MID-GAP STATES IN DEFECTIVE ANATASE TiO_2 : A DENSITY FUNCTIONAL THEORY STUDY PLUS A HUBBARD TERM (DFT+U)

BY

KANER TOLBERT NGEYWO

A THESIS SUBMITTED IN PARTIAL FULFILMENT OF THE REQUIREMENTS FOR THE DEGREE OF MASTER OF SCIENCE IN PHYSICS TO THE SCHOOL OF SCIENCE OF UNIVERSITY OF ELDORET, ELDORET KENYA

2016

DECLARATION

This thesis is my own original work and has not been presented for degree to any other University. No part of this thesis may be reproduced without prior permission of the author and/or University of Eldoret.

Kaner Tolbert Ngeywo

Signature: ..... Date: .....

SC/PGP/003/12

Declaration by Supervisors

This thesis has been submitted for examination with our approval as University of Eldoret supervisors.

Signature: ..... Date: .....

Professor George O. Amolo,

Department of Physics,

University of Eldoret, Eldoret, Kenya.

Signature: ..... Date: .....

Dr. Nicholas W. Makau,

Department of Physics,

University of Eldoret, Eldoret, Kenya.

DEDICATION

I dedicate the work of this study to my beloved wife Emmy, my children; Jael, Jared, Joan and Joleen, my parents and siblings for their unwavering support during this study.

ACKNOWLEDGEMENT

First and foremost, I thank the Almighty God for His sufficient grace and mercies which are new each morning without which the completion of this study will not have been possible. Special acknowledgment goes to my supervisors, Professor G. O. Amolo and Dr. N. W. Makau for their expertise, dedication, drive and encouragement during this study. You were my father figures and mentors. Thank you so much and may God bless you and your families abundantly. I also acknowledge Dr. Kiptiemoi K. Korir for your valuable and informative discussions which went along way in enhancing the quality of this study. God bless you too.

On a similar note, I acknowledge the following institutions: the Kenya Government through the National Commission for Science, Technology and Innovations (NACOSTI) for their financial support through Grant No; NCST/5/003/4thCALL/50, Centre for High Performance Computing (CHPC), Cape Town, Republic of South Africa, for the use of their HPC cluster facility and the University of Eldoret (UoE) for the use of their resources during this study. I also acknowledge the Abdus Salam, International Centre for Theoretical Physics (ICTP), Trieste, Italy, for organizing informative schools, workshops and conferences.

I'm also indebted to my co-researchers in the Computational Material Science Group (CMSG) at the University of Eldoret Physics lab 4; Perpetua Muchiri, Caroline Bakasa, Victor Meng'wa, Felix Dusabirane, Patrick Mwonga, Denis Magero, Peter Kirui and Michael Atambo and my friend Issac Matere 'Josky'. They were always an encouragement to me and provided very informative discussions. God bless you all. Lastly, I acknowledge madam Grace Taracha for the conducive research environment in phyics lab 4 . Furthermore, your words of wisdom made a great impact in my life. May God bless you and your family too.

ABSTRACT

Motivated by the performance of reduced Titania in various important applications including photo-catalysis, photo-voltaics and CO_2 reduction in hydrocarbon fuels, a systematic study of the structural properties and the electronic band structure characteristics of intrinsic point defects in the bulk TiO_2 beginning with well established rutile then anatase was performed. All the calculations were performed within the density functional theory using an on-site Coulomb term, U=5.3 eV, and a plane wave basis set as implemented in the Quantum ESPRESSSO computer code. A comparison with the DFT results was also done. Non-relativistic norm-conserving pseudo-potentials were used to describe the core-valence interactions with GGA-PBE being chosen for the exchange-correlation functional. The systems were modeled using 48-atoms and 96-atoms super-cells for rutile and anatase, respectively. The calculated lattice parameters for the pristine cells were compared with those of other studies and found to be in good agreement with them, differing only by -1.40% to +3.42%. A direct band gap of 2.89 eV along the Γ high symmetry direction was observed in rutile while an indirect band gap of 3.01 eV from Γ-Z high symmetry points was observed in anatase TiO_2. A direct band gap of 3.11 eV was also observed along Γ in anatase. The presence of isolated intrinsic point defects, both Schottky and Frenkel within the perfect cells led to the alteration of both bond lengths and angles. The largest of these distortions occurred in the presence of Frenkel defects with O_F and Ti_F causing changes in the equatorial Ti-O bond length of between -11.2% and 12.3%, respectively, in rutile and -8.9% and 8.0%, respectively, in anatase. This was accompanied by changes in Ti-O-Ti bond angle ranging from of 143.49^0-131.41^0 and 99.93^0-88.86^0 for O_F and Ti_F, respectively, in rutile and 152.39^0-176.05^0 and 103.81^0-93.59^0, respectively, in anatase. As a result, the electronic band structures were equally altered. The presence of O_V and O_I in rutile resulted to defect states located 0.75 eV below the CB edge and 0.64 eV above the VB edge, respectively. Ti_V led to formation of defect states located 0.62 eV above the VB edge while Ti_I led to quadruple defect states located 0.83 eV & 1.17 eV above the VB edge and others located 0.93 eV & 0.56 eV below the CB edge. The presence of O_F caused defect states located 0.203 eV below the CB edge while Ti_F caused defect states located 0.801 eV above the the VB edge. In anatase, the presence of O_V and O_I resulted to defect level states located 0.735 eV below the CB edge and 0.646 eV above the VB edge, respectively. Similarly, Ti_V and Ti_I led to the formation of defect states located 0.805 eV above the VB edge and 1.22 eV below the CB edge. On the other hand, O_F caused defect states located 0.297 eV below the CB edge while Ti_F caused defect states located 0.718 eV above the the VB edge. The origin of the observed defect states in both phases of TiO_2 are the $O-2p$ and $Ti-3d$ orbitals. The contribution of $Ti-3d$ orbitals is dominant in all the considered defects except in O_F where $O-2p$ orbitals dominates. These features were confirmed by a plot of density of states differences. The calculated defect formation energies (DFEs) for the phases of TiO_2 showed that the formation of O_I is the most favoured while O_V is the most difficult to form. Additionally, it is easier to displace an atom within a crystal than to remove it all together. Since the band-gap of materials determines the overall behavior and performance of devices made from them, this study suggests that native point defects in anatase TiO_2 do indeed contribute to desired electronic properties of this material of interest for various industrial applications.

TABLE OF CONTENTS

LIST OF FIGURES

LIST OF TABLES

LIST OF SYMBOLS AND ABBREVIATIONS

α	Coefficient of linear expansion.
arb. units	Arbitrary Units
ASESMA	African School on Electronic Structure Methods and Applications
B_0	Bulk modulus
BC	boundary conditions
BFGS	Broyden-Fletcher-Goldfarb-Shannon
BOA	Born-Oppenheimer approximation
BSE	Bathe-Salpeter Equation
BZ	Brilloune Zone
CASTEP	Cambridge Serial Total Energy Package
CB	conduction band
CBM	conduction band minimum
CHPC	Centre for High Performance Computing
CI	configuration interaction
CMSG	Computational Material Science Group
DFE	defect formation energy/enthalpy
DFT	Density Functional Theory
DOS	Density of states
DSSC	Dye sensitized solar cell
EAS	Electron absorption spectroscopy
Ecut	plane wave kinetic energy cut-off
Ecutrho	plane wave charge density cut-off
ϵ_{ex}	Exchange-correlation energy per particle of a homogeneous gas

E_{tot}	Total Energy
EELS	electron energy loss spectroscopy
EHT	Extended Huckel tight-binding
ESR	electron spin resonance
EU	European Union
Exp. Value	Experimental Values
GGA	Generalized Gradient Approximation
GW	Green Function & the Screened Coulomb Interaction
H-F	Hartree-Fock
H-K	Hohenberg-Kohn
$\hat{H}$	Hamiltonian operator
HOMO	Highest occupied molecular orbital
HRTEM	high resolution transmission electron microscopy
ICTP	International Centre for Theoretical Physics
KE	Kinetic energy
K-S	Kohn-Sham
LAPW	Linear augmented plane waves
LCAO	linear combination of atomic orbital
LC	linear combination
LDA	Local Density Approximation
LSDA	Local Spin Density Approximation
LUMO	Lowest unoccupied molecular orbital
MBPT	many body perturbation theory
MD	Molecular dynamics

MOSFET	Metal-oxide-semiconductor field- effect transistor
NACOSTI	National Commission for Science, Technology and Innovations
NC-PP	Norm-conserving pseudo-potential
NIR	near infra-red
O_F	oxygen Frenkel
O_I	oxygen interstitial
O_V	oxygen vacancy
PAW	Projector augmented waves
PBE	Perdew, Burke, Ernzerhof
PDOS	Projected density of states
PE	Potential energy
PL	photoluminiscence
PP	Pseudo-potential
PW	plane wave
PWSCF	Plane wave self-consistent field
QE	Quantum ESPRESSO
QM	Quantum mechanics
QP	Quasi particle
RPE	Resonant photo-emission
RSPT	Rayleigh-Schrodinger Perturbation Theory
SC	self-consistent
STS	scanning tunneling spectroscopy
TCO's	Transparent Conducting Oxides
TDDFT	Time Dependent Density Functional Theory

T(n)	Exact K.E functional
Ti_F	Titanium Frenkel
Ti_I	Titanium interstitial
Ti_V	Titanium vacancy
TMO	Transition metal oxide
TM	Transition metal
T_o(n)	Non-interacting K.E functional
U_{ex}	electron interaction with own exchange-correlation hole
US-PP	ultra-soft pseudo-potential
UV	Ultra-violet
VASP	Vienna Ab-$initio$ Simulation Package
VB	valence band
VBM	valence band maximum
VESTA	Visualization system for Electronic and Structural Analysis
V_{ex}	Exchange-correlation potential
XcrysDen	X-Window Crystalline Structure and Densities

CHAPTER ONE

INTRODUCTION

1.1 Overview

Titanium dioxide (TiO_2), a wide band-gap semiconductor material (Lee, $et.al$, 2012), is a versatile transition metal oxide (TMO) with ubiquitous applications both technological and industrial (Chiodo, $et.al$, 2010). Many of these applications are critically linked to its band-gap (Strunk, $et.al$ 2010), an area that has not been investigated exhaustively. The band-gap determines the electrical conductivity, light absorption or transparency of TiO_2 in the visible spectral range (Ghuman &, Singh 2013). Due to its fundamental properties including insulating, semiconducting, superconducting, ferroelectric and magnetic (Batzil, M., $et.al$, 2002), TiO_2 provides a wide area that requires study. In fact, a deep understanding of properties of TiO_2 may provide a deep insight in the study of the electronic, optical and chemical properties of other reducible metal oxides (Chiodo, $et.al$, 2010). Thus, TiO_2 has attracted considerable interest in the recent years (Diebold, 2003). Its single-crystal polymorphs, surface and nano-structures response to optical excitation are of topical interest in solar energy harvesting through photo-catalytic splitting of water into hydrogen and oxygen, photovoltaic generation of electricity (see **Figure 1.1**)as well as reduction of CO_2 in hydrocarbon fuels (Diebold, 2003, Strunk, $et.al$, 2010, Navio, $et.al$, 1996).

The discovery of water photolysis on a TiO_2 electrode by Fujishima and Honda in 1972 (Fujishima & Honda, 1972) has been recognized as a landmark event in the science of TiO_2. This discovery led to a good establishment that surface defects plays an important role in surface chemistry phenomena like mass transport and decomposition and also a strong bearing on the chemical and electronic properties of oxide surfaces (He & Sinnott, 2005, Jensen, 1999). Since then, TiO_2 has attracted immense attention as an ideal material for photo-catalysis (see **Figure 1.2**) since it possesses excellent properties including high activity, good stability, non-toxicity and low cost (Wang, $et.al$, 2012).

Currently, TiO_2 is being used in vast fields of renewable energy and ecological environmental protection. However, due to its large band-gap (rutile $\sim 3.0\ eV$ and anatase $\sim 3.2\ eV$), visible light sensitivity which is necessary for high performance under solar spectrum illumination (Di Valentin., $et.al$, 2004, Schelfe, $et.al$, 2013, Mattthisen, 2007, Morris, $et.al$, 2000, Batzill, $et.al$, 2002) is dwarfed.

Apart from renewable energy applications, TiO_2 as a semiconductor has various application in a wide range of fields. It is currently being actively used in phononics, dilute magnetic semiconductors, spintronic devices, photo-sensors, as white pigment (in paints and cosmetics) coatings, electronic devices like varistor, bone implants, gas sensors, medicine in cancer therapy (see **Figure 1.3**), photochemical reactions as well as catalysis (Diebold, 2003). As a matter of fact, TiO_2 is currently being discussed as the best possible dielectric gate material for the new generation MOSFETS to replace SnO_2 and as a spacer material in magnetic spin valve systems (Morgan, 2009, Ying, $et.al$, 2013, Na-Phattalung, $et.al$, 2006, Zhang, $et.al$, 2014). As mentioned earlier, many of these applications are tightly connected to the band-gap whose general behavior is greatly influenced by the isolated intrinsic point defects and impurities introduced in the TiO_2 structure (He & Sinnott, 2005).

Principally, perfect stoichiometric metal oxides exhibit insulation properties, but intrinsic point defects or structural changes turns these oxide materials into semiconductors or conductors depending on the defect concentration or the level of the structural distortion (Santara, $et.al$, 2013). Point defects and impurities can be found in both bulk, the surface and at the grain boundary. These defects can form energy levels which may act as trapping centres or shallow energy levels which may act as donors (Morgan & Watson, 2009, Na-Phattalung, $et.al$, 2006). Consequently, there is a great interest in trying to understand defect structures and the mechanisms responsible for their creation. Further impetus that is driving research in TiO_2 is the current need for economical, sustainable and environmentally friendly sources of energy globally which TiO_2 has shown great potential since it is economical, readily available, biologically and chemically inert, stable to corrosion and non-toxic (Diebold, 2003, Di Valentin, $et.al$, 2004).

Experimental methods are rather successful in the study of defect concentration. However, a deeper understanding of the defect formation is still limited due to the extreme sensitivity of the electronic and physical properties of metal oxides to minute defect and impurity concentration in the bulk material (Cho, $et.al$, 2006). It is therefore important to understand the nature of the defect and formation mechanism in bulk metal oxides like TiO_2 especially since they influence conductivity of the material in different ways depending on the gas adsorption and temperature fluctuations, a part of which has been answered by the work of He & Sinnott (2005). Therefore, by controlling the nature and concentration of the defects and impurities, one can be able to tailor make the conductivity and absorption spectra of a semi-conducting transition metal oxide (TMO) such as TiO_2 to suite the requirements of particular applications.

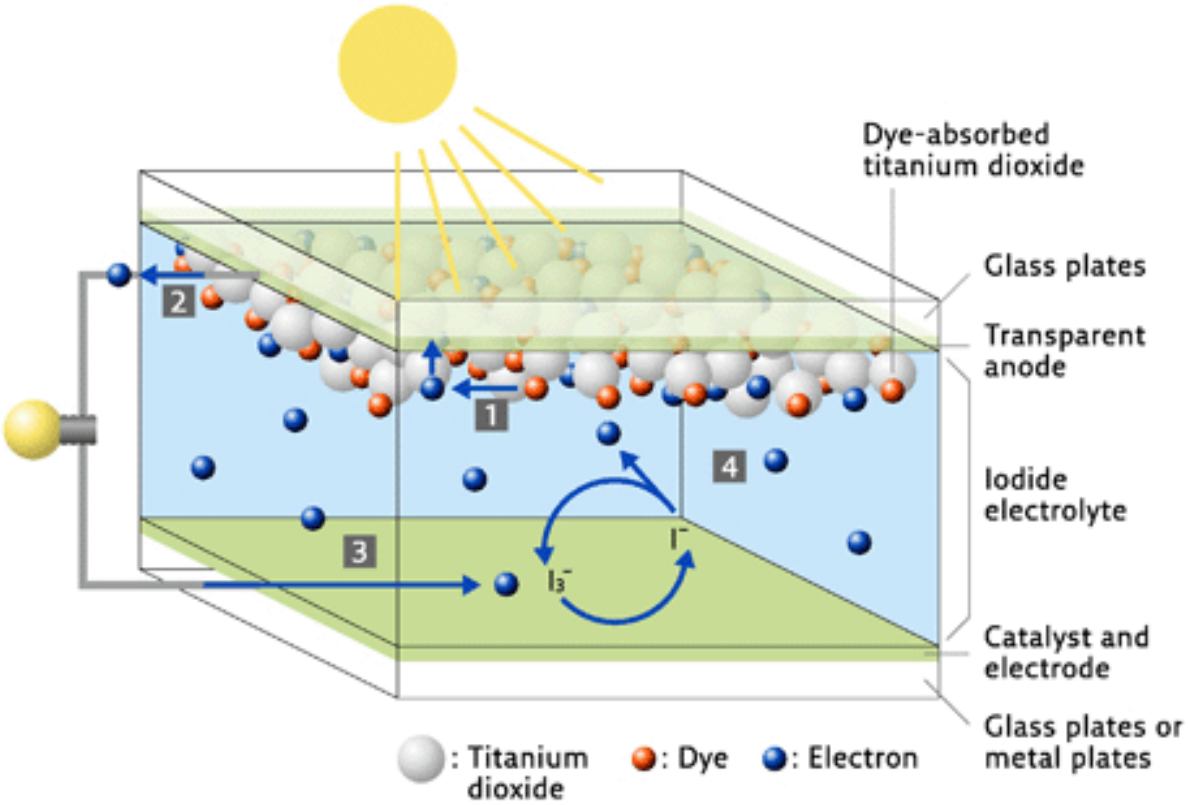

Figure 1.1: Representation of the reaction in a DSSC (Adapted from NISSHA: www.nissha.com).

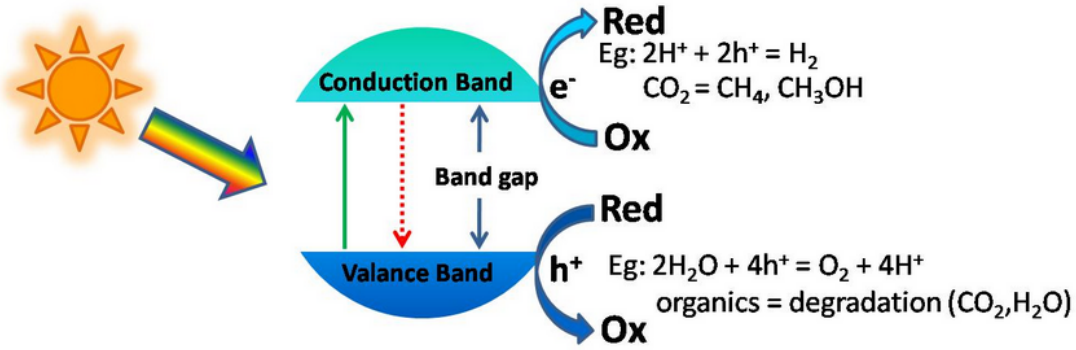

Figure 1.2: Photocatalytic reaction using clean TiO_2. Red means reduction reaction while OX means oxidation reaction (Adopted from phelafel: www.nde.edu.org).

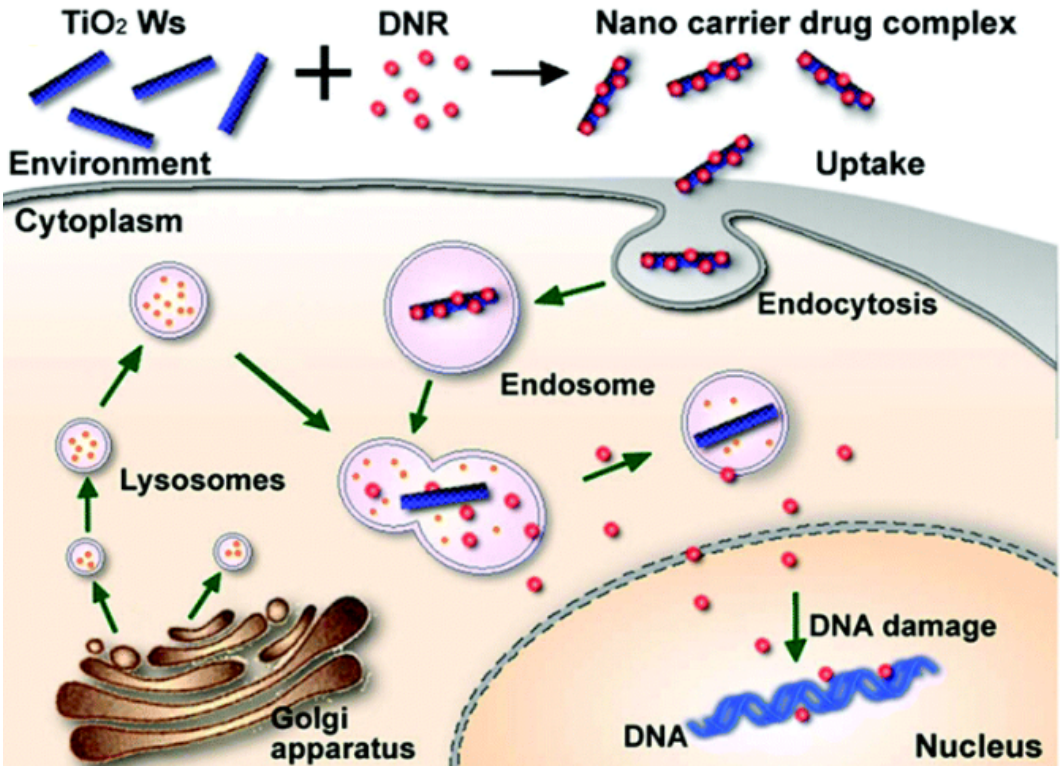

Figure 1.3: Cancer therapy using nano-sized TiO_2 (www.pubs.rsc.org).

1.2 Titanium Dioxide Phases

Titanium dioxide crystallizes in three major phases (see **Figure 1.4**); rutile (tetragonal, a=b=4.589Å, c=2.953Å), anatase (tetragonal, a=b=3.782Å, c=9.502Å) and brookite (rhombohedrical, a=5.436Å, b=9.166Å, c=5.135Å) (Diebold, 2003). There exists other six phases; TiO_2-OII (Cotunite) - orthorhombic, TiO_2-OI,- orthorhombic, TiO_2-(II) [PbO_2-like] - orthorhombic, TiO_2(R) [ramsdellite-like] - orthorhombic, TiO_2(H) [hollandite-like] - tetragonal & TiO_2(B)- monoclinic. Cotunite is synthesized at high pressure and is the hardest polycrystalline material known to exist (Diebold, 2003). Of the known phases of titanium dioxide, only rutile and anatase are currently used for various known applications, thus extensive studies, both experimental and theoretical with interesting physical and chemical properties have been harnessed on the bulk structures and literature on both bulk and surfaces is available (Strunck, $et.al$, 2010). Rutile is the most thermodynamically stable except at the nano-scale and possibly at very low temperature for which anatase is known to be stable (Muscat, $et.al$, 2002). It is reported that at temperature between 400-800^{o}C, anatase transforms to rutile (Glassford & Chelikowsky, 1992). However, depending on the method of preperation and impurities the temperature can be as high as 1200^{o}C (Sun, $et.al$).

The rutile and anatase phases of TiO_2 are structures characterized by two complimentary Ti_xO_y building-block representations with the most common network being the edge and/or corner linked distorted TiO_6 octahedron building-block (Simons & Dachille, 1967). Rutile and brookite exhibits both corner and edge-sharing TiO_6 units. In rutile TiO_2, the O_h symmetry of an ideal octahedra is reduced to D_{2h} symmetry due to the different in-plane (equatorial) and out-of-plane (axial) $Ti-O$ bond length and two types of $Ti-O-Ti$ in-plane bond angles deviating by 90^o and axial $Ti-O$ bond length being slightly longer than the equatorial one (Diebold, 2003). Anatase has additional displacement of O ions from the equatorial position generating a local D_{2h} symmetry seen by the Ti ions. Due to stronger distortion in brookite TiO_2, all bond lengths and bond angles slightly diffuse from each other, thus, leading to a formal loss

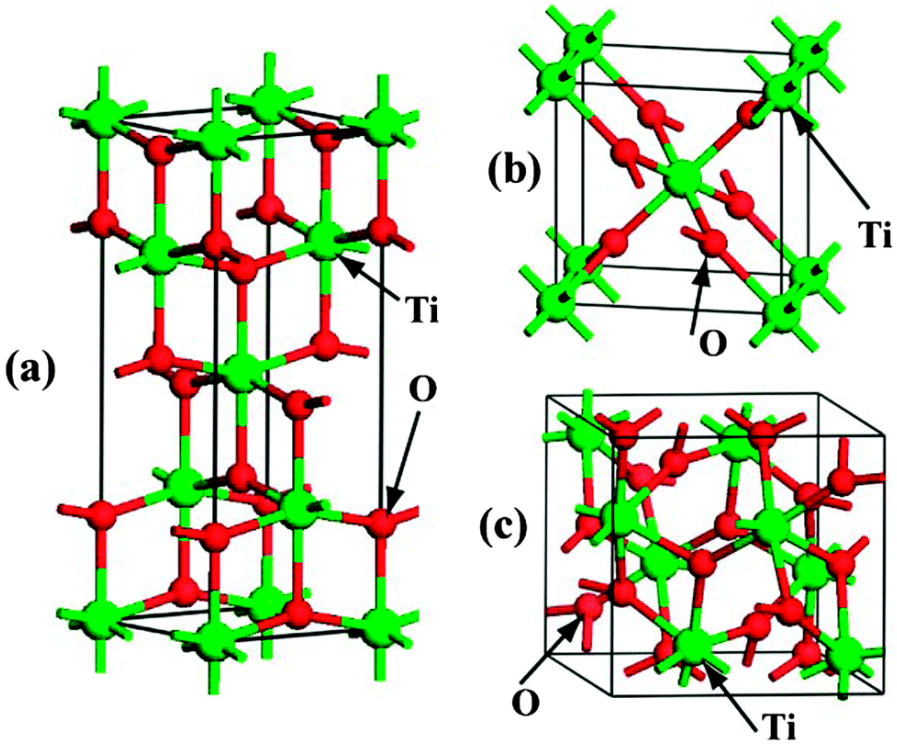

Figure 1.4: Diagramatic representation of the three main phases of TiO_2 (a) Anatase (b) rutile (c) Brookite. (Adopted from Zhang, $et.al$**,(2014): www.pubs.rsc.org).**

of local symmetry and C_1 symmetry TiO_6 units (Henderson, 1999). The key difference between rutile and anatase comes from the connection of its octahedra, where in rutile they share two edges with other octahedra while in anatase they share four edges. A summary of most known properties of rutile and anatase are shown in the **Table 1.1**.

Table 1.1: Properties of rutile and anatase (Diebold, 2003, & Henderson, 1999).

Property	*Rutile*	*Anatase*
Crystal Structure	*Tetragonal*	*Tetragonal*
Space Group	$P4_2/mnm$	$I4_1/mnm$
Lattice Constants($\AA$)	$a = 4.5936,\ c = 2.9587$	$a = 3.784,\ c = 9.515$
Atoms per unit cell	6	12
Phase Transformation	*No*	*Rutile* $(400 - 1000^oC)$
Density (g/cm^3)	4.25	3.89
Melting Point(^oC)	1855	*Turns to Rutile*
Permittivity (ε_r)	$90(c-axis),\ 170(a-axis)$	$38(c-axis),\ -$
$Ti-O$ *bond length*($\AA$)	$1.949(d_{ax}),\ 1.980(d_{eq})$	$1.965(d_{ax}),\ 1.937(d_{eq})$
Band gap (eV)	3.0	3.23
$Reflectance, \%(at\ 400^oC)$	$47-50$	$88-90$
UV light A at $360nm$ $(\%)$	90	67
$Coefficient\ of\ linear$ $expansion,\ \alpha,\ (10^{-6}/K)$	7.14	10.2

1.3 Point Defects

Structural defects in TiO_2 have been studied since the early years of 1950s (Rao, $et.al$, 2003). Intrinsic point defects includes vacancies (O_V and Ti_V), self-interstitials (O_I and Ti_I) and anti-sites (O_{Ti} and Ti_O). Ordinarily, defects exists in equilibrium between the crystal lattice and its environment and a material can either have point defects or extended defects or both. Point defects are associated with single crystals and occur at/around a single lattice site (see **Figure 1.5 and 1.6**) and have significant effects on the properties of semiconductors and insulators while extended defects occur at greater ranges. Isolated intrinsic point defects play a significant role in the determination of properties of crystalline solids. These zero dimensional defects influence all physical, chemical and structural properties. In ionic solids, electrical properties (both ionic and electronic transport) are mainly determined by the concentration of these point defects and their mobilities. Thus, any modification of these defects leads to a variation in the electrical properties. Defects influences optical properties of materials too. Therefore, a deeper understanding of point defects is very important in the science of materials.

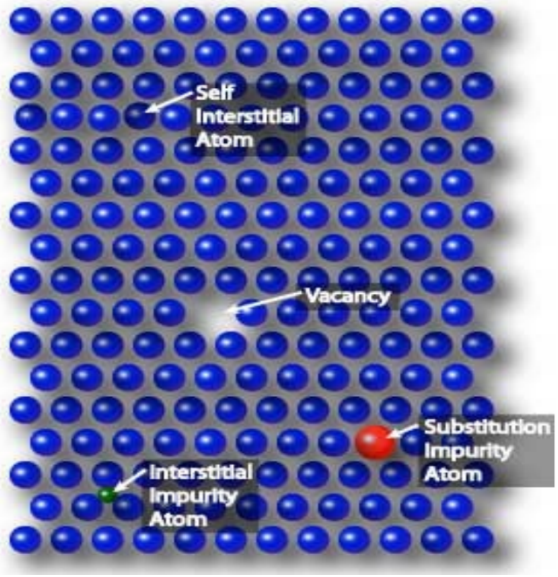

Figure 1.5: Pictorial representation of various defects in materials (Adopted from Preshat: www.nde.ed.org).

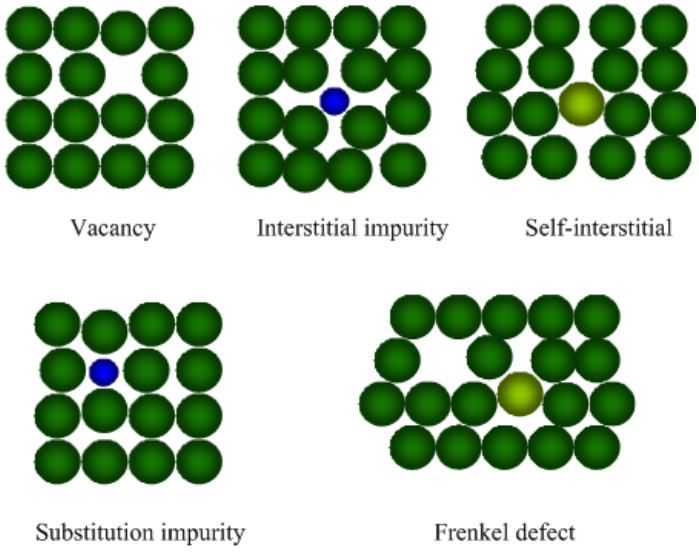

Figure 1.6: Schematic diagrams of types of defects (Adopted from Phelafel: www.phelafel.ac.il).

Point defects are either Frenkel or Schottky in nature and often occur in ionic crystals and vacancies with charge balanced in the whole crystal despite the presence of interstitials or ions and vacancies. Frenkel defects, Frenkel pair or Frenkel disorder occurs when an atom or a smaller ion (usually a cation) leaves its place in the lattice, creating a vacancy and becomes an interstitial by lodging in a nearby location. They do not have an impact on the density of the solid as it only involve the migration of the ions

within the crystal thus preserving both the volume and mass. On the other hand, Schottky defects are associated with only vacancies of cations and ions with no interstitials or misplaced ions and has an impact on the density of the solid as it involves the addition or removal of the ions within the crystal thus increasing or reducing both the volume and mass.

1.4 Ab *initio* Calculations

Attempts to determine the properties of materials from an analytical first principle solution (*ab initio*) to the Schrödinger equation for a quantum many-body interacting system pauses a daunting task to researchers (Schaefer, 2012). However, recent advances in both theoretical and computer softwares have provided some way forward (Smith & Sutcliffe, 1997). Computational results complement the information provided experimentally and also predicts unobserved chemical phenomena. But, to this level, the size of the system provided by the Schrödinger equation for the many-body system is still enormous. The exact numerical solution to this system is impractical or entirely lacking thus necessitating approximations specific to the system in evaluating the physical quantities of this interacting system. The *ab initio* (i.e without any input parameters other than the constituent particles making the material) (Schaefer, 2012) methods are entirely based on quantum mechanics (QM) and basic constants. Just like the semi-empirical methods, they involve approximations which range from simplified forms of first principle equations that are easier or faster to solve to approximations limiting the size of the system (periodic boundary conditions, BC). Born-Oppenheimer approximation (BOA) which greatly simplifies the underlying Schrödinger equation by assuming that the nuclei remains in place during the calculation is one such fundamental approximations.

Practically, however, it is impossible to eliminate approximations and the residual error inevitably remains. The *ab initio* method eventually converges to the exact solution of the underlying equation as the number of approximations are reduced. The goal of computation chemistry or physics is to minimize the residual error while at the same

time keeping the calculation tractable. The basis set (usually built from linear combination of atomic orbitals, LCAO, ansatz), used to solve the Schrödinger equation is not complete and does not span the entire Hilbert space associated with ionization and scattering process. The Hartree-Fock (H-F) and Configuration Interaction (CI) methods allow one to treat the Schrödinger equation as a "simple" eigenvalue equation of the electronic molecular Hamiltonian with a discrete set of solutions. As stated earlier, an ab-initio electronic structure method can be made to converge to the exact solution when all approximations are sufficiently small in magnitude and when the finite set of basis functions tend towards the limit of a complete set thus providing a great advantage as discussed.

The Kohn-Sham equation within the Density Functional Theory (DFT) using either the Local Density Approximation (LDA), Local Spin Density Approximations (LSDA) or Generalized Gradient Approximation (GGA) provides a way of calculating the electronic structures of a large percentage of materials in Condensed Matter Physics (Oliver & Perdew, 1979). Here, the many-body problem is solved by considering a non-interacting system with one-electron exchange correlation potential. DFT is largely applied since it is highly accurate, thus helping in interpreting experimental data. It also has a predictive power leading to calculations which are relatively cheap computationally compared to more sophisticated methods. Though largely approximate in nature, LSDA and GGA are quite accurate and thus very applicable to extended systems. The ground-state properties for majority of the systems can be provided by the exact DFT. However, for strongly correlated systems, usually containing transition metals or rare-earth metal ions with partially filled d and f shells, LDA and GGA spectacularly fails (Anisimov, $et.al$, 1997). Thus, depending on the material being considered and its properties, DFT can lead to results that are in total agreement or disagreement with the experimental ones. An example of such occurrence is where the band-gap of semiconductors and insulators are largely underestimated or not even observed at all. For better band-gap estimation, the Hybrid Functionals and DFT+U i.e (LDA+U or GGA+U or LSDA+U) are used. U is the Hubbard interaction of Coulomb energy i.e on

site repulsion term added to the transition metal d state (Anisimov, $et.al$, 1991).

1.5 Statement of the problem

Intrinsic point defects in oxide semiconductors have been studied extensively since the early 1950s bringing to the fore the relationship between defect chemistry and the semiconducting behaviour of important materials like transition metal oxides (TMOs). However, much of these studies in TiO_2 have focused on O_V and Ti_I in the rutile phase leaving an information deficiency in other phases. Similarly, there is contention on the role of vacancies in bulk rutile TiO_2. Whereas, it has been reported that O_V contribute to the formation of defect levels within the band gap, views contrary to this have also been reported, thus suggesting a need for further research to clarify on such issues. Additionally, despite studies indicating the presence and influence of these intrinsic point defects on the band gap modifications, the origin and localization of the observed defect level states thereof is still contentious.

1.6 Significance of Study

The study of TiO_2 is motivated by its wide ranging applications in the fields of renewable energy and ecological environmental protection for example photo-catalysis, light harvesting in dye sensitized solar cells (DSSCs) and nano-scale electronic devices (Chiodo, $et.al$, 2010, Wang, $et.al$, 2014) among others. Its single-crystal polymorph, nano-structures and surface responses to optical excitation is of topical interest in photo-catalysis, solar energy harvesting through photo-voltaic generation of electricity as well as reduction of CO_2 in hydrocarbon fuels (Fujishima, $et.al$, 2000). Since 2003, TiO_2 has been the "hottest" topic of discussion in material science as the best dielectric gate material to replace SiO_2 in MOSFET devices (Diebold, 2003).

However, despite this huge potential of stoichiometric TiO_2, its large band-gap ($\sim 3.00 - 3.23\ eV$) limits its response to light activity to the UV region ($\lambda = 414.4 - 384.9\ nm$) of the electromagnetic spectrum which accounts for only 5% of the spec-

trum in contrast to visible light region which is 45% (Na-Phattalung, $et.al$, 2006). An important activity like photo-catalysis requires a band-gap of $\sim$ 2.0 eV thus rendering pure TiO_2 unsuitable (Zhu, $et.al$, 2014).

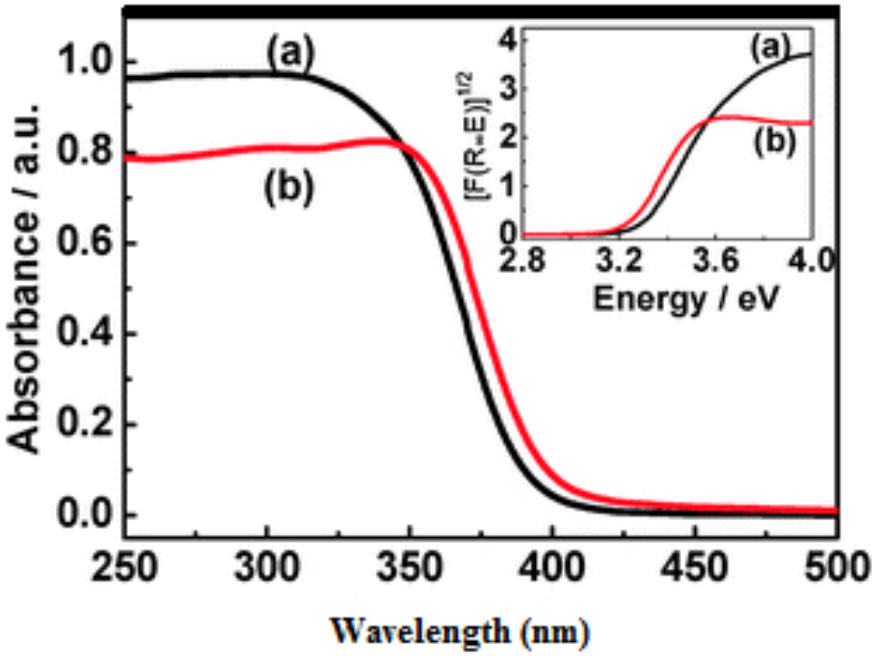

Figure 1.7: Light absorption of clean anatase surface (001): (a) Nano-sized (b) Micron-sized. (Adopted from Guia(2010): www.pubs.rsc.org).

Arising from this fact, much effort in the last decade has been devoted to extending the spectral responses of TiO_2 to visible light. Surface disorders and intrinsic point defects provide a viable way towards achieving this. Point defects in TiO_2 bring additional features in the electronic band structure, thus substantially influencing the transport and optical behaviour of TiO_2 (Campbell, $et.al$, 1999). Since different applications require specific band gap, understanding how the band gap is modified is important in tailor making TiO_2 to suit these applications. This study which focuses on understanding the mid-gap states and their precise positions within the band gap in anatase will provide enriching information on how improvement on important processes including photocatalysis (which requires a band gap $\approx$ 2 eV), solar energy harvesting and CO_2 reduction in hydrocarbon fuels due to improved optical excitation may be achieved. The study has used GGA+U to investigate Schottky and Frenkel defects in anatase phase of

TiO_2 with emphasis on the influence of the presence of these defects on its electronic properties. Since rutile phase has been the paradigm in the study of metal oxides and especially TiO_2, this work begins with a study of rutile at each level.

1.7 Objectives

The goal of this study is to investigate the effect of the intrinsic point defects on the pristine rutile and anatase phases of titanium dioxide which will be achieved through the following specific objectives;

1. To determine the structural changes including bond lengths, angles and bulk modulus occurring in rutile and anatase TiO_2 upon introduction of O_I, O_V,Ti_I, Ti_V, O_F and Ti_F defects.

2. To identify the defect states and its origin in the band gap upon the introduction of O_I, O_V,Ti_I, Ti_V, O_F and Ti_F defects in the two phases of TiO_2.

3. To calculate the formation energies of the different intrinsic point defects mentioned in objective one above on the two phases of TiO_2.

CHAPTER TWO

LITERATURE REVIEW

2.1 Introduction

Titanium dioxide is an important transition metal oxide (TMO) that has been studied extensively both experimentally and theoretically (Di Valentin, $et.al$, 2004). Various semi-empirical and first principle methods have predicted important properties that agree well with experimental findings. Important properties of TiO_2 including its light absorption, charge transport and surface adsorption are closely related to its defect disorder, which in turn plays a significant role in the photo-catalytic performance of TiO_2 (Diebold, 2003). This chapter reviews some of the important available information on materials modelling and point defects in TiO_2.

2.2 Materials Modelling

Computational materials design integrates targeted materials process–structure and structure–property models in systems framework to meet desired engineering needs. Important aspects of materials such as transmittance, thermo-chromic, mechanical and electrical properties play important roles in the functionality of these materials but their manufacturing cost greatly influences the consumer costs (Smith & Sutcliffe, 1997). Thus, design essentially consists of many competing requirements that require judicious decisions regarding key trade-offs (Schaefer, 2012). The goal of computational materials design is to apply the best scientific understanding to facilitate decisions regarding the optimal trade-offs that meet desired needs in the time and resource efficient manner (Wahle, $et.al$, 2001).

Computer simulations have been used in the investigation of various materials having a wide range of properties with promising findings which compare well with the experimental ones (Strunk, $et.at$, 2010, Glassford, & Chelikowsky, 1992). Most theoretical calculations use either empirical and semi-empirical methods such as tight bind-

ing and Mott-Littleton methods, molecular dynamics (MD) simulations, and more theoretically rigorous first principles approaches or the third class methods which include Hartree-Fock (HF) and density functional theory (DFT) methods.

When modelling a material for energy application such as TiO_2, it is more than likely that knowledge with good accuracy of one or more of the following properties: electronic band gap, gap level alignment and optical gap comes in handy. Great findings on the structural, electronic, optical and magnetic properties both theoretical and experimental for TiO_2 have been well reported and documented. However, much of the available data is on rutile phase since most crystal-growth techniques yields rutile. Additionally, rutile has the simplest best known structure and which is the most stable form of TiO_2 (Diebold, 2003). The direct band gap of 3.0 eV reported for rutile is also desirable for the semiconductor applications (Chiodo, $et.al$, 2010, Diebold, 2003, Strunk, $et.al$, 2010, Di Valentin, $et.al$, 2004, Matthisen, 2007, Morris, $et.al$, 2000).

2.3 Point Defects in Titanium Dioxide

Huge resources and time have been devoted to the study of non-stoichiometric rutile TiO_{2-y} both in the structural aspect related to the nature of defect (Zekrzewska, 2011) and in the subsequent physical and thermal properties. Generally, it is believed that titania can support large deviations from stoichiometry (Trnzek-Zajac, $et.al$, 2012). However, there is still disagreement as to the extent of non-stoichiometry and the mechanism it is accommodated in rutile. A study by Wahlbeck and Gilles reported that TiO_2 occurs in a wide range of non-stoichiometric structures which are determined by temperature and oxygen pressure (He, & Sinnott, 2005, Waldner, & Erikson, 1999, Cancarevic, $et.at$, 2007). Order-disorder transformations take place over the entire composition range of Ti-O solid solution depending on the temperature (Umebayashi, $et.al$, 2002). Just like most non-stoichiometric oxides, the thermo-chemical and electronic properties of rutile and anatase TiO_2 are directly influenced by the type and concentration of point defects or impurities (Cancarevic, $et.at$, 2007, Umebayashi, $et.al$, 2002).

Due to the unique electronic configuration and spectral characterization of transi-

tion metals (TMs), TM doping is one of the most effective approaches of extending the absorption edge of TiO_2 to the desired range (visible light region) (Di Valentin, 2004). Depending on its concentration, dopants can provide free carriers to increase conductivity and enable applications in electronics (Batzil, $et.al$, 2002). Alternatively, the dopants and impurities result in defect levels and break the crystal symmetry, thus, inserting of new states into the original band-gap or modification of the CB or VB, thereby improving photo-catalytic activity of TiO_2 and light harvesting to a desirable degree (Schleife, 2013). The defect level states in the band-gap allow sub-band-gap illumination by improving electron transitions from the VB to the CB thus improving visible-light activity (Matthiesen, 2007). In TiO_2, *O-2p* orbitals dominate the VB and *Ti-3d* states of the five-fold coordinated Ti atoms govern the CB due to the electrostatic downward shift of the 3-*d* states. Thus, introducing dopants with different p-orbital energies relative to the $O - atoms$ shifts the valence band maximum (VBM) upwards while dopants with different d-orbital energies vis-a-vis Ti atoms shifts the conduct band minimum (CBM) downwards (Morris, $et.al$, 2000, Peng, $et.al$, 2012).

Umebayashi, $et.al$ (2002), showed that localized Co doping was sufficiently low to lie at the top of the VB while other dopants like V, Mn, Fe, Ni and Cr produced mid-gap states. Yu & Halley (1995), using semi-empirical methods further confirmed the red shift of the absorption edges and narrowing of the band gap of Fe:TiO_2 nano-rods. Xing-Gang, $et.al$ (2009), showed that new occupied bands were found in the band gap of Ag doped anatase TiO_2. Zhu, $et.al$ (2013), showed that Cu could lead to enhancement of d-states near the uppermost part of the VB of TiO_2 and both Ag and Au doping caused some new electronic states in the band gap. As stated in section 1.6, the advantages of doping is an issue of little debate. However, doped materials suffer from thermal instability. Dopants also introduce carrier recombination centres leading to quantum inefficiencies in the TiO_2 devices (Hossain, $et.al$, 2006). Similarly, the solubility limits of the dopants especially for tuning electrical properties of relatively closely packed solids such as TiO_2 can not be underestimated (Adepalli, $et.al$, 2013).

Defects, just like dopant impurities have profound effects on the properties of ti-

tanium dioxide. Among all the defects identified, oxygen vacancy is one of the most important and is the most prevalent defect in many metal oxides, which has been widely investigated both by theoretical calculations and experimental characterizations. It is well-known that TiO_2 can loose oxygen resulting in the formation of both bulk and surface vacancies which changes both the chemical and electronic properties of TiO_2 and consequently its device performance (Navio, $et.al$, 1996). Oxygen vacancies in bulk TiO_2 can be detected using electron paramagnetic resonance (EPR) spectroscopy because the electrons remaining in a vacancy move towards the neighbouring Ti atoms forming two reduced Ti^{3+} cations (Chiodo, $et.al$, 2010). Basing on scanning tunnelling microscopy (STM) studies and theoretical calculations by Diebold, $et.al$ (1996), local electronic properties induced by intrinsic and extrinsic defects on these surfaces are established. Studies using ultraviolet photo-emission spectroscopy (UPS) and electron energy loss spectroscopy (EELS) suggests that oxygen deficiency defects give rise to localized gap states lying about 0.7-1.0 eV below the CB edge (Yang, $et.al$, 2009, Henrich, $et.al$, 1976).

However, the origin and localization of these states is still contentious, even though electron spin resonance (ESR) study has shown that unpaired electrons associated with oxygen vacancy are localized on two of the three Ti sites adjacent to the vacancy (Yang, $et.al$, 2009). Scanning tunnelling spectroscopy (STS) also reports that oxygen vacancies and impurity atoms with positive charge state give rise to mid-gap states within the band gap (He, & Sinnott, 2005). In both cases, they cause n-type conductivity and localized downward band bending. As noted by Lany and Zunger (2009), defect localization arise from both the electronic state and the interaction of electronic states with lattice distortions – a polaronic effect. Janotti, $et.al$ (2010), using HSE06 functional to study oxygen vacancy and substitutional dopants reported that the vacancies have localized states in the gap but that the transition levels was shallow.

From the calculations on the role of bulk vacancies in rutile TiO_2 by a scattering theoretical method using the classical Green's function, it has been reported that bulk oxygen vacancies do not induce any defect states inside the gap of TiO_2 (Munnix, &

Schmeits, M., 1984). In contrast, Ramamoorthy (1994) found that oxygen vacancies and titanium interstitial introduces defects within the band gap. Using semi-empirical methods, Yu and Halley (1995) working on oxygen vacancies and titanium interstitial in reduced rutile reported donor levels in the range of 0.7-0.8 eV for isolated defects and also the presence of clustering in nearly stoichiometric rutile with multiple defects (Yu, & Halley, 1995). Dawson $et.al$ (1996) using DFT studied point defects and impurities in bulk rutile TiO_2 reported that isolated Schottky and Frenkel defects are equivalent energetically. Cho $et.al$ (1996) using DFT calculation of neutral oxygen vacancies and titanium interstitial in rutile reported the defect formation energies (DFEs) as 4.44 eV and 7.09 eV, respectively, thus indicating that oxygen vacancy formation is favoured. They also reported that mid-gap states above the VBM instead of Ti^{3+} ions associated with oxygen vacancy are responsible for the visible and infra-red absorption in disordered engineered black TiO_2 (Cho, $et.al$, 2006). However, in that study by Cho $et.al$ (2006), temperature and oxygen partial pressure were not considered. Extensive series of Mott-Littleton calculation study by Catlow $et.al$ reported that Schottky defects are energetically more stable than the Frenkel defects and also that vacancies are predominant in rutile phase of TiO_2 (Catlow, $et.al$, 1982, 1985).

For many years, catalytic activity has been discussed in terms of surface oxygen vacancies, based on resonant photo-emission (RPE) or EELS. In fact, a study by Schaub $et.al$ (2001) using DFT combined with STM experiments showed that the dissociation of water is energetically possible on rutile TiO_2 (110) surface only at oxygen vacancies sites. However, not many years before Wendt, $et.al$ (1989), interpreted STM maps in terms of a dominant role of Ti interstitials and reported that Ti interstitial in the near surface region play a crucial role for the band gap states. Experiments by Henderson (1999) demonstrated that major diffusion species in the bulk-assisted re-oxidation of ion-sputtered TiO_2 are Ti interstitials rather than O vacancies ([Henderson, 1999). The transition from oxygen vacancies to titanium interstitial in anatase has been reported by Weibel $et.al$ (2006) on the basis of the measurement of the electrical resistance in dense anatase ceramics. This transition has been observed upon temperature increase and/or

the oxygen partial pressure decrease leading to a conclusion that titanium interstitial is more favourably formed in anatase than rutile due to the lower density than rutile.

Santara $et.al$ (2013) from low temperature in situ photo-luminescence (PL) studies reported that there is great evidence for Ti surface interstitials being responsible for the near infra-red (NIR) PL emission at 1.27 eV ($\lambda = 969.29\ nm$) and 1.47 eV ($\lambda = 845.66\ nm$). In the same study, they also reported that UV-visible-NIR absorption spectroscopy showed states within the band-gap of TiO_2 nano-ribbon. During TiO_2 growth, mass transport also suggested that Ti interstitials were involved (Zhu, $et.al$, 2009). As a matter of fact, this debate has continued, and recently, resonant photoemission (RPE) spectra again suggested that localized gap states were due to the oxygen vacancy (Mitsuhara, $et.al$, 2012, Yim, $et.al$, 2010). Interestingly, it is reported that both O vacancy and Ti interstitial can coexists in reduced TiO_2 though in different concentration depending on the chemical synthesis and post growth thermal treatments under different environments (Santara, $et.al$, 2013). Thus, providing a detailed description and understanding the specific role of each native defect in reduced titania is very important.

Experimental techniques such as space charge segregation measurements, thermogravimetric measurement and tracer impurity diffusion report that Frenkel defect formation energies are lower than Schottky defect formation energies, thus more energetically favourable in TiO_2 than Schottky defects (Wahlbeck, & Gilles, 1966, Kofstad, 1962). This finding is supported by the work of He & Sinnott (2005) using DFT. In the same study, the calculations also indicated that both Frenkel and Schottky defects prefer to cluster together rather than spread out across the unit cell (He, & Sinnott, 2005). However, several other theoretical calculations find that DFEs for Frenkel are much higher than those of Schottky (Catlow, $et.al$, 1985, Tomlinson, $et.al$, 1989, Shao, 2008). Extended Huckel tight-binding (EHT) and pseudo-potential Hatree Fock (PP-HF) calculations have been done on anatase with PP-HF predicting larger band-gap value while the former giving a good estimation of the bond length (Dupin, $et.al$, 2000). Most of the available literature suggest that fewer theoretical investigations have been done so far

on effects of intrinsic point defects in anatase compared to rutile.

CHAPTER THREE

COMPUTATIONAL THEORIES

3.1 Introduction

Electronic band structure calculations both for ground-state and excited state are an important aspect in Condensed Matter Physics. Electrons and nuclei of materials determine most properties of condensed matter and molecules. They provide salient information about structural, magnetic, electronic and optical properties. However, computational methods that can accurately treat the interacting system of a huge number of electrons and the nuclei are a big problem even with modern age computer technology. The interacting system with many electrons and nuclei is well described by the Schrödinger equation, but inspite of this providing the exact solution to the Schrödinger equation to the many-body problem for a system of N interacting electrons in the internal Coulomb field created by a collection of atomic nuclei is a very difficult task. A number of structure methods have been developed in the past to try and overcome this hurdle with a great degree of success. In this chapter, the most prominent ones will be discussed following the scheme by Harrison (2003).

3.2 Many Body Problem

Neglecting relativistic effect, all matter is described at a fundamental level by quantum theory whose central feature is the many-body wave function. For a system of N_e electrons and N_n nucleons, the non-relativistic time-independent Schrödinger equation for the full description of the quantum behaviour of an atom is given by:

$$\hat{H}\Psi = E\Psi, \tag{3.1}$$

where $\hat{H}$ is the Hamiltonian, Ψ is the many-particle wave-function and E is the total energy of the system. The many-particle wave function can either be symmetric or anti-symmetric. The symmetric case is expressed as;

$$\Psi^{(S)}_{n_{1...}n_N}(...r_i....r_j) = \Psi^{(S)}_{n_{1...}n_N}(...r_j....r_i), \tag{3.2}$$

while the anti-symmetric case is given by;

$$\Psi^{(A)}_{n_{1...}n_N}(...r_i....r_j) = -\Psi^{(A)}_{n_{1...}n_N}(...r_j....r_i). \tag{3.3}$$

Particles whose wave functions are symmetric under particle interchange and have integral or zero intrinsic spin, are called bosons. Those particles with half integer spins such as electrons are described by the anti symmetric wave functions and they obey the Pauli Exclusion Principle. Such particles are called fermions. The general Hamiltonian for the many body system is thus given by equation 3.4, as,

$$\hat{H} = \sum_i -\frac{\hbar^2}{2M_i}\nabla_i^2 + \frac{1}{2}\sum_{i,j}\frac{Z_i Z_j e^2}{|\mathbf{R}_i - \mathbf{R}_j|} - \sum_k \frac{\hbar^2}{2m_e}\nabla_{rk}^2 + \frac{1}{2}\sum_{k,l}\frac{e^2}{|\mathbf{r}_k - \mathbf{r}_l|} - \sum_{k,l}\frac{Ze^2}{|\mathbf{r}_k - \mathbf{R}_l|}, \tag{3.4}$$

where, M_i is the mass of the nucleus at position R_i, m_e is the mass of an electron located at position r_i , Z is the atomic number of atoms forming the solid. The first and third terms are the kinetic energies of the nuclei and electrons, respectively, while the second and fourth terms describe the nucleus-nucleus and electron-electron Coulomb repulsion, respectively. The fifth term describes the Coulomb attraction between the nuclei and electrons.

3.3 Born-Oppenheimer Approximation

Determining the properties of materials using *ab initio* method requires that a solution to equation 3.4 is found. However, this equation is extremely difficult to solve numerically due to its huge dimensions, thus, necessitating approximations. The first and most important approximation is the Born-Oppenheimer approximation (BOA) which decouples the dynamics of the nuclei and electrons. Named after Max Born and J. Robert Oppenheimer, BOA allows the electrons and nuclear degrees of freedom to be

separated giving room for the wave-function to be broken into its electron and nucleus components. The nucleus and electrons are attracted to each other with the same magnitude of electric charge, and hence they exert the same force and momentum. While exerting the same momentum, the nucleus with a much larger mass in comparison to the electrons will have a very small velocity and considered almost negligible. Thus, the motion of the nucleus is ignored in the solving of the Schrödinger equation. The electrons are much less massive than the nuclei and therefore the electrons will respond almost instantaneously to the movement of the nuclei. Thus, the energy for a given nuclear configuration will be that of the ground state of the electrons in that configuration.

In principle, equation 3.4 may be mathematically solved to arbitrary accuracy by representing it as a direct product wave-function and diagonalizing the Hamiltonian. However, the cost of this calculation scales exponentially with the number of electrons in the system and is intractable for all but the smallest of systems.

3.4 Wave Function Based Method

A Hamiltonian operator $\hat{H}$ in QM is the quantum mechanical operator corresponding to the total energy (sum of KE and PE) of the system whose particular eigen-function operator is the wave-function which is a function that describes the quantity of states of an isolated system of one or more particles. The eigen-function operator depends on the coordinates upon which the operator acts.

3.4.1 Hartree Approximation

Hartree Approximation method is a useful method since it is an introduction to the solution of the many-body systems and the concept of self-consistency and self-consistent fields. Here the electronic Hamiltonian (equation 3.4) has its kinetic energy (KE) and nucleus-electrons interaction terms as sum of single particle operators each of which act as a single electron coordinate while the electron-electron interaction term on the other hand is a pair interaction of electrons. The initial ansatz is that the many-body wave-function may be written as,

$$\psi(r_1, r_2, ..., r_n) = \psi_1(r_1)\psi_2(r_2).....\psi_n(r_n), \tag{3.5}$$

from which it follows that the electrons are independent and interact only via the mean-field Coulomb potential. This yields one-electron Schrödinger equations of the form,

$$\frac{\hbar^2}{2m}\nabla^2\psi_1(r) + V(r)\psi_1(r) = \epsilon_1\psi_1(r), \tag{3.6}$$

where V(r) is the potential in which the electrons move. This includes both the nuclear-electron interaction,

$$V_{nucleus}(r) = -Ze^2\sum_R \frac{1}{|\mathbf{r} - \mathbf{R}|}, \tag{3.7}$$

and the mean field arising from the N-1 other electrons. Other electrons are smeared out into a smooth negative charge density ρ(r') leading to a potential of the form,

$$V_{nucleus}(r) = -e\int dx^{'}\rho(r^{'})\frac{1}{|\mathbf{r} - \mathbf{r}^{'}|}, \tag{3.8}$$

where, $\rho(r) = \sum_i |\psi(r)|^2$.

Although these Hartree equations are numerically tractable via the self-consistent field method, the approximation fails to capture elements of the essential physics, that is; the Pauli exclusion principle which demands that the many-body wave-function be anti-symmetric with respect to interchange of any two electron coordinates. This exchange condition can be satisfied by forming a Slater determinant of single-particle orbitals.

3.4.2 Hartree-Fock Approximation

As discussed in 3.4.1, although Hartree equations are numerically tractable via the self-consistent field method, the approximation fails to capture the essential element of the Pauli exclusion principle which demands that the many-body wave-function be anti-symmetric with respect to interchange of any two electron coordinates which can be satisfied by forming a Slater determinant of single-particle orbitals. This can be achieved

by Hartree-Fock approximation. Hartree-Fock theory is one of the simplest approximate theories for solving the many-body Hamiltonian. It is based on a simple approximation to the true many-body wave-function: that the wave-function ψ, is given by a single Slater determinant of N spin-orbitals,

$$\Psi(X_1, X_2...X_N) = \frac{1}{\sqrt{N!}} \begin{vmatrix} \psi_1(\vec{X_1}) & \psi_1(\vec{X_2}) & \dots & \psi_1(\vec{X_N}) \\ \psi_2(\vec{X_1}) & \psi_2(\vec{X_2}) & \dots & \psi_2(\vec{X_N}) \\ \vdots & \vdots & \vdots & \vdots \\ \psi_N(\vec{X_1}) & \psi_N(\vec{X_2}) & \dots & \psi_N(\vec{X_N}) \end{vmatrix} = |X_1 X_2 ... X_N|, \quad (3.9)$$

where, the variables X includes the coordinates of space and spin. This simple ansatz for the wave-function ψ captures much of the physics required for accurate solutions of the Hamiltonian. Most importantly, the wave-function is anti-symmetric with respect to an interchange of any two electron positions. This property is required by the Pauli exclusion principle (refer to equations 3.2 and 3.3). This wave-function may be inserted into the Hamiltonian, equation 3.4 and an expression for the total energy derived. By applying the theorem that the value of a determinant is unchanged by any non-singular linear transformation, ψ may be chosen to be an orthonormal set. Introducing a Lagrange multiplier $\epsilon_{\,i}$, the condition that the ψ are normalized and minimized with respect to the Ψ can be imposed.

$$\frac{\delta}{\delta\psi}[\langle\hat{H}\rangle - \sum_j \epsilon_j \int |\psi_j|^2 dr] = 0. \quad (3.10)$$

Here, an enormous simplification of the expressions for the orbitals Ψ results. They reduce to a set of one-electron equations of the form,

$$-\frac{1}{2}\nabla^2\psi_i(\vec{r}) + V_{ion}(\vec{r})\psi(\vec{r}) + U(\vec{r})\psi_i(\vec{r}) = \epsilon_i\psi_i(\vec{r}), \quad (3.11)$$

where, U($\vec{r}$) is a non-local potential and the local ionic potential is given by V_{ion} . The one-electron equations resemble single-particle Schrödinger equations. The full

Hartree-Fock equations are given by:

$$\epsilon_i\psi_i(r) = [-\frac{1}{2}\nabla^2 + V_{ion}(r)]\psi_i(r) + \sum_j \int dr' \frac{|\psi_j(r')^2|}{|r-r'|}\psi_i(r) - \sum_j \delta\sigma_i\sigma_j \int dr' \frac{\psi_j(r')\psi_i(r')}{|r-r'|}\psi_j(r). \tag{3.12}$$

The right hand side of the equation consists of four terms. The first and second give rise to the kinetic energy contribution and the electron-ion potential. The third term, or Hartree term, is the simplified electrostatic potential arising from the charge distribution of N electrons. As written, the term includes an non-physical self-interaction of electrons when $j = i$. This term is cancelled out in the fourth, or exchange term. The exchange term results from the inclusion of the Pauli principle and the assumed determinantal form of the wave-function. The effect of exchange is for electrons of like-spin to avoid each other. Each electron of a given spin is consequently surrounded by an "exchange hole", a small volume around the electron which like-spin electron avoid.

The Hartree-Fock approximation corresponds to the conventional single-electron picture of electronic structure. The distribution of the N electrons is given simply by the sum of one-electron distributions $|\psi|^2$. This allows concepts such as labelling of electrons by angular momenta. Hartree-Fock theory by assuming a single-determinant form for the wave-function, neglects correlation between electrons. The electrons are subject to an average non-local potential arising from the other electrons which can lead to a poor description of the electronic structure. Although qualitatively correct in many materials and compounds, Hartree-Fock theory is insufficiently accurate to make accurate quantitative predictions. Beyond Hartree-Fock formalism, Hartree-Fock is improved by taking into account the electron correlation.

3.5 Density Functional Theory (DFT)

In view of the poor predictions of chemical bonds and molecular properties afforded by Hartree-Fock approximation and the high numerical price of wave function approaches, it is beneficial to seek out methods that circumvent the need to represent the many-

body electronic wave-function. Density Functional Theory (DFT) is one of the most popular and versatile method available in Condensed Matter and Computational Physics and Chemistry. Principally for ground-state electronic structure investigation of many-body system, the properties of many-body systems are determined using functionals i.e functions of another function which in this case is the spatially dependent electron density.

With a great refinement of the approximations used to better model exchange and correlation in 1990s, DFT which was considered inaccurate in the 1970s has evolved to be rather an accurate tool. As a matter of fact, solid-state system calculations agree satisfactorily with experimental data especially on the description of the structural and electronic properties of a vast class of materials. Computationally, DFT is cheaper compared to traditional methods like HF and its descendants based on the complex many-electron wave-functions. With all these reasons, DFT is a common tool for describing and predicting the properties of the molecular and condensed matter systems. At this point, however, it is worthwhile noting that despite recent improvements, there are still difficulties in using density functional theory to properly describe intermolecular interactions especially dispersion, charge transfer excitations, transition states, global potential energy surfaces, dopant interactions and some other strongly correlated systems. There is also a limitation in calculation of the band gap (underestimation of the band gap) and ferro-magnetism in semiconductors.

3.5.1 Hohenberg-Kohn Theory

Density Functional theory, DFT, is made possible by the existence of ingeniously simple theorem put forward by Hohenberg and Kohn (H-K) in 1964 (Bauer, 1983). Hohenberg and Kohn using the first theorem proved that for a system of N interacting particles in an external potential $V_{ext}(\vec{r})$, the density is uniquely determined i.e the external potential is a unique functional of the density. Using variational principle where no wave-function can give an energy that is less than the energy of $V_{ext}(\vec{r})$ for $\hat{H}_{ext}(\vec{r})$ and by assuming

that the ground state is non degenerate, then;

$$n(r) = N \int |\psi(r_1, r_2, ..., r_N|^2 dr_1 dr_2 .....dr_N, \tag{3.13}$$

where, ψ is the ground state wave-function. Consequently, using the second theorem, the ground-state energy E is uniquely determined by;

$$E[n(r)] = F[n(r)] + \int n(r) V_{ext}(r) dr, \tag{3.14}$$

where, $F[n(r)]$ is the Universal Functional of the charge density $n(r)$. This defines an energy functional for the system and proves that the correct ground state electron density minimizes this energy functional.

3.5.2 Kohn Sham Equations

The Kohn–Sham (K-S) equation is the Schrödinger equation of a fictitious system (the "Kohn–Sham system") of non-interacting particles that generate the same density as any given system of interacting particles. The Kohn–Sham equation is defined by a local effective (fictitious) external potential in which the non-interacting particles move, typically denoted as $V_s(\vec{r})$ or $V_{eff}(\vec{r})$, called the Kohn–Sham potential. Within the framework of K-S DFT, the intractable many-body problem of interacting electrons in a static external potential is reduced to a tractable problem of non-interacting electrons moving in an effective potential. The effective potential includes the external potential and the effects of the Coulomb interaction between the electrons, i.e the exchange and correlations interactions. The K-S wave-function is a single Slatter determinant constructed from a set of orbitals that are the lowest energy solutions to,

$$[-\frac{\hbar^2}{2m}\nabla^2 + V_{eff}(\vec{r})]\psi_i(\vec{r}) = E_i \psi_i(\vec{r}), \tag{3.15}$$

where, E_i is the orbital energy of the corresponding Kohn–Sham orbital, ψ_i . The

effective potential used above has the form,

$$V_{eff}(r) = e^2 \int \frac{n(r)}{|r - r'|} d^3r + \frac{\delta E_{ex}[N]}{\delta \rho(r)} n(r) + V_{ext}(r). \tag{3.16}$$

The density for an N-particle system is given by,

$$\rho(r) = \sum_{i}^{N} |\psi_i(r)|^2. \tag{3.17}$$

The total energy of a system is expressed as a functional of the charge density as;

$$E[\rho] = T_s[\rho] + \int dr V_{ext}(r) + V_H[\rho] + V_{ex}[\rho], \tag{3.18}$$

where, T_s is kinetic energy, V_{ext} the external potential acting on the system, V_H is the Hartree or Coulomb energy and V_{ex} is the exchange-correlation energy of the system. In equation 3.18, it is only the energy expression, E and V_{ex} term that are the unknowns in the K-S approach to density functional theory. The exchange-correlation energy is given by;

$$V_{ex}(r) = \frac{\delta E_{ex}[\rho]}{\delta \rho(r)}, \tag{3.19}$$

and includes all 7 corrections in these quantities due to electron correlations.

3.5.3 Exchange-Correlation Energy

Exchange and correlation energy is the difference between the exact total energy of a system and the classical Hartree energy. How the exchange and correlation comes to the exact value determines the quality of DFT. However, it is worthy to treat the above definition with caution since the kinetic energy used is non-interacting.

$$E_{ex}(n) = T(n) - T_o(n) + U_{ex}, \tag{3.20}$$

where, $T(n)$ is the exact KE functional, $T_o(n)$ is the non-interacting KE functional and U_{ex} is the interaction of the electrons with their own exchange-correlation hole.

Thus, using the classical electrostatic interaction between the electron density $n(r)$ and the hole density $E_{ex}(r, r^{'})$, then,

$$E_{ex}[n(r)] = \frac{1}{2} \iint dr dr^{'} \frac{[n(r) n_{ex}(r, r^{'})]}{|r - r^{'}|}. \tag{3.21}$$

However, the exact form of E_{ex} is not known thus, approximation functionals based upon electron density are introduced to describe the term. The two commonly known approximations are the Local Density Approximation (LDA) functional and the Generalized Gradient Approximation (GGA) functional.

3.5.4 Local Density Approximation (LDA)

Centered on the idea of the uniform electron gas, LDA forms the basis of all approximate exchange-correlation functionals. It makes an assumption that the exchange-correlation energy at a point r is simply equal to the exchange-correlation energy of a uniform gas that has the same density at a point r. Generally, spin-unpolarized system LDA for the exchange-correlation energy is,

$$E_{ex}^{LDA}[n] = \int n(\vec{r}) \epsilon_{ex}(n) dr, \tag{3.22}$$

where, $[n]$ is the electronic density and ϵ_{ex} is the exchange-correlation energy per particle of the homogeneous electron gas of charge density $[n]$. The exchange-correlation energy is decomposed into exchange and correlation terms linearly,

$$E_{ex} = E_e + E_x, \tag{3.23}$$

hence, E_e and E_x are sought separately where the exchange term takes a simple analytic form for homogeneous electron gas (HEG). The exchange-correlation potential is obtained by,

$$V_{xc}^{LDA} = \frac{\delta E_{ex}^{LDA}[n(\vec{r})]}{[\delta n(\vec{r})]}. \tag{3.24}$$

Despite its simplicity, LDA works reasonably well in systems where the charge density is slowly varying. However it tends to under predict atomic ground state energies and ionization energies, while over predicting binding energies. It is also known to overly favour high spin state structure. LDA is also known to predict the wrong magnetic structure of iron (Leung, $et.al$, 1991, Oliver, & Perdew, 1979). Similarly, it incorrectly predicts the band gap of semiconductor materials (Wang, & Perdew, 1991).

3.5.5 Local Spin Density Approximation (LSDA)

Local Spin Density Approximation (LSDA) is the generalization of the LDA to include the electron spin (Sjostrom, $et.al$, 2013). Here the exact spin-scaling is known but for correction, further approximation is employed (Wang, $et.al$, 1985, Oliver, & Perdew,1979). A spin polarized system in DFT employs two spin densities $[n_\uparrow]$ and $[n_\downarrow]$,

$$E_{xc}^{LDA}[n_\uparrow, n_\downarrow] = \int \delta r n(r) \epsilon_{ex}(n_\uparrow, n_\downarrow). \tag{3.25}$$

The exact result of the exchange energy is known in terms of the spin unpolarized functional,

$$E_{xc}^{LDA}[n_\uparrow, n_\downarrow] = \frac{1}{2}\{E_x[2n_\uparrow] + E_c[2n_\downarrow]\} \tag{3.26}$$

and the spin-dependence of the correlation energy is approached by introducing the relative spin polarization,

$$\zeta(r) = \frac{[n_\uparrow(r) - n_\downarrow(r)]}{[n_\uparrow(r) + n_\downarrow(r)]}. \tag{3.27}$$

3.5.6 Generalized Gradient Approximation (GGA)

Generalized Gradient Approximation (GGA) developed as a result of failure by LDA in situations where the density undergoes rapid changes and for strongly correlated systems where an independent particle picture fails; example in transition metal oxides (TMOs). Though still local, in GGA the gradient of the electronic density is considered

and thus accurate ground-state energies are achieved.

$$E_{xc}GGA[n_{\uparrow}, n_{\downarrow}] = \int \epsilon_{xc}\{n_{\uparrow}, n_{\downarrow}, \vec{\nabla} n_{\downarrow}\} n(\vec{r}) \delta^3 r. \tag{3.28}$$

Compared to LDA and LSDA, GGA tends to improve the total energies, atomization energies, energy barriers and structural energy difference. HF approximation under binds atoms while LSDA over binds them, GGA expands and soften the bonds thus corrects LSDA prediction (Perdew,$et.al$, 1996). However, the expansion and softening of the bonds other times over-correct the LSDA prediction. GGA favours density inhomogeneity. Its depended only on the density and its derivative makes it easy to evaluate them (Oliver, 1979, Perdew, $et.al$, 1996, Vosko, $et.al$, 1980). In a general perspective, GGA has advantages over LDA in that GGA improves ground state properties for light atoms, molecules and clusters (Wang, $et.al$, 1991, Burke, 2012). Also, GGA predicts the correct magnetic properties of $3d$ transition metals example the body centered iron.

Although GGA seems superior to LDA, it too has a number of drawbacks. GGA fails to accurately treat the hydrogen's bond which is clearly manifested through expansion and hence softening of bonds as discussed earlier in this paragraph (Burke, 2012).

3.5.7 Pseudo-potentials

Practical solutions to the self-consistent (SC) Kohn-Sham (K-S) equation are subject to a number of approximations, thus various methods have been developed to be cost effective i.e cause a rapid convergence but without compromising the calculation outcome. Ab *initio* pseudo-potentials method takes into account only valence electrons leaving the deep inner core states and the strong potential binding them to the nuclei making the calculation relatively cheaper compared to full-potential method (Pickett, 1989). It is generally understood that ion cores (deep inner core electrons and nuclei) play minimal role on the properties of solids, but their proper inclusion into the pseudo-potentials creates room for sufficient use of plane-K-points wave basis sets in electronic structure calculation (Hellmann, 1935).

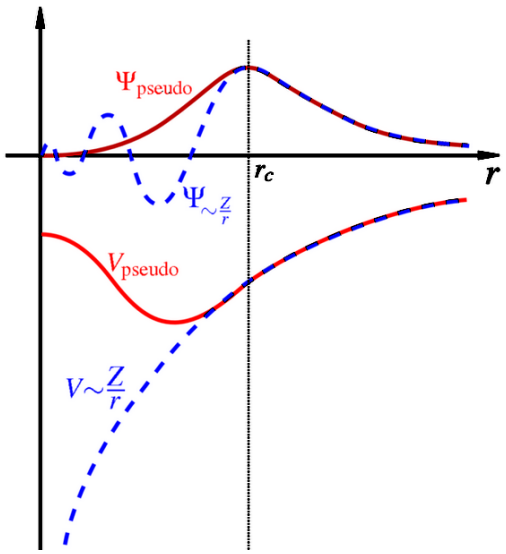

Figure 3.1: Comparison of the wave-function in the Coulomb potential of the nucleus (blue) to the one in the pseudo-potential (red). The real and the pseudo wave-function and potential match at a certain cut-off radius, r_c.

First introduced in 1934 by Hans Hellmann, pseudo-potentials attempt to replace the complicated effects of the motion of the ion core thus the Schrödinger equation is modified with an effective potential term instead of the Coulomb potential (Hellman, & Kassatotsschkin, 1936, Hellman, 1935). Pseudo-potentials simply tend to mimic the behavior of the ion cores of an atom, thus the core states are eliminated and the valence electrons are described by pseudo-wave-function with significantly fewer nodes (Kresse, & Joubert, 1999).

Although the general ideas behind pseudo-potential approach are similar, several procedures are applied in the construction of these pseudo-potential leading to existence of several types of pseudo-potentials. Norm-conserving (NC) and ultra-soft (US) represent the most common forms of pseudo-potentials used in plane-wave electronic structure codes. They allow a basis-set with significantly lower cut-off to be used to describe the electron wave-function and so allows proper numerical convergence with reasonable computing resources (Brust, 1986).

Projector augmented wave (PAW) pseudo-potential (PP) first proposed by Peter E. Bloch in 1994, is a method for reformulating an ordinary Kohn-Sham problem with numerically inconvenient behaviour into a more computationally digestible form, which

involves a different Kohn-Sham problem plus certain corrections (Blochl, 1994, Lee, & Robertson, 2012). It is a unique way of determining the electron structure of materials since it describes well the nodal behavior of the valence electrons wave function and at the same time allowing the inclusion of the upper core states into the SC interaction procedures (Wang, & Perdew, 1991). It is a generalization of the PP and linear augmented-plane-wave (LAPW) methods, and allows for DFT calculations to be performed with greater computational efficiency. Generally the PAW potentials are more accurate than the ultra-soft pseudo-potentials (Kresse, & Joubert, 1999). Two reasons are advanced for this: first, the radial cut-offs (core radii) are smaller than the radii used for the ultra-soft pseudo-potential (US-PP), and second the PAW potentials reconstruct the exact valence wave-function with all nodes in the core region (Vosko, & Nusair, 1980). Since the core radii of the PAW potentials are smaller, the required energy cut-offs and basis sets are also somewhat larger. If such a high precision is not required, the older US-PP can be used. In practice, however, the increase in the basis set size will be usually small, since the energy cut-offs have not changed appreciably for C, N and O, so that calculations for model structures that include any of these elements are not more expensive with PAW than with US-PP (Kresse, & Joubert, 1999). In this study, norm-conserving pseudo-potentials were used to represent the inner core electrons and the nuclei.

3.5.8 The Perdew, Burke, Ernzerhof (PBE) Exchange-Correlation Functional

Designed to satisfy further exact conditions, Perdew-Wang (PW91) functional incorporates some inhomogeneity effects to the exchange and correlation functional while at the same time retaining important features of LSDA (Perdew, 1991). PBE-GGA correlation functional developed in 1996 by Perdew, Burke and Ernzerhof simplified GGA such that it best fulfils many of the physical and mathematical attributes of DFT (Zhao, $et.al$, 2005, Perdew, $et.al$, 1996). PBE functional particularly, satisfies the Lieb-Oxford bound, provides the correct linear response of the uniform electron gas with proper uniform scaling and also leads to a smooth PP.

In PBE the enhancement factor of the exchange functional takes the form;

$$F_x^{PBE}(s) = 1 + k - \frac{k}{1 + \frac{\mu}{k}s^2}, \tag{3.29}$$

where, k=0.804 is set to the maximum value allowed by the local Lieb-Oxford bound [Zhao, Y., $et.al$, 2005] on E_{ex} and =0.21951 is set to cover the linear response of a uniform gas such that the effective gradient for exchange cancels that for correlation. The exchange energy is approximated as;

$$E_x^o = \Sigma_\alpha \int dr F_{x\sigma}^{PBE} \rho_\sigma \nabla \rho_\alpha \{\sum_{i=0}^{m} a_i W_\tau^i\}, \tag{3.30}$$

where, W_τ is a function of τ_σ suggested by Burke because it reduces to zero for a uniform electron gas, but becomes negative in regions of de-localized one- electron exchange hole. The static correction contribution to the exchange functional must be different in such negative-W_τ regions, typically associated with fractionally occupied single orbitals, than in more typical regions where $W_\tau \approx 1$. As pointed by Burke, the density based exchange is still not correct for weak electron-electron coupling which can be corrected by mixing a small percentage of X of HF exchange (Hehre, 2003);

$$E_x = \{1 + \frac{x}{100}\}E_x^o + \frac{x}{100}E_x^{HF}. \tag{3.31}$$

However, the numerical performance of PBE is unsatisfactory for total atomic energies and thermodynamic properties of molecular systems.

3.6 DFT+U Approximation

Over de-localization of electrons especially for localized d and f states of TM and TMOs is a serious failure of LDA and GGA (Anisimov, $et.al$, 1997). At the moment all available exchange-correlation functionals including LSDA and GGA fails in describing the exchange-correlation energy of the system with a strong tendency of localization and interaction of electrons. As a matter of fact LSDA and its failure in strongly correlated

oxides is associated with the inadequacy in describing the strong Coulomb repulsion between $3d$ and $4f$ electrons localized on metal ions.

LDA and its extensions underestimates the local magnetic moments and tendency to favour high-spin ground states in such metals and the insulating gap in cases where it is related to electron localization. Underestimation of the exchange splitting induced by local magnetic moments leads to the underestimation of the gap in the LDA and GGA due to the absence of the derivative discontinuity with respect to orbitals occupancy in the exact exchange-correlation functional. Thus, incorporating the on-site Coulomb interaction term, U, into the exchange-correlation functional is desirable.

DFT+U also known as LDA+U or GGA+U formulated in 1997 by Anisimov, $et.al.$, is used in the description of strongly correlated electron system especially in TM and TMOs (Anisimov, $et.al$, 1997). DFT+U treats the on-site Coulomb interaction of localized electron, which is not correctly described by LDA or GGA with additional Hubbard-like term. Due to the simplicity of its expression and its low computational cost, only marginally larger than the standard DFT calculation, DFT+U has rapidly become a popular approach in the $ab\ initio$ calculations. Based on the corrective functional, DFT+U is formulated to improve the description of the ground-state of correlated systems (Perdew, $et.al$, 1996). The main idea of DFT+U is to separate the electrons into two subsystems; localized d or f electrons for which the Coulomb interaction is taken into account by the model Hamiltonian and de-localized s and p electrons which could be described by using orbital-independent one-electron potential. DFT+U is usually thought as an explicit mean-field treatment of the exchange-correlation energy contributed by the correlated sites within the Hubbard model. It also includes the double counting correction to take into account that contribution which is already included in the LDA term. The Hubbard term , U, is the effective interaction parameter characterizing the on-site Coulomb repulsion between d f electrons.

The total energy in LDA+U is written as,

$$E_{LDA} + U[\rho(r)] = E_{LDA}[\rho(r)] + E_{Hub}[n^{I\sigma}_{mm'}] - E_{dc}[n^{I\sigma}], \tag{3.32}$$

where, E_{LDA} , is the approximate DFT total energy functional being corrected, E_{Hub}, is the term that contains the Hubbard Hamiltonian to model correlated states and E_{dc}, is the double counting term. Due to the additive nature of the correction, part of the interaction energy to be modelled, E_{Hub} is eliminated from the E_{LDA}. Thus,

$$E_{LDA} + U[\rho(r)] = E_{LDA}[\rho(r)] + \sum_{I}\{\frac{U}{2}\sum_{m,\sigma\neg m',\sigma'} n_m^{I\sigma'} - \frac{U'}{2}n^I(n^I-1)\}, \quad (3.33)$$

where, $n_n^{I\sigma}$ is the occupation number of localized orbitals identified by the atomic site index I, state index m and spin τ. The Hubbard correction discourages fractional occupation of localized orbitals and favours the Mott hybridization of the electrons on specific atomic states while penalizing the occupation of others. The difference between the potential acting on occupied and unoccupied states approximately equals to U, corresponds to an effective discontinuity correspondence of integers. This discontinuity in the potential is a feature of the exact DFT and is responsible for the creation of the energy gap in the K-S spectrum equal to the fundamental gap of the system (HOMO-LUMO gap) in crystals (Himmetoglu, $et.al$, 2014).

3.7 Basis Set

3.7.1 Overview

A basis set is a set of functions (called basis function) which are combined in linear combination (LC) to create molecular orbitals. For convenience, these functions are typically atomic orbitals centred on atoms. However, theoretically, they can be any function. Plane wave (PW) basis sets are frequently used in material calculations (Balabin, , 2010, Zhakhov, 2013, Levine, 1991). Wave-functions in systems in question are represented as vectors, the components of which corresponds to the coefficients in LC of basis functions in the basis set used and the operators are represented as matrices (tensors of rank two) in the finite basis (Levine, 1991). Note that basis functions are not usually the exact orbitals. If the finite basis is expanded towards an infinite complete set

of function, calculations using such a basis set are said to approach basis set limit. If a basis set is composed of a finite number of atomic orbitals centred at each atomic nuclei within a molecule, then it follows the LCAO ansatz (Balabin, 2010).

A minimum basis set is one in which for each atom in the molecule, a single function is used for each orbital in a HF calculation on the free atom. The common addition to a minimal set is polarization function. This provides additional node for the much needed flexibility within the basis set effectively allowing molecular orbitals to be more asymmetric. This is important considering accurate representation of bonding between atoms because the very presence of the bonded atom makes the energetic environment of the electrons spherically asymmetric.

Another common addition to the basis set is the addition of diffusion function which are shallow Gaussian basis functions which accurately represent the "tail" position of the atomic orbitals which are distant from the atomic nuclei. They are important when considering anions and other large "soft" molecular systems. Both polarization and diffusion functions are usually added to the light atoms.

3.7.2 Plane Basis Set

In plane wave calculations, one always has to define a computational box, even for isolated molecular systems. Typically, finite number of plane wave (PW) functions are used below a specific energy cut-off which is chosen for a certain calculation. PW basis sets are popular in calculations involving periodic boundary conditions (BCs) (Zakhov, 2013). In practice, PW basis sets are used in combination with an "effective core potential" or pseudo-potential (PP) so that the PW are only used to describe the valence charge density (Zakhov, 2013, Moran, $et.al$, 2006). This is because the core electrons tend to be concentrated very close to the atomic nuclei resulting in a large wave-function and density gradients near the nuclei which are not easily described by a PW basis set unless a very high energy cut-off and therefore a small wavelength is used (Thygesen, & Mortensen, 2008).

Since all functions in the basis are mutually orthogonal and not associated with any

particular atom, PW basis sets do not exhibit basis set superposition error (Balabin, 2010, Zakhov, 2013, Levine, 1991, Thygesen, & Mortensen, 2008). Secondly, PW basis set have an advantage in that the derivatives are computationally less demanding to be carried out. Thirdly, they guarantee convergence in a smooth monotonic manner to target wave-function. Additionally, PW basis sets also have a few other advantages over Slater or Gaussian functions. To begin with, the same basis set can be used for all atomic species. Secondly, convergence toward completeness can easily be tested. Lastly, PW do not depend on nuclear positions so, unlike localized basis sets, correction terms are not needed for the calculation of forces (Davidson, & Feller, 1986).

CHAPTER FOUR

COMPUTATIONAL METHODOLOGY

4.1 Introduction

From the early 1960s, experimental techniques such as thermogravimetry and electrical conductivity measurements have been used to study deviations from stoichiometry in bulk TiO_2 as a function of temperature and oxygen partial pressure using reasonable assumptions (Diebold, $et.al$, 1996). However, to this level, limited experimental techniques to explore the nature of defects formation in bulk TiO_2 has led to obscurity in the fundamental understanding of defect formation and diffusion mechanism in the bulk and grain boundaries [He, & Sinnott, 2005). Z-contrast imaging, electron energy loss spectroscopy (EELS) and high resolution transmission electron microscopy (HRTEM) are techniques used to analyze defects and impurities at grain boundaries in oxides. HRTEM and electronic absorption spectroscopy (EAS) studies on Co^{2+} and Cr^{3+} doped nano-crystalline TiO_2 show that the most important process for activating ferro-magnetism in nano-crystalline cobalt-doped involves the creation of grain boundary defects which are identified as oxygen vacancies (Navio, $et.al$, 1996). EELS has demonstrated to be sensitive to the changes in the oxygen concentration and could be used to probe the effect of individual defect on the local electronic structures (Batzill, $et.al$, 2002).

This study uses computer modelling to analyse the structural and electronic properties of isolated point defects in bulk rutile and anatase TiO_2 at ground-state. All the calculations of the ground-state properties of rutile and anatase TiO_2 reported in this work were done using the integrated suite of computer codes for electronic structure calculation and modelling, Quantum ESPRESSO (QE) package (Giannozzi, $et.al$, 2009). The calculations (structural optimization and description) using Quantum ESPRESSO (Quantum opEn Source Package for Research in Electronic Structure Simulation and Optimization) are based on DFT+U and a comparison with DFT. QE uses plane wave

basis set for the expansion of the electronic wave-function and pseudo-potential for the description of the electron-ion interaction for O and Ti atoms. PBE functional form of GGA was chosen for the electron exchange-correlation (i.e difference between the exact total energy of a system and the classical Hartree energy) within DFT.

4.2 DFT and DFT+U Formalism

The interaction between electrons which are identical fermions posses the greatest problem in solving the quantum many-body (M-B) problem described by the Schrodinger equation. To reduce this, the calculations are done at ground-state where the solution of the M-B problem is reduced to a solution of a simpler problem of a single non-interacting electron moving in an effective field. DFT reformulates the total energy in terms of a functional of the charge density of the system, thus the ground state energy of the system is obtained from the ground-state electron density (Giannozzi, $et.al$, 2009). Successful approximations have been discussed in section 3.5 and 3.6 of chapter three of this study including LDA, GGA, LSDA and DFT+U which have allowed practical and quantitatively accurate calculations of ground-state properties. A Hubbard term, U = 5.3 eV was applied on the Ti-$3d$ electrons to modify the strongly correlated interactions.

4.3 Solution to the Self-consisted Kohn-Sham Equation

The effective potential given by equation (3.17) depends on the charge density $\eta(r)$ which is depended on the K-S orbital ψ (r). In the K-S approach, the electron density and the total energy may be obtained by solving an associated system of non-interacting electrons with the same charge as the interacting system. Here, the charge density η(r) is expressed exactly in terms of the sum over particle orbital as given by equation (3.18). Thus, the K-S equation is solved iteratively until a self-consistent solution is arrived at. In practical calculations, the basic approximation lies in the construction of the energy functional itself.

Figure 4.1 presents an SCF scheme. At the beginning an initial guess for the elec-

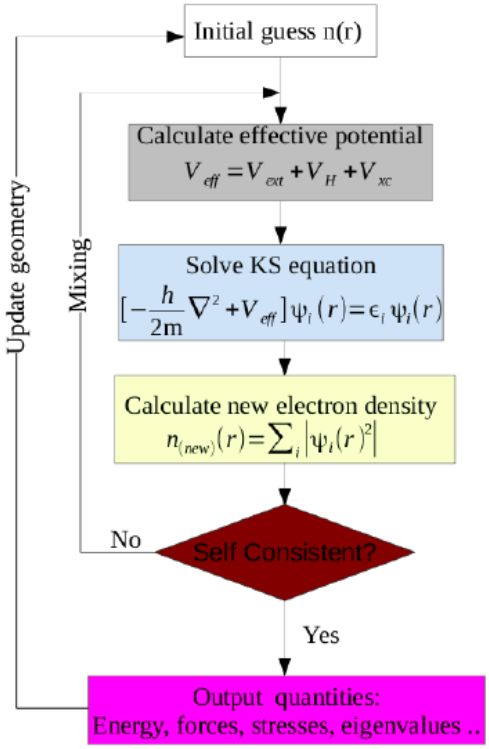

Figure 4.1: Schematic representation of the SC loop for the solution of the K-S Equation.

tron density, which is required for the calculation of V_{eff}(r) is assumed. The diagonalization of the K-S Hamiltonian and the subsequent evaluation of ψ(r) along with total energy (E_{tot}) is then performed. As long as convergence criterion is not fulfilled, the numerical procedure is continued with the last ψ(r) instead of the initial guess. When the criterion is satisfied, various output quantities are computed i.e when self-consistency is achieved for this loop, the electronic part of the system is solved; total energy, forces, etc. can be obtained.

4.4 Structural Optimization

The rutile phase was modelled with a 48 atom super-cell while anatase used a 96 atoms super-cell. VESTA (Visualization system for Electronic and Structural Analysis) software (Monna, & Izumi, 2008) was used to construct the initial super-cell and XCrysDen software (Kokalj, 1999) to visualize these structures and the K-path selection too. XcrysDen package is the crystalline and molecular structure visualization pro-

gram which displays isosurfaces and contours which can be superimposed on crystalline structure and interactively rotated and manipulated. Super-cell structural optimization was done using convergence tests at fixed internal stress. The geometry optimization used the Broyden-Fletcher-Goldfarb-Shannon (BFGS) algorithm with convergence to 5×10^{-5} eV/atom, 0.001eV/Å for the Hellmann-Feynman force on each atom and stress of 0.2Gpa. The optimized cell parameters are summarized in figures A.$_1$ & A.$_2$ and B.$_1$ & B.$_2$ on appendices 1 and 2 respectively.

4.5 K-Point Optimization

The experimental lattice parameters, a=b=4.594 Å and c=2.959 Å for bulk rutile and a=b=3.784 Å and c=9.517 Å for bulk anatase were used to optimize the K-point. The kinetic energy cut-off was fixed at 30 Ry for both rutile and anatase, a value not too low to compromise on the accuracy of the calculations yet not too high to make the calculation computationally expensive. The K-points were automatically generated using the Monkhost-Pack scheme which ensures that the irreducible parts of the Brillouin zone (BZ) are integrated over a set (mesh) of uniformly spaced high symmetry points. Since TM like Ti are known to require a large K-point, the grid mesh was varied from 2×2×2 to a dense of 15×15×15. The results of the calculated total energy against K-point are shown figures A.$_4$ and B.$_4$ in the appendices one and two. From these results, a grid of 5×5×5 was chosen for rutile and 4×4×2 for anatase to sample out the path between the high symmetry points within the Brillouin zone.

4.6 Pseudo-potentials

This study used norm-conserving pseudo-potentials (NC-PPs) and the results compared with those from ultra-soft pseudo-potentials.

4.6.1 Norm-conserving PP

Norm-conserving pseudo-potentials were used since they are the most transferable thus capable of describing the scattering properties of an ion in a variety of ways. They are also more accurate and non-local. However, they make calculations to take relatively long to achieve convergence since they require a relatively high cut-off energy. Hence, NC-PPs are a bit more expensive as they requires a bigger CPU and RAM.

4.6.2 Ultra-soft PP

Confronted by the requirement of large cut-off energies by NC-PPs making the calculations using NC-PPs to be a bit expensive, Vanderbilt in 1990 introduced ultra-soft PP. US-PP allows calculations to be performed with a relatively low cut-off energy for the plane-wave basis set. US-PPs are made to be soft by removing charge associated with core orbitals from the core region i.e they are build to relax the norm-conserving constraints thus, reducing the necessary basis-set size. Thus, US-PPs are relatively cheaper compared to NC-PPP. However, US-PP's accuracy is slightly compromised.

4.7 Plane Wave Energy Cut-off Optimization

The kinetic energies cut-off (ecut) varying from 20 Ry to 90 Ry for rutile and 30 Ry to 120 Ry for anatase were applied with a relaxed system. For each case the charge density cut-off (ecutrho) was chosen to be four times the $ecut$ as suggested by the use of norm-conserving pseudo-potentials. The cut-off energy for convergence was achieved at 50 Ry and 70 Ry for rutile and anatase respectively and thus, the values were chosen for the expansion of the K-S function for O and Ti atoms. Convergence was considered to have been achieved when the difference between the successive self consistent steps was less than 10^{-7} Ry. The results of total energy against ecut are shown in figures A.$_3$ and B.$_3$ in appendices one and two respectively.

4.8 Brillouin Zone (BZ)

A Brillouin zone is a Weigner-Seitz primitive cell in the reciprocal lattice (Kittel, 2002). A set of points around a point in space that are closer to that lattice point than to any other lattice points is the Weigner-Seitz cell. These sets of points are referred to as the K-path (see figure 4.2). A vivid geometrical interpretation of the diffraction conditions i.e the description of the electron energy band theory and of the elementary excitation of other kinds is given by the BZ. To plot the band structure of both rutile and anatase, the high symmetry points and path was generated using the X-window Crystalline and Molecular Structure Visualization (XCrysDen) program (Kokalj, 1999, Setyawan, & Curtarolo, 2010, Giannozzi, $et.al$, 2009). The K-path and points chosen in this study are shown in **Figure 4.2** and **Table 4.1**

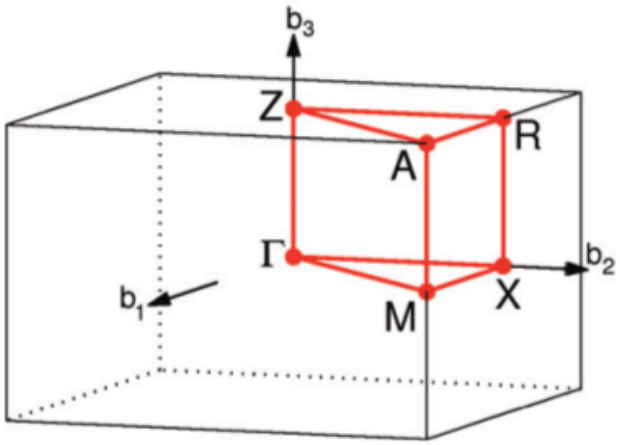

Figure 4.2: BZ and K-path ($\Gamma - X - M - \Gamma - Z - R - A - Z - R - A$) **for the tetragonal rutile and anatase structures.**

Table 4.1: High symmetry points for rutile and anatase.

a*	b*	c*	path
0.000	0.000	0.000	Γ
0.500	0.500	0.500	A
0.500	0.500	0.000	M
0.000	0.500	0.500	R
0.000	0.500	0.000	X
0.000	0.000	0.500	Z

4.9 Energy Band Gap Determination

Due to the fact that most of the applications of TiO_2 have a close relationship to either light absorption or transparency (as discussed in Chapter one) (Strunk, $et.al$, 2010, Di Valentin, $et.al$, 2004, Schleife, $et.al$, 2013, Matthissen, 2007) and more so electrical conductivity, determination of its energy band gap is key in this study. The band gap was calculated both with and without the U term in order to establish the manner in which the U term varies the band gap. In solid state Physics, fundamental band gap is the energy difference between the CB edge and the VB edge (Neamen, 2006). An electron can transit from the VB to the CB either directly or indirectly by absorbing a phonon (heat) or a photon (light). Direct band gap occurs when the crystal momentum (K-vector in the Brillouin zone) of electrons and holes is the same in both the VB and the CB, thus an electron can directly emit a photon (DolTPoMs, $www.doltpoms.ac.uk$). On the other hand, in an indirect gap, a photon cannot be emitted since the electron must pass through an intermediate state(s) (mid-gap state(s)) and transfers the momentum to the crystal lattice (DolTPoMs, $www.doltpoms.ac.uk$).

It is well documented that both LDA and GGA give rise to an underestimated value of the band gap of semiconductors and insulators (Perdew & Levy, 1983). The K-S

band gap is given by;

$$E_{gap}^{KS} = \epsilon_{N+1}^{KS}(N) - \epsilon_{N}^{KS}(N). \tag{4.1}$$

But the calculated difference of the K-S band gap between HOMO and LUMO of an N-electron system is given by;

$$E_{gap}^{KS} = \epsilon_{N-1}^{KS}(N) - \epsilon_{N}^{KS}(N), \tag{4.2}$$

$$E_{gap}^{KS} = [\epsilon_{N+1}^{KS}(N+1) - \epsilon_{N}^{KS}(N)] - [\epsilon_{N+1}^{KS}(N) - \epsilon_{N+1}^{KS}E(N)], \tag{4.3}$$

$$E_{gap}^{KS} = E_{gap} - \Delta XC, \tag{4.4}$$

where: ΔXC is the K-S potential due to the infinitesimal variation of the density which is rigid and entirely due to the discontinuity in the derivation of the XC energy functional.

Under many circumstances, point defects and impurities introduce defect levels in the band gap or near the band edges of the semiconductor. These defect levels can be theoretically characterized by K-S eigenvalues and defect transition levels (ionization levels) methods. However, the K-S eigenvalue does not account for the excitation aspect, thus only defect transition levels can be compared directly with experimental work. In this work, U=5.3 eV (Morgan, & Watson, 2007, Yang, $et.al$, 2014) has been used in the band-gap calculation and it has further been established that the band-gap is predicted to be much closer to the experimental value (will be discussed in chapter 5) and a reasonable defect localization description is offered.

4.10 Defect Calculations

Crystalline solids exhibit periodic crystal structures with positions of the atoms or molecules occurring in fixed repeated distances which are determined by the unit cell parameters. However, the arrangements of these atoms or molecules in most crystalline material is

not so perfect. Crystallographic point or extended defects interrupt this regular pattern resulting in the breaking of the symmetry within this crystals. Vacancies, interstitials and Frenkel pairs which are the main focus of these study causes this disruptions and occur only at or around a single lattice point. In calculating the defect concentration, the following formula was used,

$$\%\, defect\ concentration = \frac{No.\ of\ defective\ atom(s)}{Total\ No.\ of\ atoms\ in\ a\ supercell} \times 100\%. \quad (4.5)$$

4.11 Defect Formation Energies

Formation energies are important criteria of evaluating the relative difficulty for the in-cooperation of dopants/defects into the host lattice and therefore the relative stability of the doped/defective systems. In this study, only charge neutral structures have been considered and thus, the formulation of the formation energies does not include the chemical potential of electrons. The equations used in the calculations of the defect formation energies (DFEs) are well described in section 5.6 of chapter five on the Formation Energies section.

CHAPTER FIVE

RESULTS AND DISCUSSIONS

5.1 Introduction

This chapter presents the theoretical results obtained from the current study. Findings on the pristine and defective anatase TiO_2 super-cells are reported. The structural and electronic properties of anatase titanium dioxide as well as the defect formation energies are presented. Findings on rutile phase have been presented earlier in each stage as a precursor to the findings of anatase since rutile has been studied quite extensively.

5.2 Structural Optimization

Tables 5.1 and 5.2 show the calculated lattice parameters at ground state for the tetragonal rutile and anatase, TiO_2 respectively. These are compared with available results and they show a very good agreement with those reported by other studies done using different theoretical codes (VASP, CASTEP) (Batzill, $et.al$, 2002, He, & Sinnott, 2005, Diebold, $et.al$, 1996, Bryan, $et.al$, 2005) as well as experimental approaches (Zhang, $et.al$, 2014, Zhang, $et.al$, 2008). In particular, the cell volumes are very close to the experimental value deviating only by $+0.95\%$ for rutile and $+3.3\%$ for anatase. The increased volume as depicted by the positive deviation is an indication of the difference between the purity of the ideal computer modelled TiO_2 structure compared to one done experimentally. Here, the later though termed pristine will always have some defects even if in minute quantities. The increased volume as expected proportionally reduced the bulk modulus, a fact that is corroborated by the negative deviation of the value of B_0 (-0.926%) for rutile phase and B_0 (-2.23%) for anatase phase of TiO_2. The deviations shown in Tables 5.1 and 5.2 are based on the comparison with the corresponding experimental values.

Table 5.1: Calculated DFT+U Lattice parameters for perfect rutile TiO_2.

Property	*Calculated*	*Exp Value*^{a}	*Literature*^{b}	*Literature*^{c}	*% dev*	*Ref*
$Cell\ Vol(\AA^3)$	63.026	62.434	64.840	62.220	$+0.948$	$(Navio,\ et.al, 1996)^a$,
$a_o(\AA)$	4.630	4.594	4.653	4.584	$+0.784$	$(Batzill, et.al, 2002)^b$,
$\frac{c}{a}$	0.635	0.644	0.637	0.637	-1.400	$(He, \& \ Sinnott, 2005)^c$
$B_0(GPa)$	214.0	216.0	209.3	226.7	-0.926	

Table 5.2: Calculated DFT+U Lattice parameters for perfect anatase TiO_2.

Property	*Calculated*	*Exp Value*^{d}	*Literature*^{e}	*Literature*^{f}	*% dev*	*Ref*
$Cell\ Vol(\AA^3)$	140.87	136.24	139.84	138.27	$+3.30$	$(Zhang, et.al, 2008)^d$
$a_o(\AA)$	3.784	3.784	3.763	3.785	$+1.32$	$(Diebold, et.al, 1996)^e$,
$\frac{c}{a}$	2.601	2.515	2.618	2.550	$+3.42$	$(Bryan, et.al, 2005)^f$
$B_0(GPa)$	176.2	179.0	172.11	173.4	-2.23	

The same trend is observed for the lattice constants a and $\frac{c}{a}$. In the rutile phase, the lattice constants a and $\frac{c}{a}$ are observed to deviate from the experimental value by $+0.784\%$ and -1.4%, respectively while in anatase the values are found to deviate by $+0.132\%$, and $+3.42\%$ respectively. Figures 5.1 and 5.2 show the optimized super-cells for rutile (48 atoms) and anatase (96 atoms) phases of TiO_2 whereby, the apical d_{ax} and equatorial d_{eq} bonds are indicated.

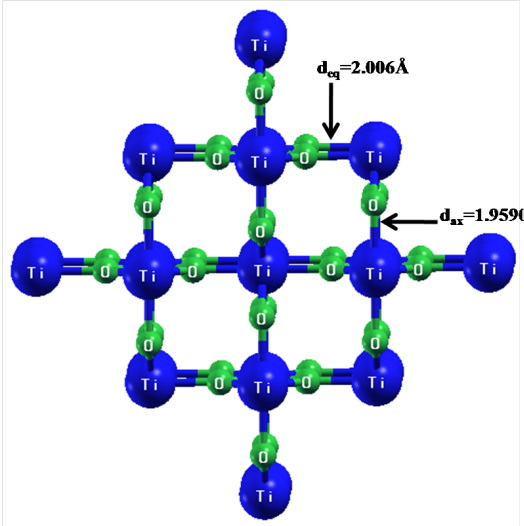

Figure 5.1: Optimized Rutile TiO_2 super-cell.

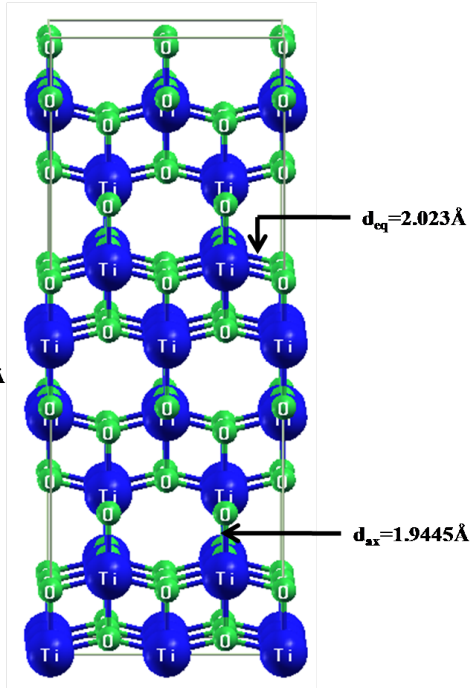

Figure 5.2: optimized anatase TiO_2 super-cell.

A summary of the calculated and changes occurring in the bond length and bond angles of the two phases, rutile and anatase, TiO_2 are shown in Table 5.3 for the pristine and defective super-cells (see page 53). In pristine rutile, the apical bond length, (d_{ax}) was found to contract by -1.16% while the equatorial bond length (d_{eq}) elongate by $+3.0\%$ from the corresponding experimental values. Similarly, d_{ax} and d_{eq} for pristine anatase contracted and elongated by -1.2% and $+6.0\%$, respectively, from the experimental values. These changes in the d_{ax} and d_{eq} bond lengths were attributed elsewhere to the reduction in the $O-O$ repulsion (Fahmi, $et.al$, 1993). In general, the anatase phase was found to experience greater changes in the bond length following the relaxation as seen in **Table 5.3**.

The defects considered in this study and reported in Table 5.3 include O_I, O_V, Ti_I, Ti_I, O_F and Ti_F. Recent studies have shown that reducible metal oxides tend to accommodate a large degree of sub-stoichiometries whose net result is the adverse effect on the physical-chemical properties of these materials. Intrinsic point defects just like impurities in pristine crystals have been shown to lead to local structural disorders that modify the bonding configuration around the defect site depending on the nature and position of the defect (Wang, $et.al$, 2012). However, such studies have been limited and hence the need for a more detailed study as presented in this work.

The pristine TiO_2 rutile has a symmetric structure with each Ti atom bounded to four nearest (four-fold coordinated) and two nearest (two-fold coordinated) oxygen neighbours (Diebold, 2003). The calculated rutile $Ti-O$ distances of 1.9590 Å and 2.0060 Å for the apical and equatorial bonds, respectively, compare relatively well with other reported values, 1.95 Å and 1.99 Å (Wang, $et.al$, 2012). In anatase, Ti atoms strongly repel their Ti nearest neighbours and attract a large number of O neighbours (Diebold, 2003). Each Ti atom has six O neighbours but only four next-nearest neighbours hence the great stability in anatase (Na-Phattalung, $et.al$, 2006). Its calculated $Ti-O$ apical bond length of 1.9563 Å compares relatively well with experimental value of 1.9650 Å, while its equatorial bond length of 2.050 Å differed by 0.1230 Å from the experimental value of 1.9370 Å.

The structural distortions are investigated in this study by the analysis of the $Ti-O$ distances and the $Ti-O-Ti$ and $O-Ti-O$ bond angles for both perfect and defective super-cells. Introduction of points defects within the TiO_2 systems was found to affect the bonding environment around the defects site rather significantly. Both Schottky and Frenkel defects caused defect concentration levels of 2.083% and 1.042% for rutile and anatase phases, respectively, in this work. Removal of one oxygen atom (O_V) from the TiO_2 rutile (2.083%) and anatase (1.042%) crystals resulted in two unpaired electrons and three Ti dangling bonds (Diebold, 2003). The largest distortion of about $+12.3\%$ occurred in the rutile phase of TiO_2 upon introduction of titanium Frenkel defect and was observed in the equatorial $Ti-O$ bond length. Similarly, oxygen Frenkel defect led to a contraction of -11.2% on the apical $Ti-O$ bond. In terms of bond angles, oxygen Frenkel defect resulted in the $Ti-O-Ti$ angles changing between $99.933^0-88.86^0$ while the titanium Frenkel defect led to a change of between $143.49^0-131.04^0$ around the defect site.

A similar trend like that observed in the rutile phase is recorded in anatase, where titanium Frenkel defect resulted into an elongation of $+8.9\%$ on the equatorial $Ti-O$ bond length while the oxygen Frenkel defect caused a contraction of -8.0% on the apical bond length. For bond angles, both $Ti-O-Ti$ and $O-Ti-O$ angles were found to change upon the introduction of titanium Frenkel defect which gave the largest angular distortion. Anatase has the largest distortion of the $Ti-O-Ti$ bond angles following a similar trend as rutile. It is observed that oxygen Frenkel defect lead to angular changes of between $103.81^0-93.59^0$ and titanium Frenkel defect resulting to changes of between $152.39^0-176.05^0$. In both phases, oxygen interstitial and oxygen vacancy defects led to the greatest angular and bond length deviation.

Table 5.3: Calculated DFT+U bond lengths and angles for pristine and defective super-cells of rutile and anatase titanium dioxide.

Defect Type	Rutile				Anatase			
(l)2-9	Ti-O (Å)		Bond Angles (^{0})		Ti-O (Å)		Bond Angles (^{0})	
Pristine	1.9590_{Ax}	2.0060_{Eq}	$99.95_{Ti-O-Ti}$	131.94_{O-Ti-O}	1.9563_{Ax}	2.0502_{Eq}	$103.81_{Ti-O-Ti}$	152.39_{O-Ti-O}
Exp. Value	1.9820_{Ax}	1.9470_{Eq}	$98.93_{Ti-O-Ti}$	130.01_{O-Ti-O}	1.9650_{Ax}	1.9370_{Eq}	$99.93_{Ti-O-Ti}$	$131.04_{Ti-O-Ti}$
% deviation	-1.16	3.03	1.03	1.50	-0.44	5.44	3.88	16.3
O_V	$1.9590 - 2.0001_{Ax}$	$1.8610 - 2.1330_{Eq}$	$95.69 - 132.11_{Ti-O-Ti}$	$129.13 - 143.05_{O-Ti-O}$	$1.8180,- 1.9906_{Ax}$	$1.7241 - 2.1700_{Eq}$	$75.66- 149.91_{Ti-O-Ti}$	$114.92 - 148.51_{O-Ti-O}$
O_I	$1.9577-2.0003_{Ax}$	$1.9214-2.1089_{Eq}$	$91.06 - 129.82_{Ti-O-Ti}$	$119.09 - 138.19_{O-Ti-O}$	$1.8512-2.0003_{Ax}$	$1.8001 - 2.1901_{Eq}$	$77.94 - 148.52_{Ti-O-Ti}$	$111.27 - 157.34_{O-Ti-O}$
Ti_V	$1.7830 - 2.0086_{Ax}$	$1.9322 - 2.1089_{Eq}$	$93.07 - 134.12_{Ti-O-Ti}$	$102.08 - 137.42_{O-Ti-O}$	$1.8102-1.9989_{Ax}$	$1.9801 - 2.1120_{Eq}$	$89.54 -142.06_{Ti-O-Ti}$	$116.69 - 134.24_{O-Ti-O}$
Ti_I	$1.8611 - 2.0193_{Ax}$	$1.9251 - 2.1701_{Eq}$	$92.16 - 133.63_{Ti-O-Ti}$	$107.07 - 128.83_{O-Ti-O}$	$1.8803 - 2.0014_{Ax}$	$1.9771 - 2.2113_{Eq}$	$81.44 - 134.05_{Ti-O-Ti}$	$115.02 - 136.70_{O-Ti-O}$
O_F	$1.9591 - 2.0394_{Ax}$	$2.0806 - 2.2069_{Eq}$	$87.19 - 113.43_{Ti-O-Ti}$	$113.10 - 141.87_{O-Ti-O}$	$2.0002 - 2.2137_{Ax}$	$1.9982 -2.1870_{Eq}$	$93.59 - 137.01_{Ti-O-Ti}$	$109.22 - 163.83_{O-Ti-O}$
Ti_F	$1.9808 - 2.0069_{Ax}$	$2.0720 - 2.2301_{Eq}$	$76.48 - 122.32_{Ti-O-Ti}$	$123.64 - 150.45_{O-Ti-O}$	$1.9815 - 2.2010_{Ax}$	$1.9665 - 2.2039_{Eq}$	$79.74 - 146.82_{Ti-O-Ti}$	$101.07 - 176.05_{O-Ti-O}$

5.3 Electronic Band Structure of Pristine TiO_2 Crystals

This section presents the electronic properties of both the pristine and defective super-cells of the two phases of TiO_2. Pristine super-cells provide salient information of the stoichiometric properties of TiO_2. It has already been pointed out that both impurities and intrinsic point defects lead to structural disorders in varying degrees. Such changes are expected to be accompanied by rearrangements of the electronic charge densities, thereby changing the electronic structural arrangements of the respective metal oxides. This in turn affects the applications of the material especially in the electronic conductivity.

5.3.1 Electronic Band Structure of Pristine Rutile TiO_2 Crystal

Figure 5.3 shows the PDOS of rutile and figure 5.4 shows the band structure of the rutile TiO_2 together with its corresponding density of states. These results show plots of DFT+U and plain DFT calculations. The lower part of the valence band, is characterized by mostly $O-1s$ orbitals with a little hybridization with the $Ti-2p$ and $Ti-1s$ states, respectively, while the upper part of the VB is attributed to a very strong hybridization between $O-2p$ and $Ti-3d$ states. The hybridized $O-2p$ and $Ti-3d$ states within the VB are responsible for the strong bonding observed in rutile (Wang, $et.al$, 2014). The lowest part of the conduction band, CB is constituted mainly of $O-2p$ and $Ti-3d$ states. This observation suggests that the excitation across the band gap involves both $O-2p$ and $Ti-3d$ states. However, it is worth noting that $O-2p$ states dominates the behavior of the VB while $Ti-3d$ states characterizes the behavior of the CB. The finding of $O-2p$ states dominance at the top of the VB and $Ti-3d$ states on the bottom of the CB is supported by many other reported studies (Stausholm-Møller, $et.al$, 2010).

In pure rutile TiO_2, this study predicts a direct band gap of $2.12\ eV$ at the Γ point using pure DFT (see **Figure 5.4**. This value compares relatively well with that of $2.24\ eV$ reported by Mwonga (2014) who used ultra-soft pseudo-potentials. The Γ- point CBM is almost at the same level with the local R minima (which is $0.03\ eV$ higher in energy).

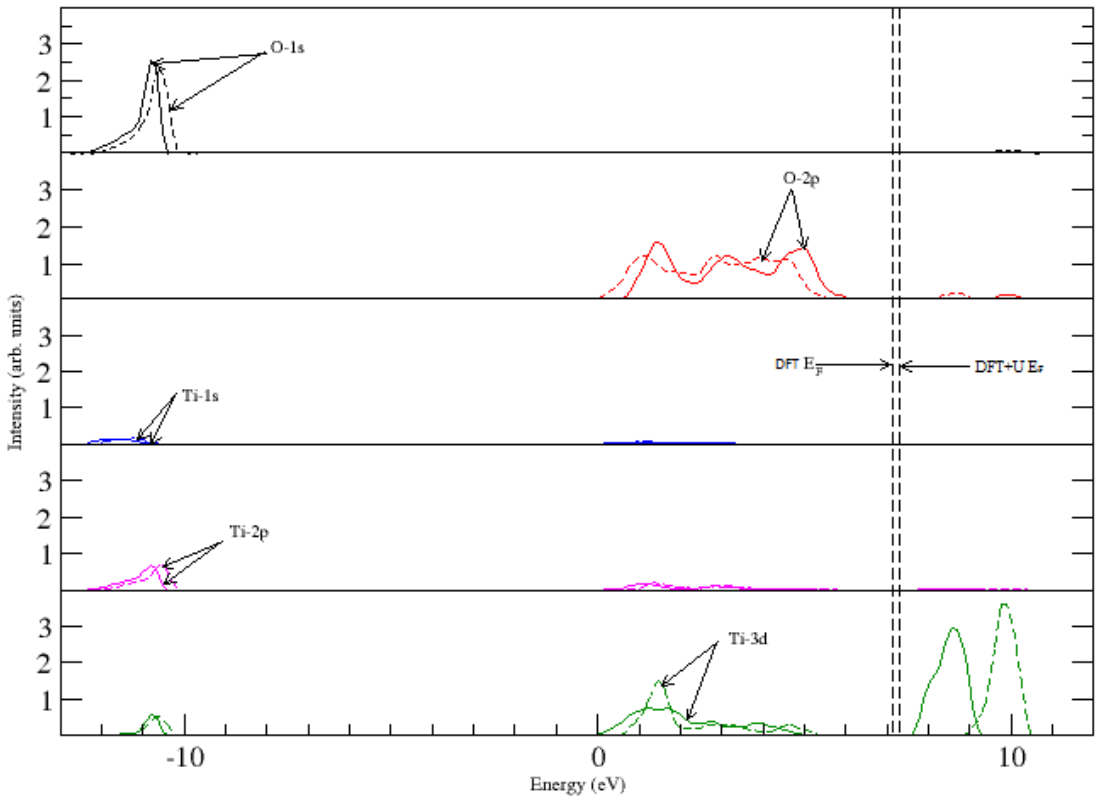

Figure 5.3: PDOS for pristine rutile TiO_2 calculated using DFT (solid) and DFT+U (dashed).

As expected from DFT calculations, the value of $2.12\ eV$ is an underestimation of about $\sim 29.33\%$ compared to the experimental value of $\sim 3.0\ eV$ which arises from lack of consideration of the discontinuity in the exchange-correlation (XC) energy functional within the DFT framework (He, & Sinnott, 2005, Wang, $et.al$, 2014). Using $DFT+U$ formalism, a direct band-gap along the same high symmetry point is observed as was for the case of DFT. However, the value of the band gap increased to $2.89\ eV$, a value that agrees well with another one of $2.86\ eV$ which is reported from a recent study (Stausholm-Møller, $et.al$, 2010). Though close, such a value is still an underestimated by $\sim 3.667\%$, from the experimental value. This shows that the inclusion of the Hubbard term, U, in the correction of DFT band gap does indeed increase the DFT band gap of the rutile TiO_2.

The pristine rutile TiO_2 was found to have a wide valence band (VB) of 5.60 eV and narrow conduction band (CB) of 1.65 eV in width (see **Figure A.5** in the appendix) which compares relatively well with values of 5.62 eV and 1.90 eV, respectively, re-

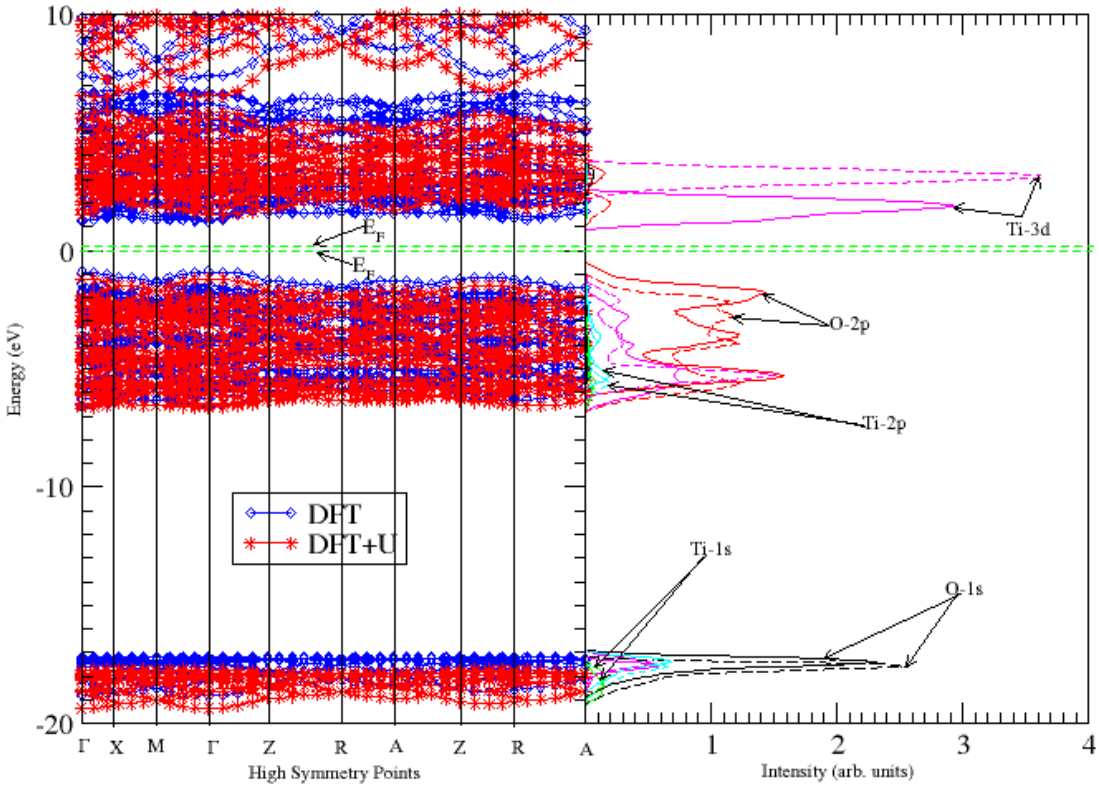

Figure 5.4: Band & PDOS Structure of pristine rutile TiO_2 calculated using DFT(solid) and DFT+U (dashed).

ported by other theoretical studies (Bryan, $et.al$, 2005). The position of the VB and CB of materials such as TiO_2 is determined by the on-site electrostatic potential and optical dielectric response (Lee, $et.al$, 2012). Comparing the band structure and the density of states (DOS) as shown in **Figure A.5**, it shows that most of the CB is empty.

5.3.2 Electronic Band Structure of Pristine Anatase TiO_2 Crystal

Figures 5.5 and 5.6 show the calculated PDOS and band structure of pristine anatase. The band structure was obtained along the high symmetry path $\Gamma \rightarrow X \rightarrow M \rightarrow \Gamma \rightarrow Z \rightarrow R \rightarrow A \rightarrow Z \rightarrow R \rightarrow A$ which is similar to that followed in the study of the rutile phase. A group of well separated bands was observed in anatase as presented in figure 5.5. The upper VB edge is dominated by $O-2p$ orbitals with a little contribution from $Ti-3d$ states. The CB was found to be dominated by $Ti-3d$ states with a little hybridization by $O-2p$ states. This suggests that in pristine anatase, the observed cross band gap excitation involves both $O-2p$ and $Ti-3d$ states.

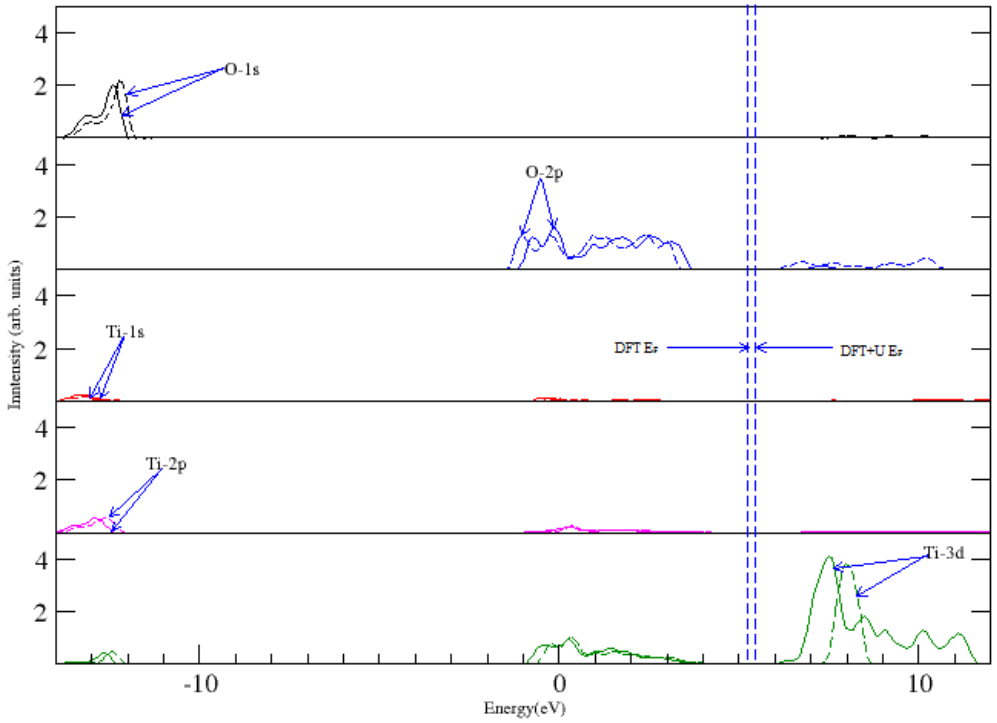

Figure 5.5: PDOS for pristine anatase TiO_2 calculated using DFT (solid) and DFT+U (dashed).

Using plain GGA-PBE calculations, pristine anatase was found to have an indirect band gap of $2.39\ eV$ from $\Gamma(1.465,\ 3.757)$ to $Z(1.902,\ 6.148)$ which is consistent with other available theoretical studies done within the same conditions. This value compares relatively well with a value $2.44\ eV$ reported by Mwonga (2014) who used ultra-soft pseudo-potentials while this study uses NC-PPs. The indirect band gap value

of 2.39 eV is underestimated by $\sim$ 26.01% compared to the experimental value of 3.23 eV due to the shortcomings attributed to DFT [Diebold, U., 2003] as mentioned earlier. Since this study intended to determine the energy band gaps as well mid gap states exactly as possible, DFT+U was also performed to try and correct the limitations associated with DFT in predicting the energy gaps (Anisimov, $et.al$, 1997). Using a U term of 5.3 eV, the band gap was found to increase to 3.01 eV, a value that differed from the experimental data by -6.81%. A direct band gap of 3.11 eV along Γ high symmetry point is also observed in this study.

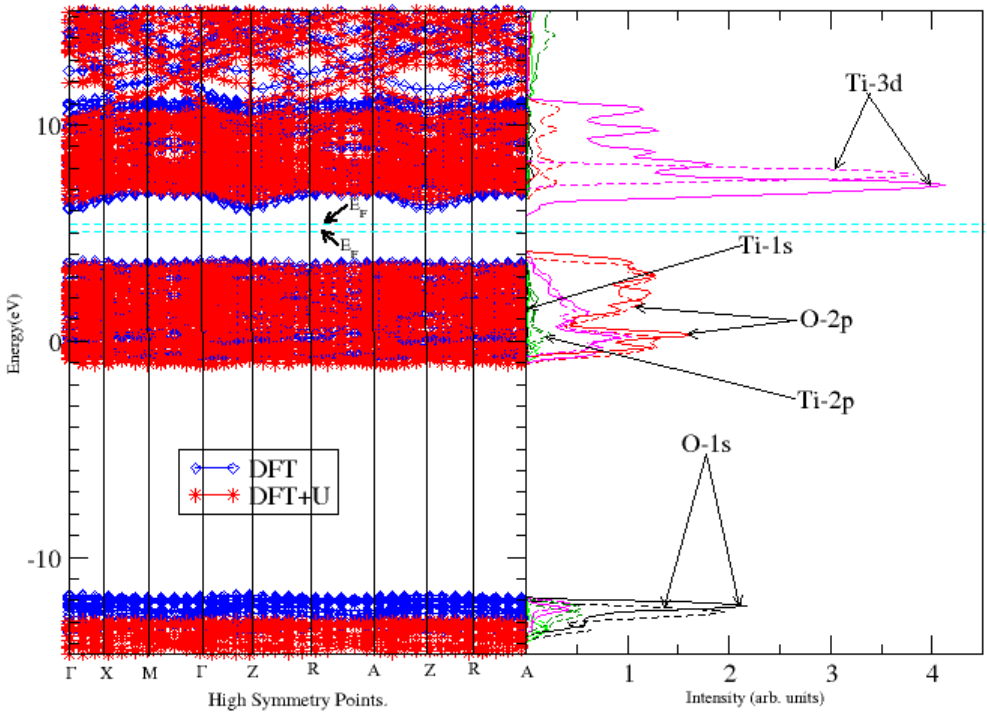

Figure 5.6: Bands and PDOS for pristine anatase TiO_2 calculated using DFT (solid) and DFT+U (dashed).

A VB width of 4.69 eV and a narrow CB of 1.96 eV were observed in this study and compares well with other theoretical studies although the CB value differ slightly from a value 2.35 eV reported by Mwonga (2014). The VB and CB width for anatase in this study when compared with the results of rutile TiO_2 indicates that anatase has almost the same VB and CB band width characteristics as rutile. The VB value of 4.69 eV compares relatively well with a value 4.75 eV (Liu, & Jaroniec, 2010) obtained experimentally, a large part of the CB being largely empty. Additionally, the bands and DOS

structures depicts a broad $Ti - 3d$-like bands in the CB that are distinctively divided in two sub-bands, a feature that was also observed in rutile TiO_2. In the VB, the $O - 2p$-like states are composed of a weak two peak separation which is much less predominant in anatase as compared to the case of rutile. The high bonding energy states are mainly $O - 1s$ and $Ti - 1s$ as seen in **figure 5.5** which is an observation that is quite similar to that of rutile as can be seen in figure 5.3. A closer look at the numbers of the bands (**Appendix figures A.5 and B.5**) indicates that anatase has more bands than rutile as can be deduced from the intensity of the bands in each figure. This is attributed to the large number of atoms per super-cell which is 96 atoms for anatase and 48 atoms for rutile. Similarly, it was observed that the size of the CB in anatase phase is slightly wider than that of the rutile phase (1.96 eV and 1.65 eV respectively). The intensity of the peaks in the PDOS for anatase is much higher than that of the rutile structure due to the large number of atoms in anatase than rutile.

5.4 Electronic Band Structure of TiO_2 Crystals With Defects

Due to the increased energy band gap obtained from the DFT+U approach unlike the DFT method, only the bands and PDOS for DFT+U will be considered since this corresponds well with the reported experimental band gaps.

5.4.1 Electronic Band Structure of Rutile TiO_2 Crystals With Defects

Following the introduction of defects within the rutile super-cell, new defect level state(s) within the band-gap were observed as well as change in the position of the Fermi level. Introduction of oxygen vacancies (O_V) was found to lead to an upwards shifting of the Fermi level (E_F) by $\sim 0.6\,eV$ (see **Figure 5.7**) due to the charge redistribution within the material. It also resulted in the formation of two shallow defect states within the band gap located at $0.75\,eV$ below the CBM. This agrees well with the findings of Hendrich $et.al$ (1976) and also Yu and Halley (1995) who reported observing a feature between $0.7 - 1.0\,eV$ below the CBM. The charge density of these states is localized around two of the three titanium atoms next to the vacancy (Lee, $et.al$, 2012, Stausholm-Møller, $et.al$, 2010) and these local defect levels are fully occupied. The presence of oxygen vacancies results in the reduction of Ti^{4+} to Ti^{3+} due to the charge imbalance. The position of the Fermi level close to the CB is an indication of the *donor*-type conductivity and the charge state of the oxygen vacancy is most likely zero. Scanning tunneling spectroscopy (STS) studies have also reported the formation of a defect level causing *n*-type conductivity and localized downward band bending of the CB (He, & Sinnott, 2005), findings that suports *donor*-type conductivity due to the presence of oxygen vacancies.

Both $O - 2p$ and $Ti - 3d$ states as can be seen in **Figure 5.7** are responsible for the location of the new states on this figure due to rearrangement of charge following the removal of the oxygen atom. The shape of $PDOS$ shows that these states causes a slight broadening of the CB (by ~ 0.227 eV) and a reduction of the intensity of $O - 2p$ and $Ti - 3d$ states in TiO_2 when defects are introduced unlike in the pure TiO_2.This is an indication of electronic non-locality, owing to the reduction of the crystal symmetry

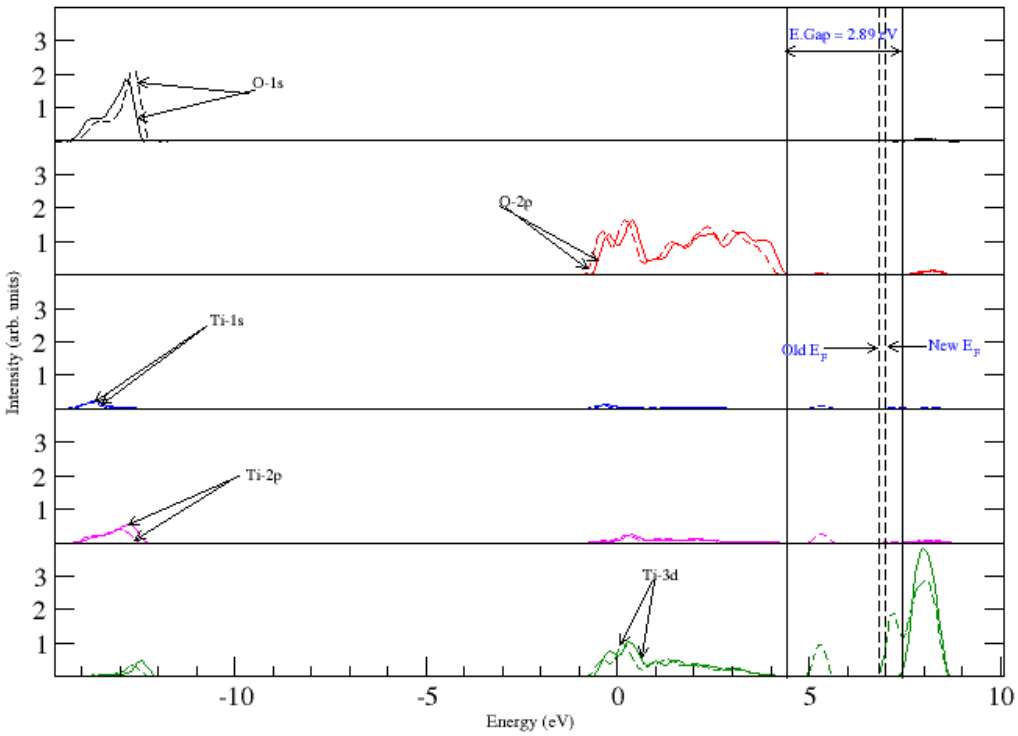

Figure 5.7: PDOS Structure of pristine rutile (solid) TiO_2, compared with those occurring in Oxygen Vacancy (dashed) calculated using DFT+U.

(Shao, 2008). A shoulder within the band gap due to $Ti - 3d$ states is also observed. Additionally, the observed defect levels within the band gap are also due to a small contribution by $Ti-1s$ and $Ti-2p$. It is also worthy noting that the widths of the upper part of the VB are similar for both pristine and defective super-cells which indicates that rutile does not experience significant chemical broadening that could offset the VB edge position (Adepalli, $et.al$, 2013). Removal of one neutral oxygen atom has been reported to result into two excess electrons located at the vacancy (Hossain, $et.al$, 2007). These excess electrons previously occupied $O - 2p$ states in the VB and since they are no longer available, these electrons go to the CB, the bottom of which is formed by $Ti-3d$ states (Diebold, 2003). The two electrons occupy the $Ti - 3d$ states where, both the neighbouring five-fold and six-fold Ti-atoms receives an electron each. Thus, the DOS peak for $Ti - 3d$ is observed below the Fermi level (Lee, $et.al$, 2012). These two extra electrons are unpaired. In the oxygen vacancy, these electrons acts as donor-like states that creates an accumulation layer in the region causing the downward band bending

(Diebold, 2003). As noted earlier, excess electrons in these material will be de-localized on the $d-states$ of cations $Ti-3d$, whereas electron holes are centred on the *2p* states of the anion ($O-2p$) which is consistent with electron spin resonance (ESR) data. Thus, as observed by Glassford & Chelikowsky (1992) the presence of oxygen vacancy creates defect levels within the gap, thereby, improving electron transition from the VB through the defect states to the CB hence allowing the absorption in the long wavelengths (0.1 - 0.3 eV) especially for shallow defect levels.

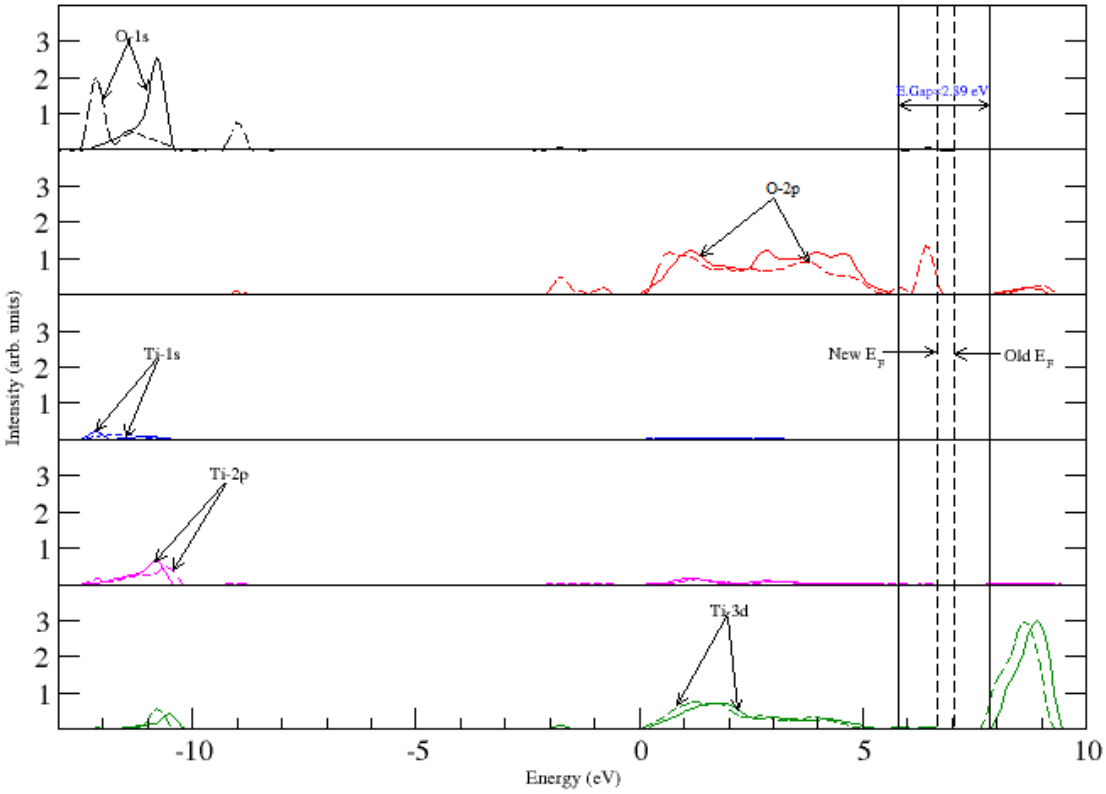

Figure 5.8: PDOS Structure of pristine rutile (solid) TiO_2, compared with those occurring in Oxygen Interstitial (dashed) calculated using DFT+U.

A similar trend of formation of defect levels states within the band gap was observed in the presence of oxygen interstitial (see **Figure 5.8**). However, in this case, four new defect levels, some shallow while others deep within the band-gap were observed. The highest new defect states were observed at $\sim 0.64\ eV$ above the VBM. The states responsible for the formation of these levels are $O-2p$ and $Ti-3d$. The appearance of the position of the Fermi level closer to the VB tend to suggest that oxygen interstitial in

rutile results in an acceptor-type conductivity. However, due to the very nature of O_I not accepting or donating charge carriers, it has minimal effect on the electronic properties of TiO_2 (Morgan, & Watson, 2009).

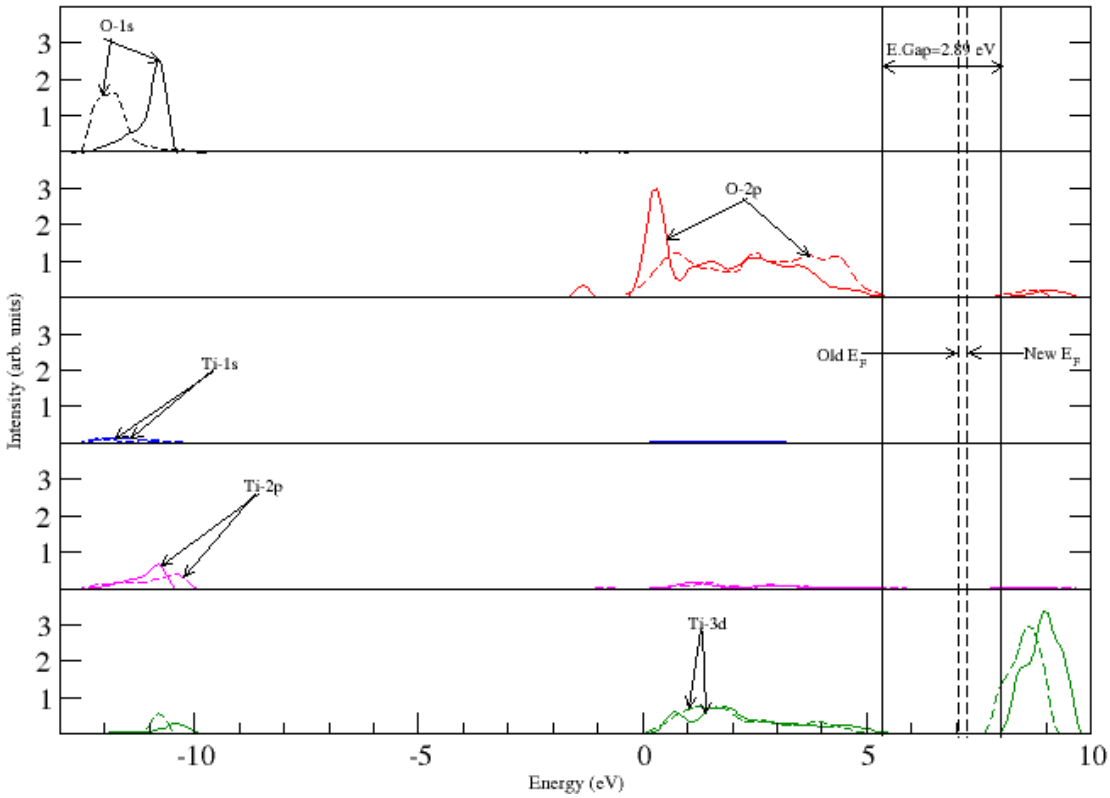

Figure 5.9: PDOS Structure of pristine rutile (solid) TiO_2, compared with those occurring in Titanium Interstitial (dashed) calculated using DFT+U.

Figure 5.9 shows the PDOS of pristine rutile TiO_2 compared to those occurring in the presence of titanium interstitial (Ti_I). In this study, titanium interstitial caused an upward shifting of the E_F towards the CB edge and generation of four $Ti - 3d$-like defect levels within the band gap located at 0.83 eV and 1.17 eV above the VB edge as well as 0.93 eV and 0.56 eV below the CB edge. The unpaired electrons of this level lie on the interstitial and the adjacent $Ti - 3d$ (Santara, $et.al$, 2013). Among the shallow localized levels, the highest on is located at 0.56 eV below the CBM , which agrees well with a value of 0.5-1.0 eV reported by other studies (Lee, $et.al$, 2012). The extra peak at $0.93\ eV$ below the CB edge arises from the octahedral distortion around the interstitial Ti atom. As was the case for the oxygen vacancy and interstitial, the states

responsible for the formation of these defect levels are the $O-2p$ and $Ti-3d$ states. The PDOS shape shows the VB of titanium dioxide with defects being slightly broader VB width than the pure TiO_2 as was the case of oxygen vacancy suggesting electronic non-locality, owing to the reduction of the crystal symmetry (Shao, 2008). The upward shifting of the E_F towards the CB and the formation of the defect levels is an indication of n-type conductivity due to the presence of the Ti_I.

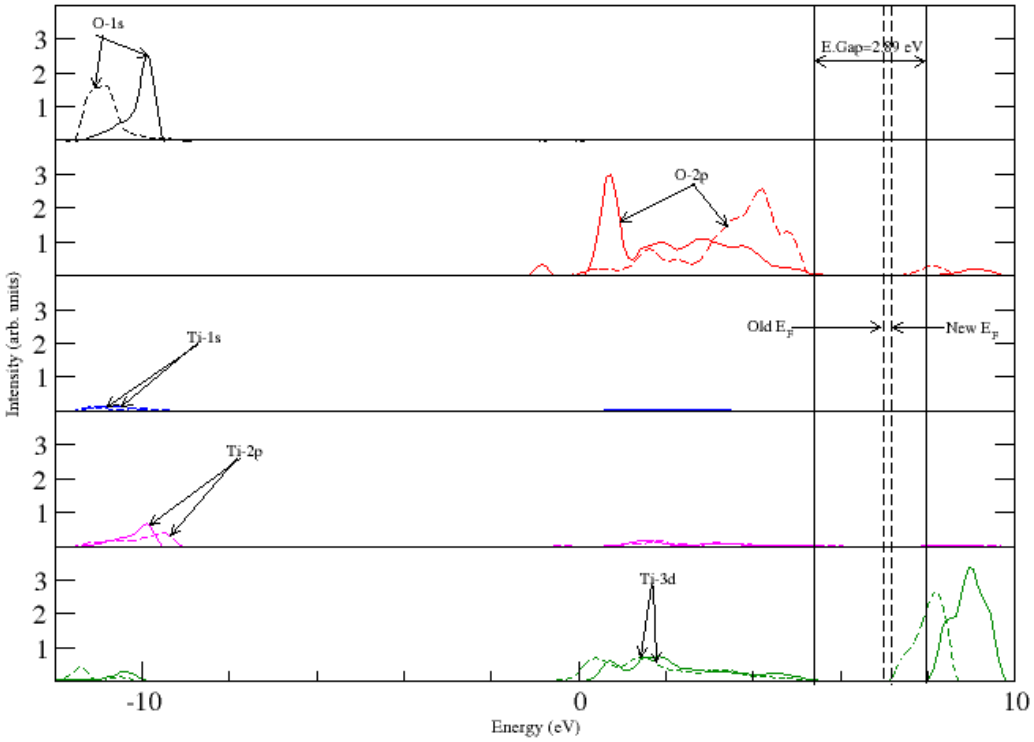

Figure 5.10: PDOS Structure of pristine rutile (solid) TiO_2, compared with those occurring in Ti_v (dashed) calculated using DFT+U.

Just like the case of O_I, the presence of titanium vacancy (Ti_V) resulted in the downward shifting of the Fermi level towards the VB edge, an indication of acceptor-like conductivity. Introduction of Ti_V led to the formation of $O-2p$-like defect levels, the highest of which was observed lying 0.62 eV above the VBM (see **Figure 5.10**). Here, titanium vacancy captures an electron from its surrounding oxygen atom and makes acceptor-like defect state in the lower half of the band gap (Morgan, & Watson, 2009). The formation of the defect levels within the band gap and the downward shifting of the E_F is an indication of $acceptor$-behavior hence, p-type conductivity for rutile TiO_2 in the the presence of Ti_V.

Figure 5.11 and 5.12 show the rutile super-cells with O_F and Ti_F defects. As depicted by these figures, the presence of Frenkel defects usually leads to the displacement of an atom from its lattice site, thereby leaving behind a vacancy and creating an interstitial at the region it settles.

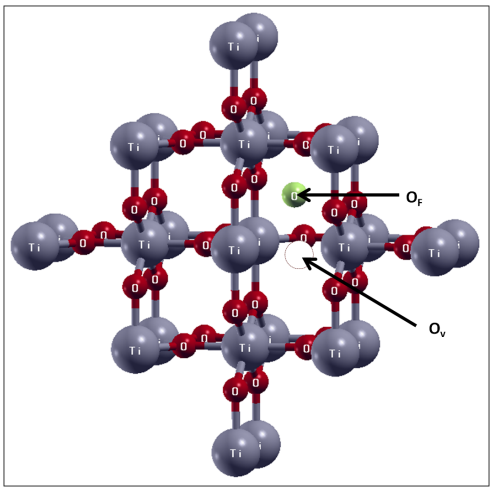

Figure 5.11: Rutile TiO_2 super-cell with O_F.

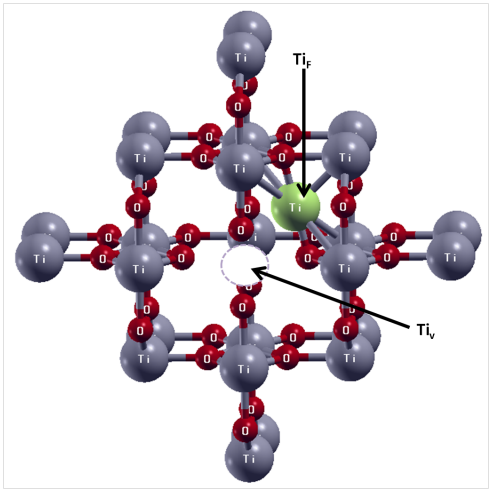

Figure 5.12: Rutile TiO_2 super-cell with Ti_F.

Figure 5.13 shows PDOS of pristine rutile and those occurring in the presence of oxygen Frenkel. A closer look at the PDOS shows that O_F led to the formation of defects levels whose locations were varying; some being shallow while others located deeper inside the band gap relative the band edges. The shallow defect levels were observed at 0.203 eV below the CB edge (see figure A.10 on the appendices section). The Fermi level (E_F) shifted upwards by $0.45\ eV$ towards the CB edge when compared to that of the pristine structure. The states responsible for the formation of O_F defect levels are $O - 2p$ and $Ti - 3d$ states.

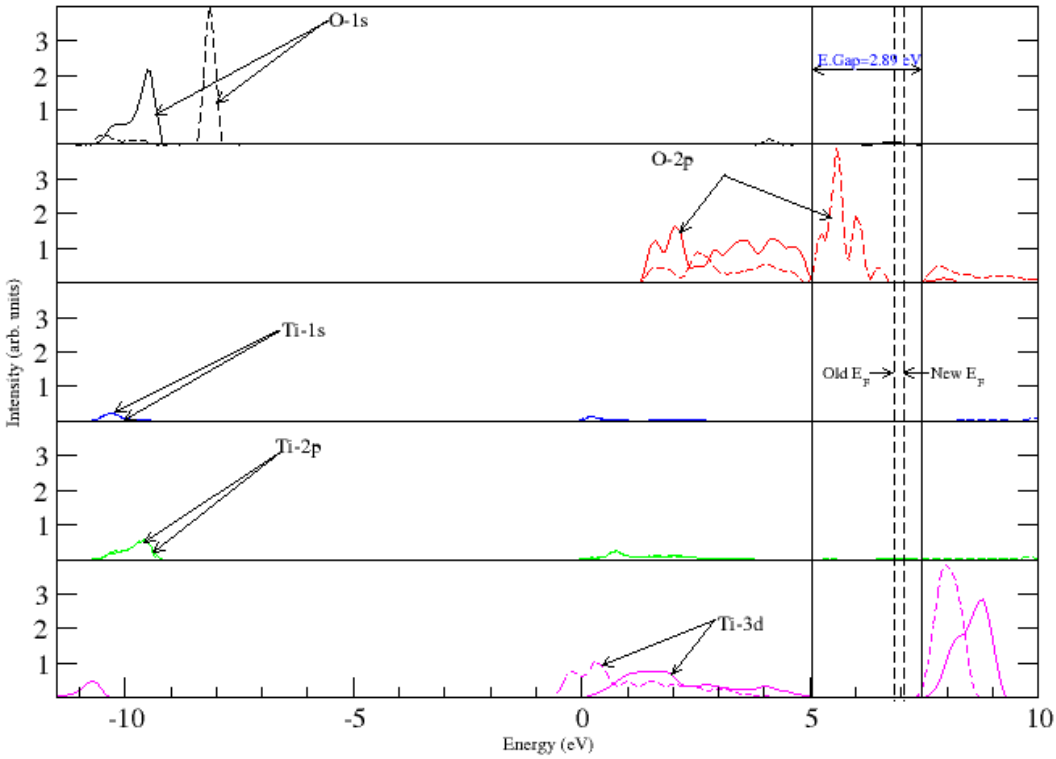

Figure 5.13: PDOS for pristine rutile (solid) TiO_2 compared with those occuring in a structure with O_F (dashed) calculated using DFT+U.

Titanium Frenkel defect led to the formation of defect levels within the band gap with the lowest being located 0.801 eV below the VB edge. The E_F shifted downwards by $0.401\ eV$ towards the VB edge (see **Figure 5.14**). With such a shallow level, Frenkel defects introduced almost "metal-like" characteristics in TiO_2. Just as was the case for oxygen Frenkel defects, the states responsible for the formation of Ti_F defect levels were $O-2p$ and $Ti-3d$ states. Oxygen Frenkel defects induced donor-like behaviour because the induced defect level states formed on the upper part of the band gap energy close to the CB edge with the E_F too shifting towards the CB edge. Titanium Frenkel defects induced acceptor-like characteristics because the defect level states were formed on the lower part of the band gap close to the VB edge accompanied by a downward shifting of the E_F towards the VB edge.

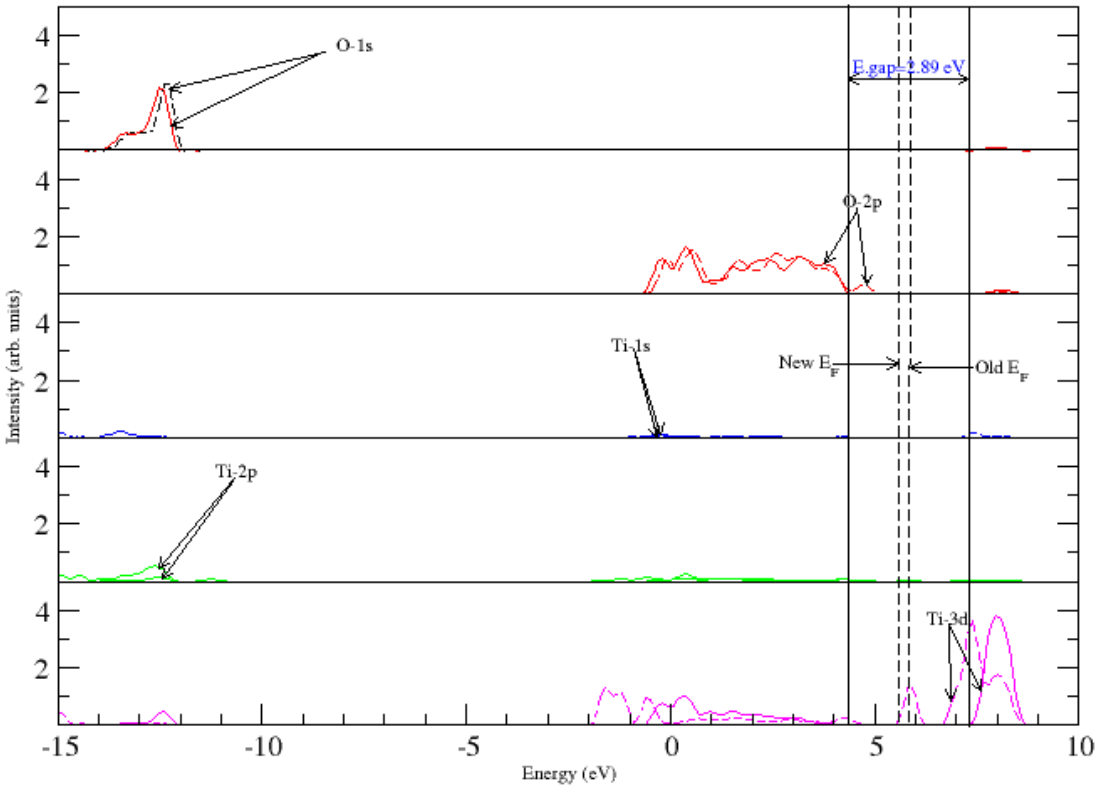

Figure 5.14: PDOS for pristine rutile (solid) TiO_2 compared with those occurring in a structure with Ti_F (dashed) calculated using DFT+U.

Both the oxygen and titanium Frenkel defects led to “metal-like” behaviour in rutile TiO_2 due to the observed shallow defect states.

5.4.2 Electronic Band Structure of Anatase TiO_2 Crystals With Defects

The presence of defects in anatase as was the case of rutile has profound effects on its electronic band structure characteristics. Figure 5.15 shows the PDOS of anatase TiO_2 with oxygen vacancy defects. A closer look at the PDOS shows that oxygen vacancy within the anatase super-cell resulted to an upward shifting of the Fermi level by 0.18 eV from 5.43 eV, to 5.61 eV towards the CB edge. A modification of the band gap similarly occurred by the formation of two defect levels which are observed within the band gap located at 0.735 eV just below the conduction band edge. These defect levels are attributed to both $O - 2p$ and $Ti - 3d$ states located at 0.17 eV and 0.21 eV, respectively, above the new E_F. These defect level states, are attributed to electrons localized on Ti^{3+} centers (Morgan & Watson, 2009). As reported by Na-Phattalung, $et.al$, oxygen vacancy defect formation in anatase results in the formation of two excess electrons neighbouring the vacancy where, these excess electrons occupy two $Ti - 3d$ orbitals, with one on the Ti sites neighboring the vacancy, and the second at a next-nearest Ti position (Na-Phattalung, $et.al$, 2006). Accompanied by this de-localization is the movement of one oxygen towards the vacancy site to give rise to a 'split vacancy'. The findings of this study were in agreement with those of other workers reported here and it was also found that the presence of O_V was further found to result to the downward bending of the CB.

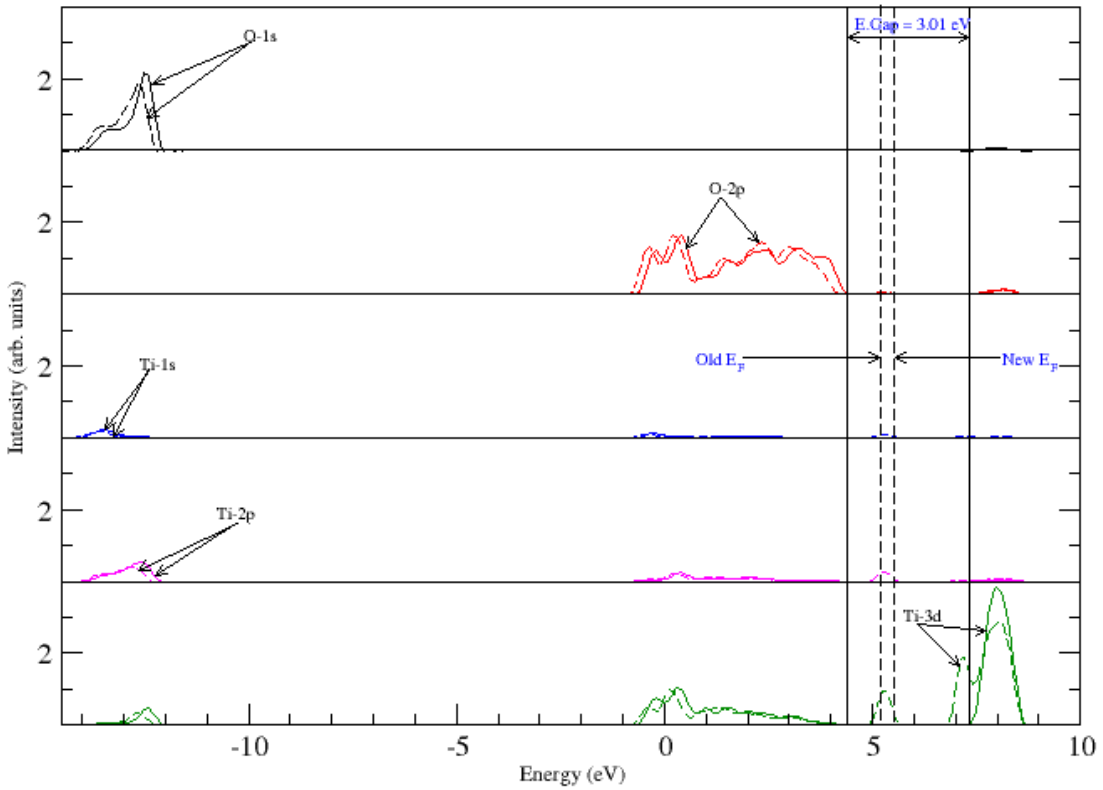

Figure 5.15: PDOS Structure of pristine anatase (solid) TiO_2, compared with those occurring in a structure with O_V (dashed) calculated using DFT+U.

The PDOS upon introduction of an oxygen interstitial (O_I) as presented in **Figure 5.16** shows that these defects leads to a downward shifting of the Fermi level (E_F) by 0.16 eV which is lower than that resulting from oxygen vacancy. Defect level states were also observed within the energy band gap, with the highest one being located at 0.65 eV above the VBM. The states responsible for the formation of these defect levels are $O-2p$ and $Ti-3d$ states located at 0.19 eV above the VBM & 1.54 eV below the CBM and 0.191 eV above the VBM & 1.37 eV below the CBM, respectively. However, just as was the case in the rutile TiO_2 structures whereby the O_I does not accept or donate charge carriers, it has minimal effect on the electronic properties of anatase TiO_2 (Morgan & Watson, 2009).

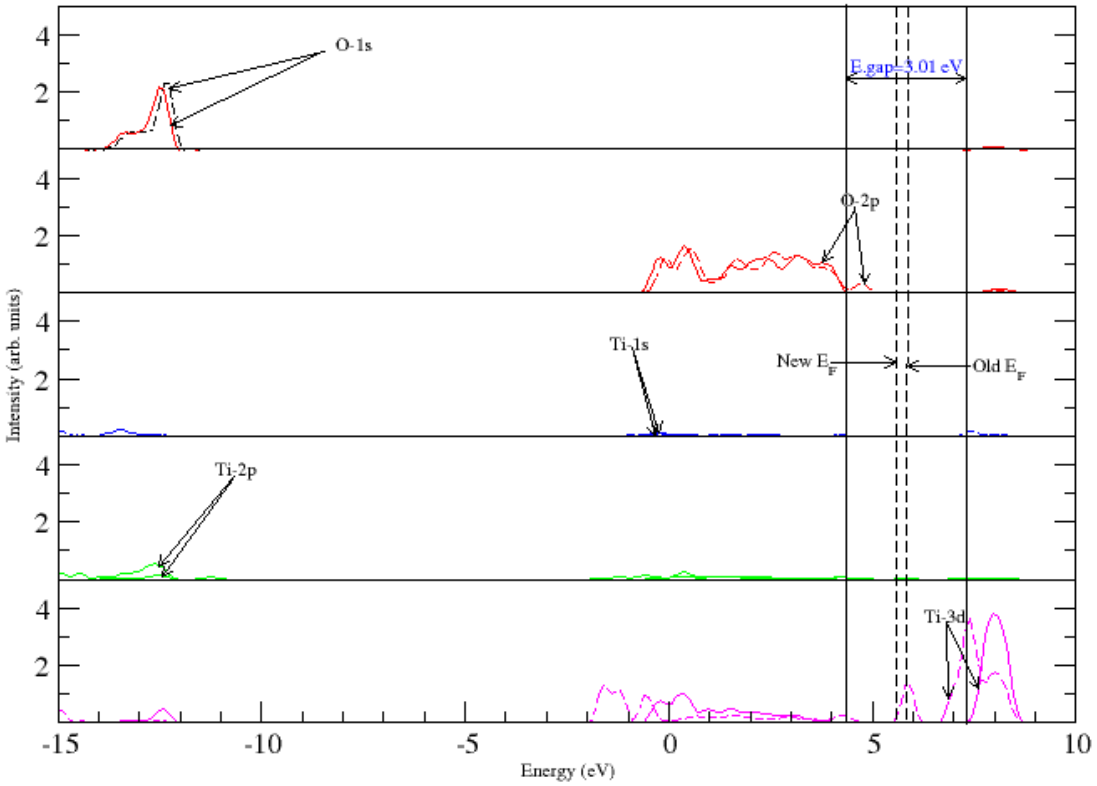

Figure 5.16: PDOS Structure of pristine anatase (solid) TiO_2, compared with those occurring in a structure upon introduction of O_I (dashed) calculated using DFT+U.

The PDOS spectra following the introduction of a titanium interstitial (Ti_I) as shown in **Figure 5.17** led to the creation of deep donor levels lying 1.22 eV ($\lambda = 1017.42$ nm) below the CBM which compares relatively well with values 1.27 eV and 1.47 eV reported by Santara $et.al$ (2013) and also shallow donor levels at 0.314 eV just below the CBM within the energy gap. These defect levels are easily excited, thereby leading to better conductivity of the materials. The Fermi level shifted upwards towards the CBM by 0.423 eV. The upward shifting of the E_F coupled with the creation of the defect levels results to n-type conductivity in anatase. This can effectively reduce the energy for the electron transition from the VBM to the CBM. A similarity is drawn with rutile, in the sense that the states responsible for the formation of these donor levels resulting from titanium interstitial are $O - 2p$ and $Ti - 3d$ states. A Ti_I, donates four electrons to the Ti lattice. One of these electrons is located at the interstitial Ti site, and three occupied defect states are hybridized between three nearest neighbour Ti sites compared

to rutile, where these excess electrons are mostly localized at four nearest neighbour Ti sites, with only a small amount of excess charge being found on the interstitial Ti atom (Morgan, & Watson, 2009). This difference in the charge on the interstitial atom is a consequence of the differing interstitial geometries in the two polymorphs.

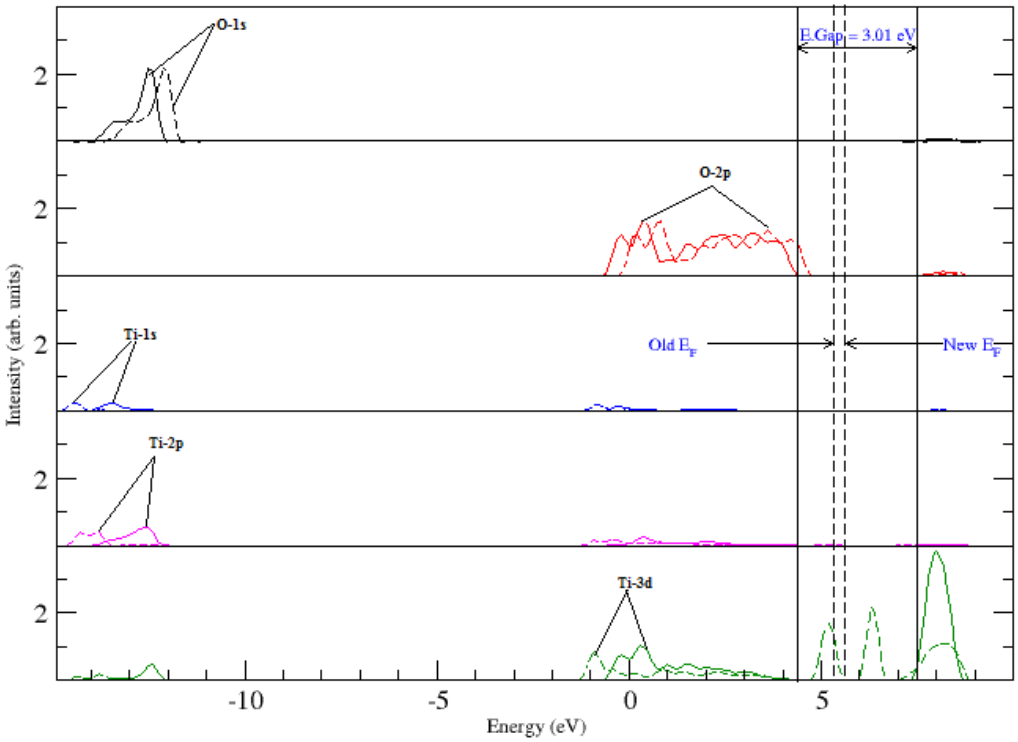

Figure 5.17: PDOS Structure of pristine anatase (solid) TiO_2, compared with those occurring in Ti_I (dashed) calculated using DFT+U.

Removal of a Ti atom resulted in the formation of titanium vacancy which in turn led to the formation of some defect levels within the energy gap as illustrated in **Figure 5.18**. These were located at 0.81 eV above the VB edges and the Fermi level was found to shift downwards by 0.63 eV towards the VBM, which was a clear indication of $acceptor$-like behaviour of titanium vacancy in anatase TiO_2. The states responsible for the formation of these $acceptor$ levels are $O-2p$ located 0.17 eV above the VBM and $Ti-3d$ states located 0.79 eV above the VBM. The presence of titanium vacancy (Ti_V) similarly resulted into the downward bending of the CB (see figure B.11 on the appendices section) as was the case of the oxygen vacancy, a trend that is also observed for the oxygen interstitial. Thus, from this study, it is quite clear that titanium Schottky

defects lead to a modification of the electronic structure of anatase so as to improve its conductivity. Since the band-gap of a material determines the overall behaviour e.g elctronic and optical and performance of devices, it is expected that the modification brought about by the defects will indeed improve on this performance.

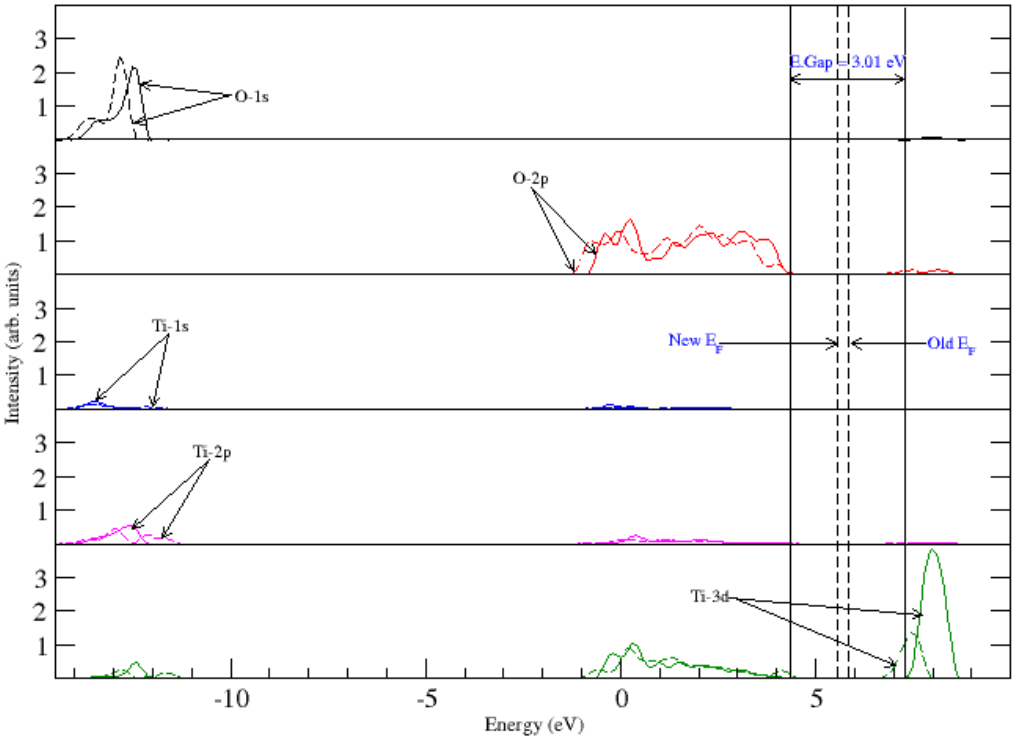

Figure 5.18: PDOS Structure of pristine anatase (solid) TiO_2, compared with those occurring in a structure with Ti_V (dashed) calculated using DFT+U.

The presence of both oxygen Frenkel (**Figure 5.19**) and titanium Frenkel defects (**Figure 5.20**) resulted into the displacement of an atom from its lattice point leaving behind a vacancy and creating an interstitial at the region where it settles.

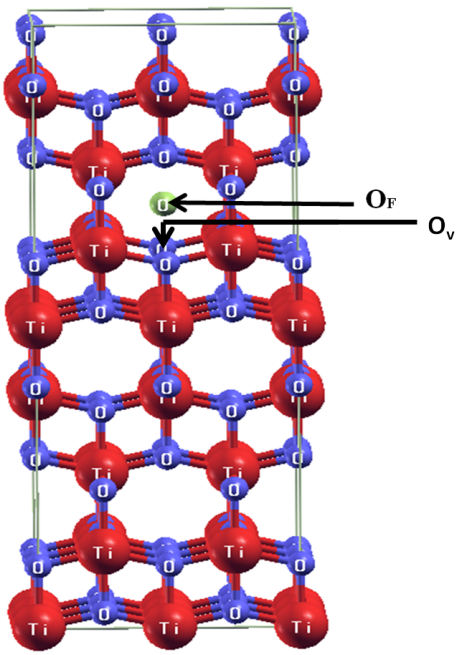

Figure 5.19: An optimized anatase super-cell with O_F.

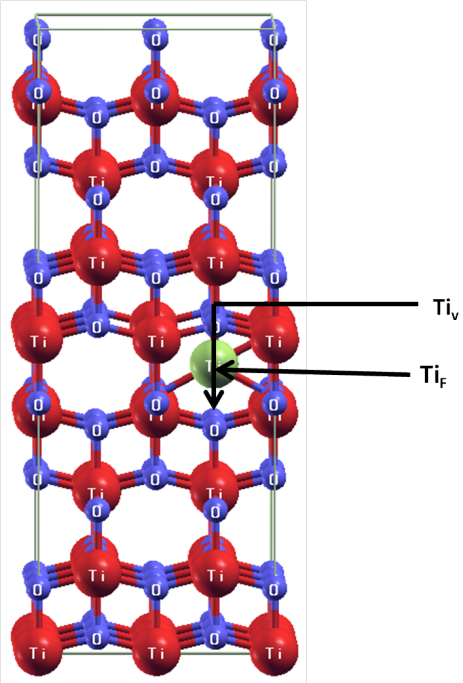

Figure 5.20: An optimized anatase super-cell with Ti_F.

Figure 5.21 shows the PDOS for pristine anatase TiO_2 and those occurring as a result of an oxygen Frenkel (O_F) defect. From the band structure, O_F resulted in the formation of defect levels within the energy gap located 0.297 eV just below the CBM. The defect states had feature-like three shoulders located within the band gap which were due to O-2p orbitals. The presence of oxygen Frenkel defect also led to the upward shifting of the E_F toward the CBM by 0.247 eV compared with the pristine structure. Thus, oxygen Frenkel defect introduced donor-like behaviour in anatase. The defect levels within the band-gap arising from the presence of oxygen Frenkel resulted from $O-2p$ and $Ti-3d$ states. However, a slight difference is visible between Frenkel and Schottky defects in that unlike Schottky defects where the contribution of $Ti-3d$ states was dominant, here, the contribution of $O-2p$ states is significant with only a small contribution from the $Ti-3d$ states.

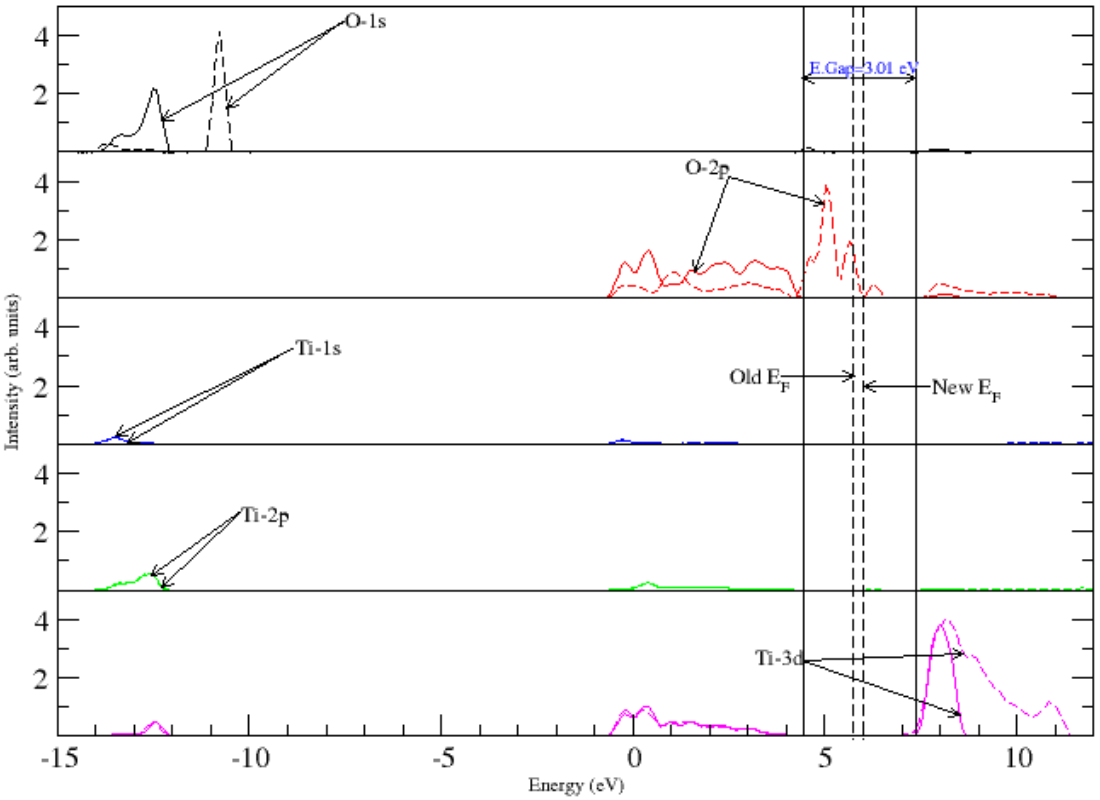

Figure 5.21: PDOS of pristine anatase (solid) TiO_2, compared with those occurring in O_F (dashed) calculated using DFT+U.

The presence of titanium Frenkel defect led to the formation of defect levels (see **Figure 5.22**) located at 0.718 eV above the VBM. The defects due to $Ti-3d$ states caused a shoulder-like feature that is located within the CB. Additionally, titanium Frenkel defect led to the downward shifting of the E_F towards the VBM by 0.055 eV. Thus, the presence of titanium Frenkel defect introduced acceptor-like behaviour in anatase. Just as was the case of oxygen Frenkel defect, the presence of titanium Frenkel defect resulted into defect states within the band-gap from $O-2p$ and $Ti-3d$ states, although the $Ti-3d$ states were the most dominant. An important observable feature of the band structure is the downward bending of the CBM due to Frenkel defects (see figure **B.10**).

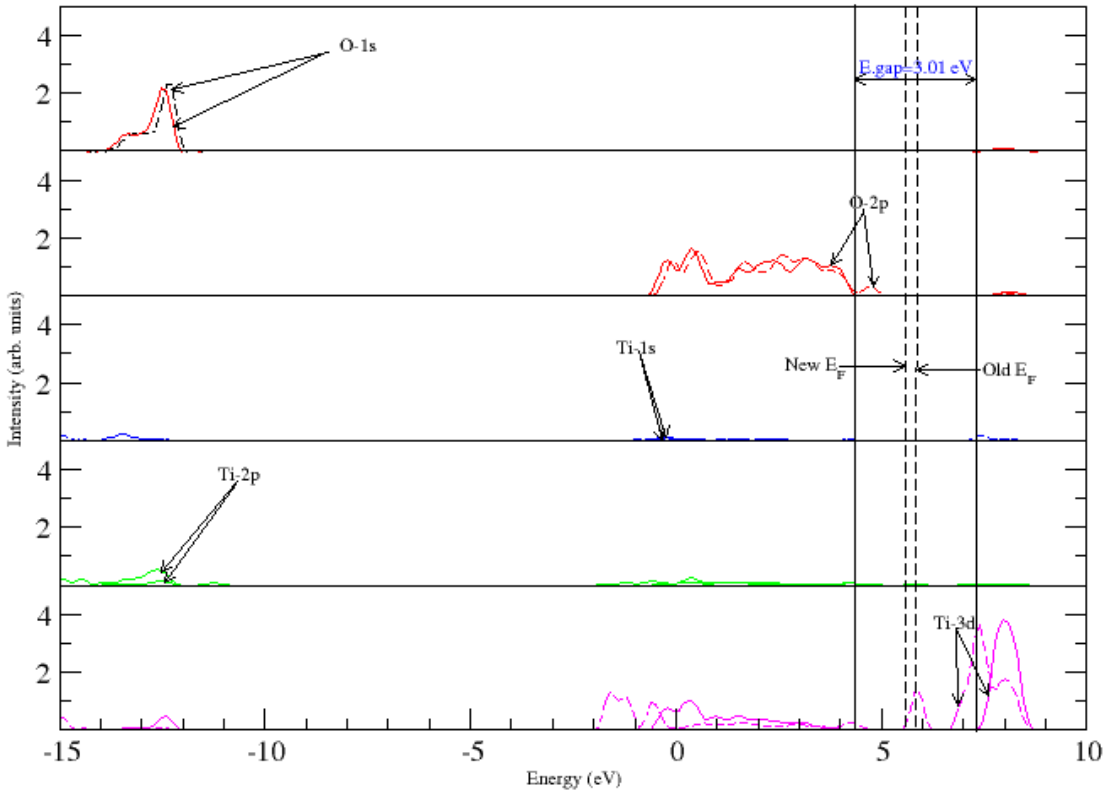

Figure 5.22: PDOS of pristine anatase (solid) TiO_2, compared with those occurring in a structure with Ti_F (dashed) calculated using DFT+U.

The findings of this study show that, both Schottky and Frenkel intrinsic point defects give rise to new defect states within the energy band-gap. The origin of these localized states are the $O - 2p$ and $Ti - 3d$ states. These defect level states within the band gaps of the two phases of TiO_2 are the ones largely responsible for the observed enhanced electrical conductivity and light absorption over a wider range of the light spectrum in their non-stoichiometric form as compared to the stoichiometric TiO_2 form.

5.5 DOS Differences

The density of states differences between the DOS of pristine and those of defective super-cells were also studied. These differences are able to bring out clearly any variations that occur between the density of states for the pure and defective TiO_2 structures. If there is no difference, then the variations could be zero, but where variations occur they will manifest themselves as either positive or negative deviations. There was a general trend in the observed shape of the plots that the DOS for all the studied TiO_2 structures were not the same as those of the pure structures as seen in **Figure 5.23 and 5.24**, for the pristine TiO_2 and those of anatase TiO_2 structures with oxygen vacancy and titanium interstitial. This study is compared with no other work since such work is unavailable.

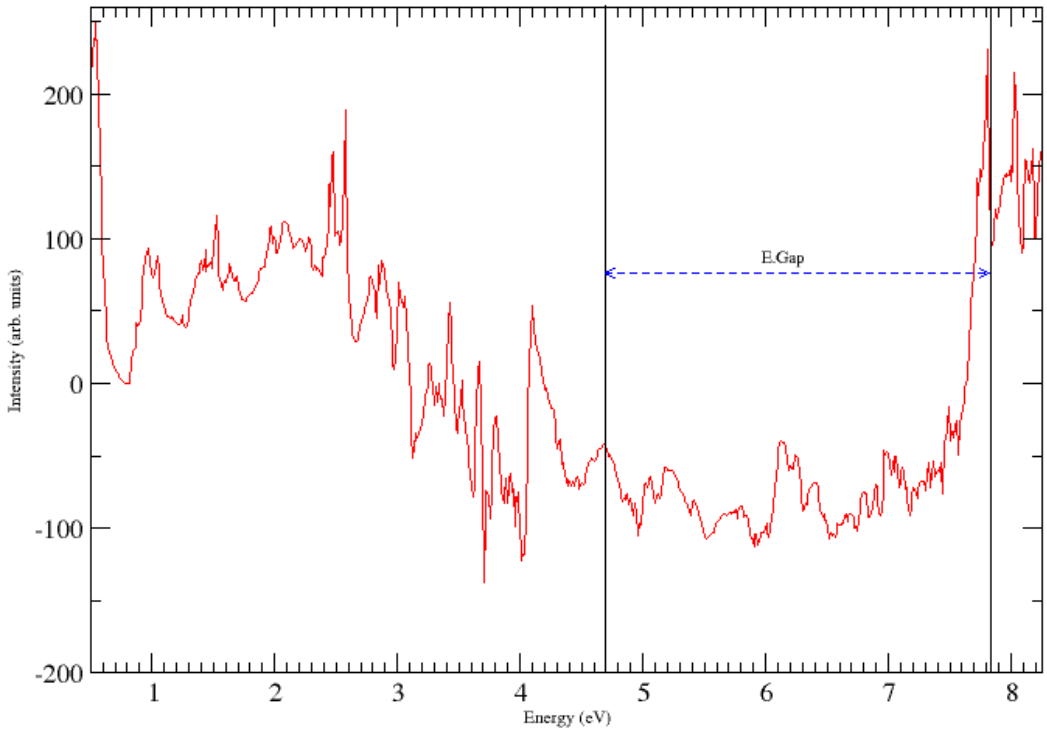

Figure 5.23: Diagrammatic representation of the DOS difference between those of pristine and those occuring in anatase TiO_2 with O_V.

Since, the Fermi level for the pristine anatase was at 5.42 eV, the observed peaks within the band gap compares well with the observed positions of the defect states due to O_V (see **Figure 5.23**). This trend is replicated in TiO_2 structure with Ti_I, where

the observed peaks tend to correspond to the observed defect level positions as well as in other structures as shown in the appendix (see Appendix Three). Thus, the DOS deviations can indeed be used to locate the exact positions of the defect states. Similarly, the observed peaks within the band gap are negative (below the zero $x - axis$). Such peaks are be attributed to charge carriers brought about by the presence of these native defects within the pristine cells of TiO_2.

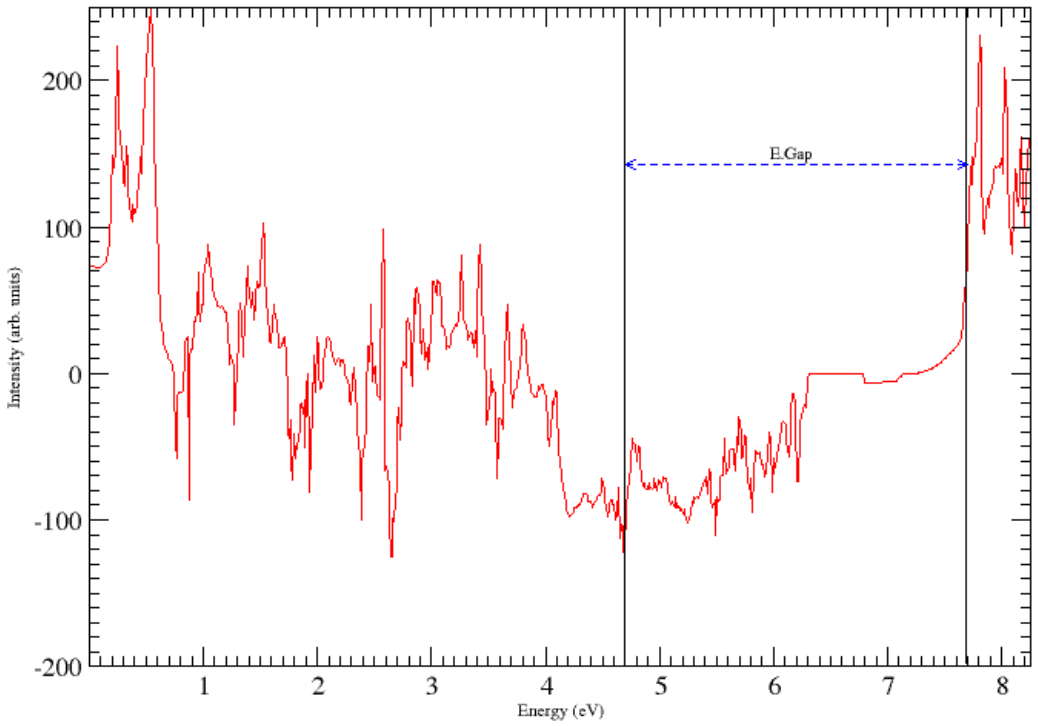

Figure 5.24: Diagrammatic representation of the DOS difference between those of pristine and those occuring in anatase TiO_2 with Ti_I.

5.6 Defect Formation Energies (DFE)

Formation energies are important criteria of evaluating the relative difficulty for the incooperation of dopants/defects into the host lattice and therefore the relative stability of the doped/defective systems. In this study, only charge neutral structures have been considered and thus, the formulation of the formation energies does not include the chemical potential of electrons.

5.6.1 Defect Formation Energies in Rutile

In the calculation of the Defect Formation Energies (DFEs), an approach involving the use of equations (5.1) - (5.4) was applied. Here, the total energy of the perfect crystal (E_c) was first calculated before introducing the defects and then the crystal was relaxed and its total energy obtained. From this process, the DFEs per formula unit for the vacancy (DFE_V) and interstitial (DFE_I) is given by the equations (5.1) and (5.2), respectively;

$$DFE_v = E_v – E_c + E_a, \tag{5.1}$$

and

$$DFE_i = E_i – E_c - E_a, \tag{5.2}$$

where, E_a is the energy of a single free atom in the vacuum in the case of a cation and energy of a free oxygen atom in the case of an anion. E_v is the relaxed energy of the crystal containing a vacancy and E_i is the relaxed energy of the crystal containing an interstitial.

DFEs for the Frenkel pair, were calculated using the relation given by equation (5.3). In this case, the separation between the Frenkel defects is assumed to be infinite such that there is no interaction between them.

$$DFE_i = E_i + E_v - 2E_c. \tag{5.3}$$

In order to compare the results of this work and other studies, the Frenkel pair formation energies were determined by creating an interstitial and vacancy in the same super-cell. The defect formation energy was calculated using the relation,

$$DFE_i = E_{disp} - E_c, \tag{5.4}$$

where, E_{disp} is the total energy for the super-cell with cation or anion Frenkel and E_c is the total energy of a perfect crystal. The result of the calculated formation energies are summarized in Table 5.4.

Table 5.4: Calculated GGA+U Defect Formation Energies in Rutile TiO_2.

$Defect$	$DFE/formula\ unit\ (eV)$	$Expt\ Value\ (eV)$
$Oxygen\ Vacancy$	8.19	7.5^*
$Oxygen\ Interstitial$	-7.36	–
$Titanium\ Vacancy$	1.14	–
$Titanium\ Interstitial$	-0.17	–
$Oxygen\ Frenkel$	0.19	–
$Titanium\ Frenkel$	0.26	–

[*Hallil, $et.al$, 2006]

It is only in oxygen vacancy where an experimental value exist and a deviation of 9.2% was obtained. This suggests that the calculation tends to overbind the defect state. Clearly, from the data, all interstitials have negative formation energies, thus more favorable to form than vacancies which have positive values. The easiest defect to form is the oxygen interstitial and the most difficult to form is the oxygen vacancy. These findings are consistent with the expectations that, it is easier to displace an atom within a crystal lattice than to completely remove it altogether.

5.6.2 Defect Formation Energies in Anatase

A similar approach was used to determine defect formation energies in anatase as was for the case in rutile TiO_2. The resulting values are summarized in Table 5.5.

Table 5.5: Calculated GGA+U Defect Formation Energies in Anatase TiO_2.

$Defect$	$DFE/formula\ unit\ (eV)$	$Expt\ Value\ (eV)$
$Oxygen\ Vacancy$	9.33	–
$Oxygen\ Interstitial$	−8.76	–
$Titanium\ Vacancy$	1.39	–
$Titanium\ Interstitial$	−0.22	–
$Oxygen\ Frenkel$	0.33	–
$Titanium\ Frenkel$	0.29	–

From the data presented in **Table 5.5**, the DFEs of anatase follows a similar trend as in rutile. In particular interstitials have negative formation energies, while vacancies have positive formation energies. Therefore, interstitials with negative energies are more favorable to be formed than vacancies which have positive values. Thus, the easiest defects to form are the interstitials especially oxygen interstitial while the most difficult defects to form are the vacancies especially oxygen vacancy. The small size of oxygen atom may be responsible for the ease of formation of this defects unlike the large and heavy titanium atom. From the comparison of DFEs for the Schottky and Frenkel defects, it is also clear that it is easier to displace an atom within a lattice than to completely remove it from the material. However, it is also relatively easier to introduce an atom into an interstitial site than displace the already existing atoms within the material. A comparison of results shown in **Tables 5.4** and **5.5** shows that it is easier to form O_V, O_F, Ti_V and Ti_F in rutile than in anatase TiO_2 while it is easier to form O_I and Ti_I in the later than in the former.

A comparison of the DFEs obtained using different pseudo-potentials i.e NC-PPs and US-PPs calculations is summarized in Tables D_1 and D_2 on the appendix four where a trend similar to the one reported here is observed.

CHAPTER SIX

CONCLUTIONS AND RECOMMENTATIONS

6.1 Conclusions

This study used an on-site Coulomb correction U term to investigate the effect of intrinsic point defects on the electronic properties of anatase phases of TiO_2 which forms the scope of this work. Findings on rutile phase of TiO_2 are also presented. The results obtained predict a direct band gap of 2.89 eV along Γ high symmetry point for pristine rutile and an indirect band-gap of 3.01 eV along the path $\Gamma \rightarrow Z$ for the pristine anatase TiO_2, which is an improvement when compared to the DFT values and much closer to the experimental values (deviations of -3.667% and -6.81% respectively). Additionally, a direct band gap of a value 3.11 eV along Γ is observed for the pristine anatase.

The presence of intrinsic point defects within the super-cells of the two phases of TiO_2 led to local structural disorders that modified the bonding environment around the defect site. The level of these distortions depended on the nature of the defect. The presence of Ti_F in rutile resulted in a +12.3 % elongation in the equatorial Ti-O bond length, which is the largest change in the rutile phase, while O_F defect caused a contraction of -11.2 % in the same phase. The two defects caused corresponding changes in the Ti-O-Ti bond angle varying between 143.49^o - 131.41^o and 99.93^o - 88.86^o for Ti_F and O_F defects, respectively. In anatase, the presence of Ti_F resulted in a +8.9 % elongation in the equatorial Ti-O bond length, while O_F defect caused a contraction of -8.0 % in the same phase. Accompanied by these bond length changes are the changes in the Ti-O-Ti angles which ranged from 152.39^o - 176.05^o and 103.81^o - 93.59^o for Ti_F and O_F, respectively. The Schottky defects within the two phases caused structural defects as summarized in **Table 5.3** which are in the range of those observed in the case of Ti_F and O_F.

Intrinsic point defects caused structural deformations in both rutile and anatase TiO_2 phases. These structural disorders were accompanied by electronic band structure mod-

ifications. Both Schottky and Frenkel defects led to the formation of defect states within the energy band gap. Introduction of O_V and O_I in rutile resulted to defect states located 0.75 eV below the CB edge and 0.64 eV above the VB edge, respectively. The presence of Ti_V in rutile led to formation of defect states located 0.62 eV above the VB edge while Ti_I led to four defect states located 0.83 eV & 1.17 eV above the VB edge and 0.93 eV & 0.56 eV below the CB edge. The presence of O_F in rutile TiO_2 caused defect states located 0.203 eV below the CB minimum while Ti_F caused defect states located 0.801 eV above the VB maximum.

The presence in anatase of O_V and O_I resulted to defect level states located 0.735 eV below the CB minimum and 0.646 eV above the VB maximum, respectively. Similarly, Ti_V and Ti_I led to the formation of defect states located 0.805 eV above the VB edge and 1.22 eV below the CB edge. On the other hand, O_F caused defect states located 0.297 eV below the CB minimum while Ti_F caused defect states located 0.718 eV above the the VB maximum.

In all the defects investigated in this study, the origin of the observed localized defect states in both phases of TiO_2 are the $O-2p$ and $Ti-3d$ orbitals, with $Ti-3d$ orbitals dominating in a majority of the considered defects. This effectively answers the question of the origin of the localized defect level states observed in TiO_2 by many studies. It is also worthy highlighting that, even though the contribution of $Ti-3d$ orbitals to formation of the defect states was dominant due to most of the native point defects, in the presence of O_F defects, $O-2p$ orbitals were observed to be dominant in contributing to the formation of these defect states. The presence of O_V, O_F and Ti_I in both rutile and anatase led to an upward shifting of the Fermi level (E_F) closer to the CB edge, thus can be interpreted to cause $n-type$ conductivity, while O_I, T_V and Ti_F led to a downward shifting of the E_F closer to the VB edge, thus causing $p-type$ conductivity. Therefore, the presence of intrinsic point defects in the two phases of TiO_2 is expected to reduce the electron transition energy from the VB to the CB, hence enhancing light absorption in the long wavelength which is accompanied by addition to improved electrical conductivity.

The calculated defect formation energies (DFEs) in both phases of TiO_2 under this study showed that the formation of interstitials is the most favoured due to their negative DFEs while vacancies are the most difficult to form due to their high positive values of DFEs. The easiest defect to form in both rutile and anatase TiO_2 is the O_I while the most difficult to form is the O_V. Furthermore, it is observed that it is easier to displace an atom within a crystal lattice than to completely remove it altogether.

Since the band-gap of a material determines the overall behaviour and performance of devices made from them, it is expected that the introduction of defects in TiO_2 will provide the desired performance efficiency of these devices. As such, this study suggests that intrinsic point defects in titanium dioxide contribute to changes in both the electronic and optical properties of this material of interest for various industrial applications including photo-catalysis and light harvesting. Similarly, a study on charged structures will be necessary since this study dealt only with charge neutral cases.

6.2 Recommendations

This work investigated only single defects where only one atom was added or removed or just displaced within the super-cell. Thus, there is need for multi-atom defects to be studied. Additionally, a multi-defect study (involving both Schottky and Frenkel defects within the same super-cell) will be necessary. The study of extended defects in both rutile and anatase TiO_2 will shed more light on the properties and performance of the two materials. Further studies based on many body perturbation theory (Green Function & the Screened Coulomb Interaction, GW, and Bathe-Salpeter Equation, BSE) will be important for the understanding the optical properties of TiO_2.

REFERENCES

Adepalli, K. K., Kelsch, M., Merkle, R., & Maier, J. (2013). Influence of line defects on the electrical properties of single crystal TiO_2. *Advanced Functional Materials*, 23(14), 1798-1806.

Anisimov V. I, Aryasetian F & Lichtenstein A. (1997) First-principle calculation of the electronic structure and spectra of stronly correlated systems; LDA+U Method: *Journal of Physics: Condensed Matter*, 9(4).

Anisimov, V. I., Zaanen, J., & Andersen, O. K. (1991). Band theory and Mott insulators: Hubbard U instead of Stoner I. *Physical Review B*, 44(3), 943.

Balabin, R. M.,(2010). Is quantum chemical treatment of biopolymers accurate? Intramolecular basis set superposition error (BSSE). *Journal of Chemical Physics*, 132, 231101-231104.

Batzill, M., Katsiev, K., Gaspar, D. J., & Diebold, U. (2002). Variations of the local electronic surface properties of TiO_2 (110) induced by intrinsic and extrinsic defects. *Physical Review B*, 66(23), 235401.

Bauer, G. E., (1983), General operator ground-state expectation value in the Hohenberg-Kohn-Sham Density-functional formalism. *Physical Review B*, 27(10), 5912.

Blöchl, P. E. (1994). Projector augmented-wave method. *Physical Review B*, 50(24), 17953.

Bryan, J. D., Santangelo, S. A., Keveren, S. C., & Gamelin, D. R. (2005). Activation of high-TC ferromagnetism in Co^{2+}: TiO_2 and Cr^{3+}: TiO_2 nano-rods and nano-crystals by grain boundary defects. *Journal of the American Chemical Society*, 127(44), 15568-15574.

Brust, D. (1986). The pseudopotential method and the single-particle electronic excitation spectra of crystals. In "Methods in Computational Physics". *Academic Press New York*, vol 8, p. 33.

Burke, K. (2012). Perspective on density functional theory. *The Journal of chemical physics*, 136(15), 150901.

Campbell, S. A., Kim, H. S., Gilmer, D. C., He, B., Ma, T., & Gladfelter, W. L. (1999). Titanium dioxide (TiO_2-based gate insulators). *IBM journal of research and development*, 43(3), 383-392.

Cancarevic, M., Zinkevich, M., & Aldinger, F. (2007). Thermodynamic description of the Ti–O system using the associate model for the liquid phase. *Calphad*, 31(3), 330-342.

Catlow, C. R. A., Mackrodt, J. R., & Stewart, R. F. (1982). Defect energies in aluminium oxide and rutile titanium oxide. *Physical Review B*, 25(2), 1006-1026.

Catlow, C. R. A., Freeman, C. M., & Royle, R. L. (1985). Recent studies using static simulation techniques. *Physica B+ C*, 131(1), 1-12.

Chiodi, M., Cheney, C. P., Vilmercati, P., Cavaliere, E., Mannella, N., Weitering, H. H., & Gavioli, L. (2011). Enhanced dopant solubility and visible-light absorption in Cr-N co-doped TiO_2 nano-clusters. *The Journal of Physical Chemistry C*, 116(1), 311-318.

Chiodo, L., García-Lastra, J. M., Iacomino, A., Ossicini, S., Zhao, J., Petek, H., & Rubio, A. (2010). Self-energy and excitonic effects in the electronic and optical properties of TiO_2 crystalline phases. *Physical Review B*, 82(4), 045207.

Cho, E., Han, S., Ahn, H. S., Lee, K. R., Kim, S. K., & Hwang, C. S. (2006). First-principles study of point defects in rutile TiO_{2-x}. *Physical Review B*, 73(19), 193202.

Davidson, E. R., & Feller, D. (1986). Basis set selection for molecular calculations. *Chemical Reviews*, 86(4), 681-696.

Dawson, I., Bristowe, P. D., White, J. A., & Payne, M. C. (1996). First Principles Computer Simulation of the Defect Chemistry of Rutile TiO_2. *In MRS Proceedings* vol. 453, p. 203. Cambridge University Press.

Diebold, U. (2003). The surface science of titanium dioxide. *Surface science reports*, 48(5), 53-229.

Diebold, U., Anderson, J. F., Ng, K. O., & Vanderbilt, D. (1996). Evidence for the Tunneling Site on Transition-Metal Oxides: TiO_2(110). *Physical review letters*, 77(7), 1322.

Di Valentin, C., Pacchioni, G., & Selloni, A. (2004). Origin of the different photoactivity of N-doped anatase and rutile TiO_2. *Physical Review B*, 70(8), 085116.

DolTPoMS. Direct and Indirect Band gap Semiconductors. Retrieved, 11^{th} May, 2016 from, http://www.doltpoms.ac.uk/tlplip/semiconductors/direct.phn.

Dupin, J. C., Gonbeau, D., Vinatier, P., & Levasseur, A. (2000). Systematic XPS studies of metal oxides, hydroxides and peroxides. *Physical Chemistry Chemical Physics*, 2(6), 1319-1324.

Fahmi, A., Minot, C., Silvi, B., & Causa, M. (1993). Theoretical analysis of the structures of titanium dioxide crystals. *Physical Review B*, 47(18), 11717.

Fujishima, A. (1972). Electrochemical photolysis of water at a semiconductor electrode. *nature*, 238, 37-38.

Fujishima, A., Rao, T. N., & Tryk, D. A. (2000). Titanium dioxide photocatalysis. *Journal of Photochemistry and Photobiology C: Photochemistry Reviews*, 1(1), 1-21.

Ghuman, K. K., & Singh, C. V. (2013). A DFT+ U study of (Rh, Nb)-codoped rutile TiO_2. *Journal of Physics: Condensed Matter*, 25(8), 085501.

Giannozzi, P., Baroni, S., Bonini, N., Calandra, M., Car, R., Cavazzoni, C., & Wentzcovitch, R. M. (2009). QUANTUM ESPRESSO: a modular and open-source software project for quantum simulations of materials. *Journal of Physics: Condensed Matter*, 21(39), 395502.

Glassford, K. M., & Chelikowsky, J. R. (1992). Structural and electronic properties of

titanium dioxide. *Physical Review B*, 46(3), 1284.

Guiá Yang, H. (2010). Nanosized anatase TiO_2 single crystals for enhanced photocatalytic activity. Chemical Communications, 46(5), 755-757. Retrieved, 18 May, 2016 from http://pubs.rsc.org/en/content/articlelanding/2010/cc/b919895d/unauth.

Hahlin, M., Johansson, E. M., Plogmaker, S., Odelius, M., Hagberg, D. P., Sun, L., & Rensmo, H., (2010). Electronic and molecular structures of organic dye/TiO_2 interfaces for solar cell applications: a core level photoelectron spectroscopy study. *Physical Chemistry Chemical Physics*, 12(7), 1507-1517.

Hallil, A., Tetot, R., Berthier, F., Braems, I., & Creuse, J., (2006). Use of a variable-charge inter-atomic potential for atomistic simulations of bulk, oxygen vacancies and surfaces of TiO_2. *Physical Review B*, 73(16), 165406.

Harrison, R., Moroz, I., & Tod, K. P., (2003). A numerical study of the Schrödinger-Newton equation. *Nonlinearity*, 16, 101.

He, J., & Sinnott, S. B., (2005). $Ab\ initio$ calculations of intrinsic defects in rutile TiO_2. *Journal of the American Ceramic Society*, 88(3), 737-741.

Hehre, Warren J., (2003). A Guide to Molecular Mechanics and Quantum Chemical Calculations. *Irvine, California: Wavefunction, Inc*. pp.40–47.

Henderson, M. A., (1999). A surface perspective on self-diffusion in rutile TiO_2. *Surface Science*, 419(2), 174-187.

Henrich, V. E., Dresselhaus, G., & Zeiger, H. J., (1976). Observation of Two-Dimensional Phases Associated with Defect States on the Surface of TiO_2. *Physical Review Letters*, 36(22), 1335.

Hellmann, H., (1935). A new approximation method in the problem of many electrons. *J. Chem. Phys*, 3(1), 61.

Hellmann, H., & Kassatotschkin, W., (1936). Metallic binding according to the com-

bined approximation procedure. *The Journal of Chemical Physics*, 4(5), 324-325.

Himmetoglu, B., Floris, A., Giconcoli, S., & Cococcioni, M., (2014) Hubbard-Corrected DFT Energy Functionals: The LDA+U description of correlated systems. *International Journal of Quantum Chemistry*, 114(1), 14-19.

Hossain, F. M., Murch, G. E., Sheppard, L., & Nowotny, J., (2006). The Effect of Defect Disorder on the Electronic Structure of Rutile TiO_{2-x}. *In Defect and Diffusion Forum*251,1-12.

Hossain, F. M., Murch, G. E., Sheppard, L., & Nowotny, J., (2007). $Ab\ initio$ electronic structure calculation of oxygen vacancies in rutile titanium dioxide. *Solid State Ionics*, 178(5), 319-325.

Janotti, A., Varley, J. B., Rinke, P., Umezawa, N., Kresse, G., & Van de Walle, C. G., (2010). Hybrid functional studies of the oxygen vacancy in TiO_2. *Physical Review B*, 81(8), 085212.

Jensen, F., (1999). Introduction to Computational Chemistry. *John Wiley and Sons*, pp.150–176.

Kittel C., Introduction to Solid State Physics. *John Wiley and Son, New York* Seventh ed., (2002).

Kokalj, A., (1999). XCrySDen—a new program for displaying crystalline structures and electron densities. *Journal of Molecular Graphics and Modelling*, 17(3), 176-179.

Kresse, G., & Joubert, D. (1999). From ultrasoft pseudopotentials to the projector augmented-wave method. *Physical Review B*, 59(3), 1758.

Kofstad, P. (1962). Thermogravimetric studies of the defect structure of rutile (TiO_2). *Journal of Physics and Chemistry of Solids*, 23(11), 1579-1586.

Lany, S., & Zunger, A. (2009). Polaronic hole localization and multiple hole binding of acceptors in oxide wide-gap semiconductors. *Physical Review B*, 80(8), 085202.

Lee, H. Y., Clark, S. J., & Robertson, J. (2012). Calculation of point defects in rutile TiO_2 by the screened-exchange hybrid functional. *Physical Review B*, 86(7), 075209.

Leung, T. C., Chan, C. T., & Harmon, B. N. (1991). Ground-state properties of Fe, Co, Ni, and their monoxides: Results of the generalized gradient approximation. *Physical Review B*, 44(7), 2923.

Levine, I. N. (1991). Quantum Chemistry. *Englewood Cliffs, New jersey: Prentice Hall*. pp.461–466.

Liu, S., Yu, J., & Jaroniec, M. (2010). Tunable photocatalytic selectivity of hollow TiO_2 microspheres composed of anatase polyhedra with exposed $\{001\}$ facets. *Journal of the American Chemical Society*, 132(34), 11914-11916.

Matthiesen, J. (2007). *The influence of point defects on TiO_2 (110) surface properties*. Doctoral dissertation, Ph. D. Thesis, University of Aarhus.

Mitsuhara, K., Okumura, H., Visikovskiy, A., Takizawa M., & Kido, Y., (2012). The source of the Ti-3d defects state in the band gap of rutile titania (110) surfaces. *Journal of Chemical Physics*, 136, 124707.

Monna, K., & Izumi, F., (2008). VESTA: a three-dimensional visualization system for electronic and structural analysis. *Journal of Applied Crystallography*, 41(3), 653-658.

Moran, D., Simmonett, A. C., Leach, F. E., Allen, W. D., Schleyer, P. V. R., & Schaefer, H. F. (2006). Popular theoretical methods predict benzene and arenes to be nonplanar. *Journal of the American Chemical Society*, 128(29), 9342-9343.

Morgan, B. J., & Watson, G. W. (2009). A DFT+U description of oxygen vacancies at the TiO_2 rutile (110) surface. *Surface Science*, 601(21), 5034-5041.

Morgan, B. J., & Watson, G. W. (2013). Polaronic trapping of electrons and holes by native defects in anatase TiO_2. *Physical Review B*, 80(23), 233102.

Morris, D., Dou, Y., Rebane, J., Mitchell, C. E. J., Egdell, R. G., Law, D. S. L., &

Casarin, M. (2000). Photoemission and STM study of the electronic structure of Nb-doped TiO_2. *Physical Review B*, 61(20), 13445.

Muscat, J., Swamy, V., & Harrison, N. M. (2002). First-principles calculations of the phase stability of TiO_2. *Physical Review B*, 65(22), 224112.

Munnix, S., & Schmeits, M. (1984). Electronic structure of ideal TiO_2 (110), TiO_2 (001), and TiO_2 (100) surfaces. *Physical Review B*, 30(4), 2202.

Mwonga P. V, (2014). *Ab-initio Study of Intrinsic Point Defects in Titanium Dioxide: A Density Function Theory Approach.* MSc. Thesis, University of Eldoret, pg (39).

Naldoni, A., Allieta, M., Santangelo, S., Marelli, M., Fabbri, F., Cappelli, S., & Dal Santo, V. (2012). Effect of nature and location of defects on band-gap narrowing in black TiO_2 nanoparticles. *Journal of the American Chemical Society*, 134(18), 7600-7603.

Na-Phattalung, S., Smith, M. F., Kim, K., Du, M. H., Wei, S. H., Zhang, S. B., & Limpijumnong, S. (2006). First-principles study of native defects in anatase TiO_2. *Physical Review B*, 73(12), 125205.

Navío, J., Colón, G., Litter, M. I., & Bianco, G. N. (1996). Synthesis, characterization and photocatalytic properties of iron-doped titania semiconductors prepared from TiO_2 and iron (III) acetylacetonate. *Journal of Molecular Catalysis A: Chemical*, 106(3), 267-276.

NISSHA. Dye-sensitized Solar Cell "EneLEAF". Retrieved, 06 May, 2016 from, *http://www.nissha.com/english/company/crd/eneleaf/index.html*.

Oliver, G. L., & Perdew, J. P. (1979). Spin-density gradient expansion for the kinetic energy. *Physical Review A*, 20(2), 397.

Peng, Y. H., Huang, G. F., & Huang, W. Q. (2012). Visible-light absorption and photocatalytic activity of Cr-doped TiO_2 nanocrystal films. *Advanced Powder Technology*, 23(1), 8-12.

Perdew, J. P., Burke, K., & Ernzerhof, M. (1996). Generalized gradient approximation made simple. *Physical review letters*, 77(18), 3865.

Perdew, J. P., & Levy, M,. (1983). Physical content of the exact Kohn-Sham orbital Energy: Band Gaps and derivatives. *Physical Review Letters*, 51(20), 1884-1887.

Perdew, J. P., (1991). Generalized gradient approximations for exchange and correlation: A look backward and forward. *Physica B: Condensed Matter*, 172(1), 1-6.

Pickett, W. E., (1989). Pseudo-potential methods in condensed matter applications. *Computer Physics Reports*, 9(3), 115-197.

Phelafel. VISUALIZATION OF DEFECTS IN GRAPHENE. Retrieved, 06 May, 2016 from, https://phelafel.technion.ac.il/ korens/defects.html.

Preshat Kamat. Photocatalysis. Retrieved, 06 May, 2016 from, https://www3.nd.edu/ kamatlab/research-photocatalysis.html.

Ramamoorthy, M., King-Smith, R. D., & Vanderbilt, D. (1994). Defects on TiO_2 (110) surfaces. *Physical Review B*, 49(11), 7709.

Rao, C. N. R., Gopalakrishnan, J., & Kulkarni, G. U. (2003). Advances in Chemistry: A Selection of CNR Rao's Publications (1994-2003). *World Scientific Publishing Company*.

Santara, B., Giri, P. K., Imakita, K., & Fujii, M. (2013). Evidence for Ti interstitial induced extended visible absorption and near infrared photoluminescence from undoped TiO_2 nano-ribbons: an in situ photo-luminescence study. *The Journal of Physical Chemistry C*, 117(44), 23402-23411.

Schaefer III, H. F. (2012). Quantum chemistry: the development of ab initio methods in molecular electronic structure theory. *Courier Corporation*.

Schaub, R., Thostrup, P., Lopez, N., Lægsgaard, E., Stensgaard, I., Norskov, J. K., & Besenbacher, F. (2001). Oxygen vacancies as active sites for water dissociation on rutile

TiO_2 (110). *Physical Review Letters*, 87(26), 266104.

Schleife, A., Varley, J. B., Janotti, A., & Van de Walle, C. G. (2013). Conductivity and transparency of TiO_2 from first principles. In SPIE Solar Energy Technology. *International Society for Optics and Photonics*. 882205-882205.

Setyawan, W., & Curtarolo, S. (2010). High-throughput electronic band structure calculations: Challenges and tools. *Computational Materials Science*, 49(2), 299-312.

Shao, G. (2008). Electronic structures of manganese-doped rutile TiO_2 from first principles. *The Journal of Physical Chemistry C*, 112(47), 18677-18685.

Sjostrom, V. V., Dufty, J. T, & Trickey, S. B. (2013). Local Spin-density Approximation Exchange-correlation Free-energy Functional. *arXiv preprint arXiv*:1311.4903.

Simons, P. Y., & Dachille, F. (1967). The structure of TiO_{2-II}, a high-pressure phase of TiO_{2-II}. *Acta Crystallographica*, 23(2), 334-336.

Smith, S. J., & Sutcliffe, B. T. (1997). The development of computational chemistry in the United Kingdom. *Reviews in Computational Chemistry*, Volume 10, 271-316.

Stausholm-Møller, J., Kristoffersen, H. H., Hinnemann, B., Madsen, G. K., & Hammer, B. (2010). DFT+ U study of defects in bulk rutile TiO_2. *The Journal of chemical physics*, (133), 144708-144708.

Strunk, J., Vining, W. C., & Bell, A. T. (2010). A Study of Oxygen Vacancy Formation and Annihilation in Submonolayer Coverages of TiO_2 Dispersed on MCM-48. *The Journal of Physical Chemistry C*, 114(40), 16937-16945.

Sun, Y., Egawa, T., Zhang, L., & Yao, X., (2002). High anatase-rutile transformation temperatures of anatase titania nanoparticles prepared by metalorganic chemical vapor deposition. *Japanese Journal of Applied Physics*, 41(8B), 945-948.

Thygesen, K. S., & Mortensen, J. J. (2008). Localized Atomic Orbital Basis Sets in the Projector Augmented Wave Method.

Tomlinson, S. M., Freeman, C. M., Catlow, C. R. A., Donnerberg, H., & Leslie, M. (1989). Atomistic simulation studies of technologically important oxides. *Journal of the Chemical Society, Faraday Transactions 2: Molecular and Chemical Physics*, 85(5), 367-383.

Trenczek-Zajac, A., Pamula, E., Radecka, M., Kowalski, K., Reszka, A., Brudnik, A., & Zakrzewska, K. (2012). Thin films of TiO_2:N for photo-electrochemical applications. *Journal of nanoscience and nanotechnology*, 12(6), 4703-4709.

Umebayashi, T., Yamaki, T., Itoh, H., & Asai, K. (2002). Analysis of electronic structures of 3d transition metal-doped TiO_2 based on band calculations. *Journal of Physics and Chemistry of Solids*, 63(10), 1909-1920.

Vosko, S. H., Wilk, L., & Nusair, M. (1980). Accurate spin-dependent electron liquid correlation energies for local spin density calculations: a critical analysis. *Canadian Journal of physics*, 58(8), 1200-1211.

Wahlbeck, P. G., & Gilles, P. W. (1966). Reinvestigation of the phase diagram for the system titanium–oxygen. *Journal of the American Ceramic Society*, 49(4), 180-183.

Wahle, A., Mitchell, S. C., Olszewski, M. E., Long, R. M., & Sonka, M. (2001). Accurate visualization and quantification of coronary vasculature by 3D/4D fusion from biplane angiography and intravascular ultrasound. *In EOS/SPIE European Biomedical Optics Week. International Society for Optics and Photonics*, 144-155.

Waldner, P., & Eriksson, G. (1999). Thermodynamic modelling of the system titanium-oxygen. *Calphad*, 23(2), 189-218.

Wang, C. S., Klein, B. M., and Krakauer, H. (1985). Theory of magnetic and structural ordering in iron. *Physical review letters*, 54(16), 1852.

Wang, X., Wang, F. H., Shang, J. X., & Zhou, Y. S. (2012). Ab initio studies of Nb doping effect on the formation of oxygen vacancy in rutile TiO_2. *Journal of Physics and Chemistry of Solids*, 73(1), 84-93.

Wang, Y., & Perdew, J. P., (1991). Spin scaling of the electron-gas correlation energy in the high-density limit. *Physical Review B*, 43(11), 8911.

Wang, Y., Zhang, R., Li, J., Li, L., & Lin, S., (2014). First-principles study on transition metal-doped anatase TiO_2. *Nanoscale research letters*, 9(1), 1-8.

Weibel, A., Bouchet, R., & Knauth, P., (2006). Electrical properties and defect chemistry of anatase (TiO_2). *Solid State Ionics*, 177(3), 229-236.

Wendt, S., Tomlinson, S. M., Freeman, C. M., Catlow, C. R. A., Donnerberg, H., & Leslie, M. (1989). Atomistic simulation studies of technologically important oxides. *Journal of the Chemical Society, Faraday Transactions 2: Molecular and Chemical Physics*, 85(5), 367-383.

Xing-Gang, H., An-Dong, L., Mei-Dong, H., Bin, L., & Xiao-Ling, W., (2009). First-principles band calculations on electronic structures of Ag-doped rutile and anatase TiO_2. *Chinese Physics Letters*, 26(7), 077106.

Yang, S., Halliburton, L. E., Manivannan, A., Bunton, P. H., Baker, D. B., Klemm, M., & Fujishima, A., (2009). Photoinduced electron paramagnetic resonance study of electron traps in TiO_2 crystals: oxygen vacancies and Ti^{3+} ions. *Applied Physics Letters*, 94(16), 162114-162114.

Yang, K., Dai, Y., Huang, B., & Feng, Y. P., (2014). First-principles GGA+ U study of the different conducting properties in pentavalent-ion-doped anatase and rutile TiO_2. *Journal of Physics D: Applied Physics*, 47(27), 275101.

Yim, C. M., Pang, C. L., & Thornton, G., (2010). Oxygen vaccancy origin of the surface band gap state of TiO_2 (110). *Physical Review letters*, 104(3), 036806.

Ying, Y., Qing, F., Weihua, W., & Yin, W., (2013). First-principle study on the electronic and optical properties of the anatase TiO_2 (101) surface. *Journal of Semiconductors*, 34(7), 073004.

Yu, N., & Halley, J. W., (1995). Electronic structure of point defects in rutile TiO_2.

Physical Review B, 51(8), 4768.

Zakhov, M., (2013). Performance of numerical atom-centered basis set in the ground-state correlated calculations of noncovalent interactions: Water and methane dimer cases. *International Journal of Quantum Chemistry*, 113(150, 1899-1918).

Zhang, H., Chen, B., Banfield, J. F., & Waychunas, G. A., (2008). Atomic structure of nanometer-sized amorphous TiO_2. *Physical Review B*, 78(21), 214106.

Zhang, J., Zhou, P., Liu, J., & Yu, J., (2014). New understanding of the difference of photocatalytic activity among anatase, rutile and brookite TiO_2. *Phys. Chem. Chem. Phys.*, 16(38), 20382-20386.

Zhao, Y., Schultz, N. E., & Truhlar, D. G., (2005). Exchange-correlation functional with broad accuracy for metallic and nonmetallic compounds, kinetics, and noncovalent interactions.*The Journal of chemical physics*, 123(16), 161103.

Zhu, W., Qiu, X., Iancu, V., Chen, X. Q., Pan, H., Wang, W., & Zhang, Z., (2009). Band gap narrowing of titanium oxide semiconductors by noncompensated anion-cation co-doping for enhanced visible-light photoactivity. *Physical review letters*, 103(22), 226401.

Zhu, Y. F., Zhang, J., Xu, L., Guo, Y., Wang, X. P., Du, R. G., & Lin, C. J., (2013). Fabrication and photoelectrochemical properties of ZnS/Au/TiO_2 nanotube array films. *Phys. Chem. Chem. Phys.*, 15(11), 4041-4048.

toc

APPENDIX I

Convergence Tests of Rutile TiO_2

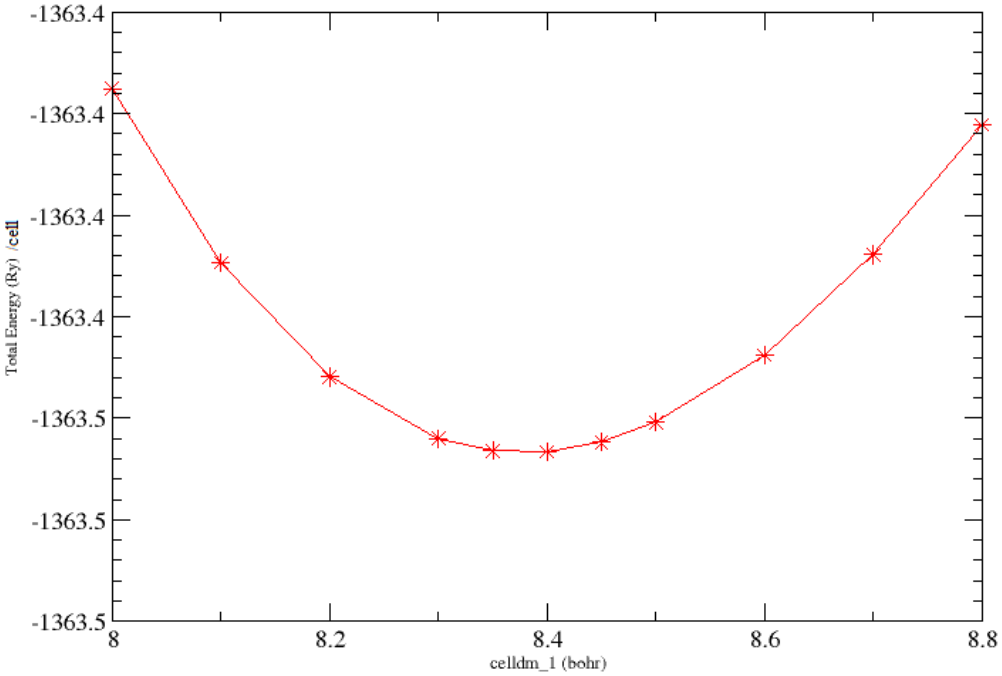

Figure A.1: Energy versus lattice parameter, a_o, for bulk rutile TiO_2.

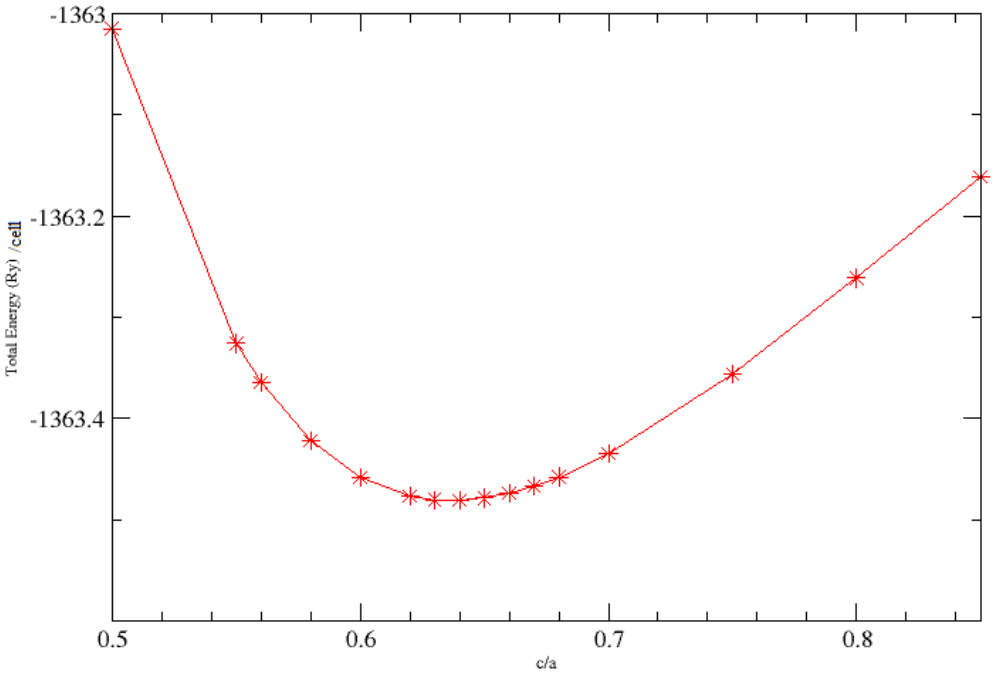

Figure A.2: Energy versus ratio c/a_o for bulk rutile TiO_2.

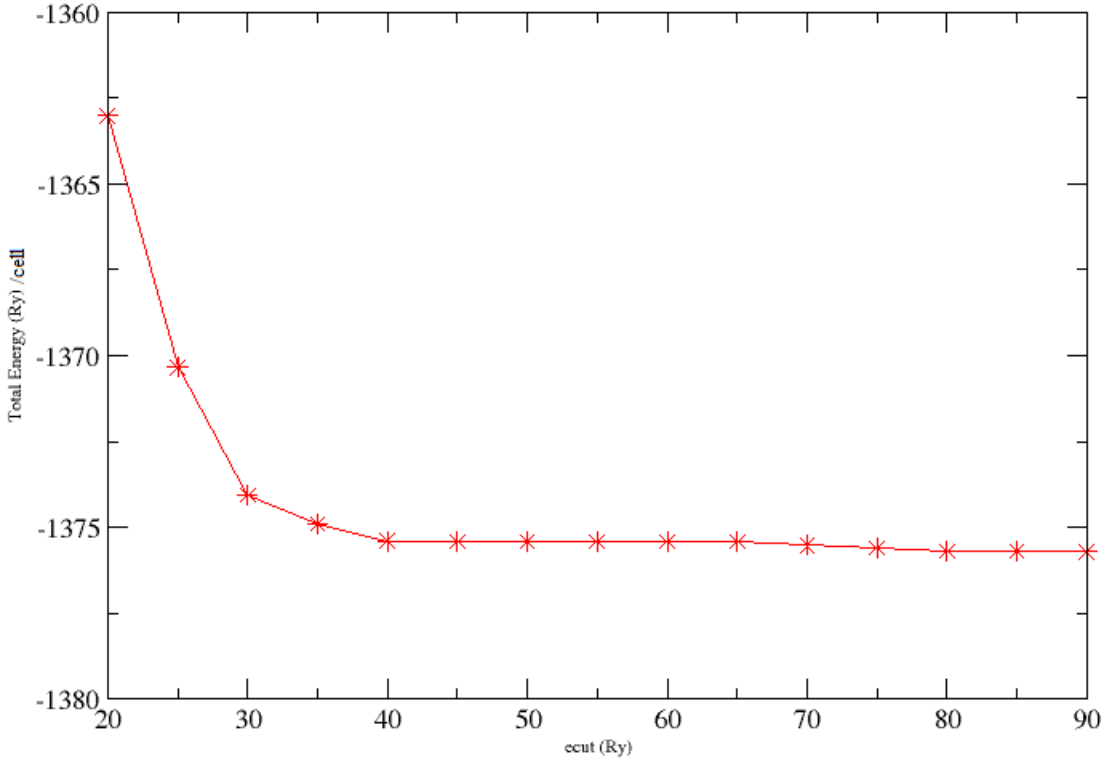

Figure A.3: Energy versus Plane wave cutoff energy for bulk rutile TiO_2.

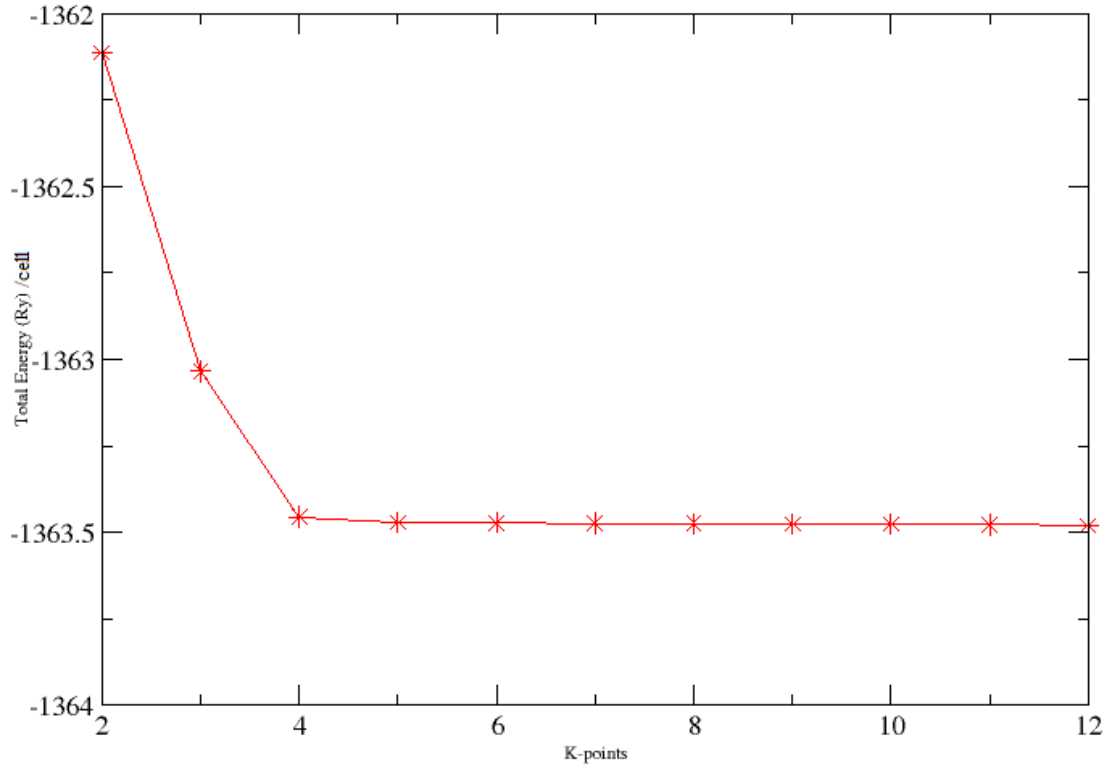

Figure A.4: Energy versus k-points for bulk rutile TiO_2.

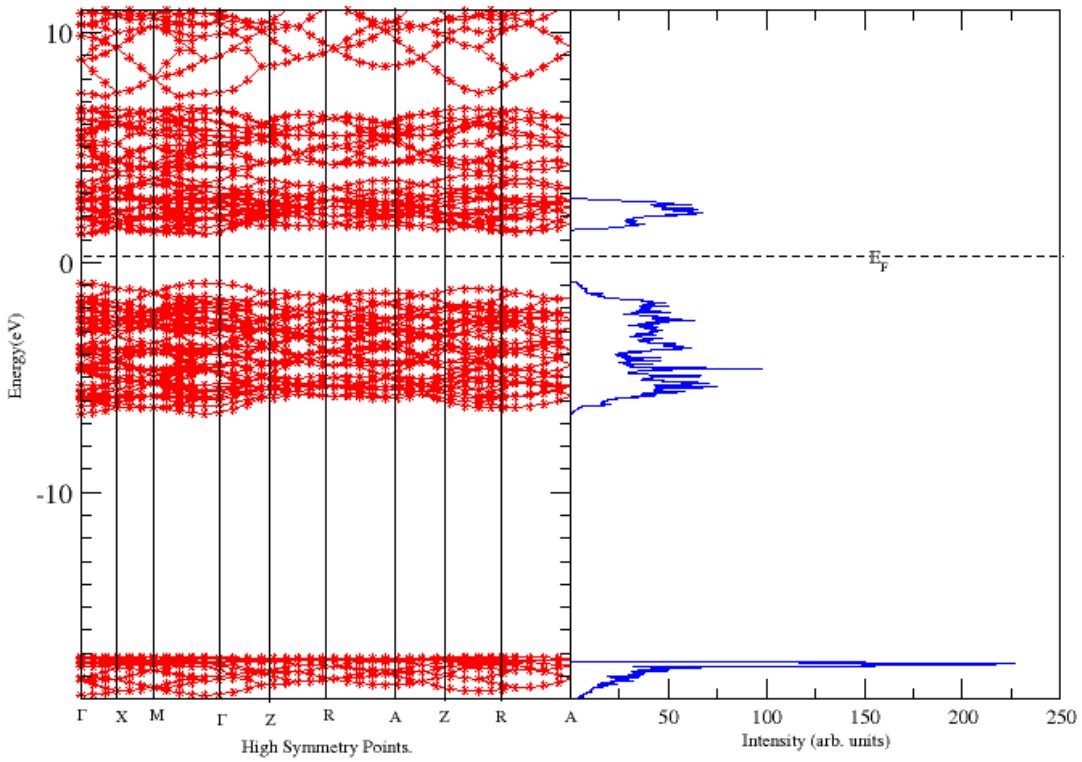

Figure A.5: Band & DOS Structures of pristine rutile TiO_2 calculated using DFT (solid) and DFT+U (dashed).

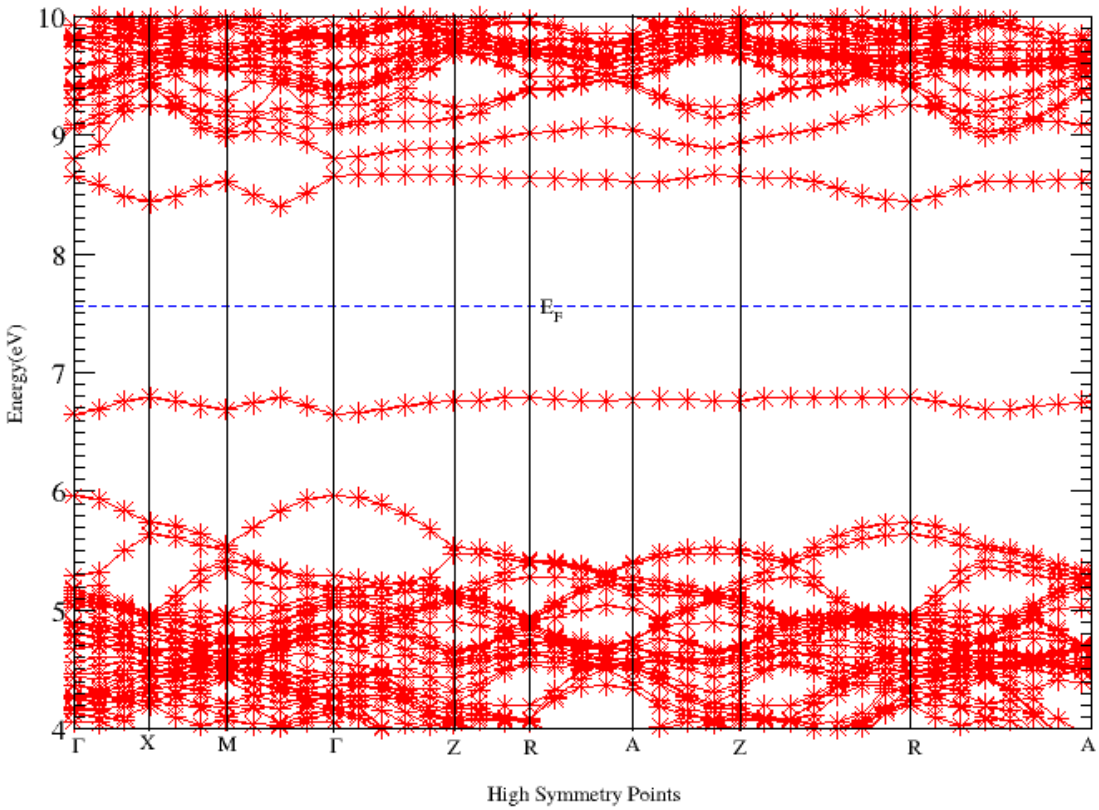

Figure A.6: Bands structure of rutile TiO_2 showing mid-gap states following the introduction of an oxygen vacancy defect.

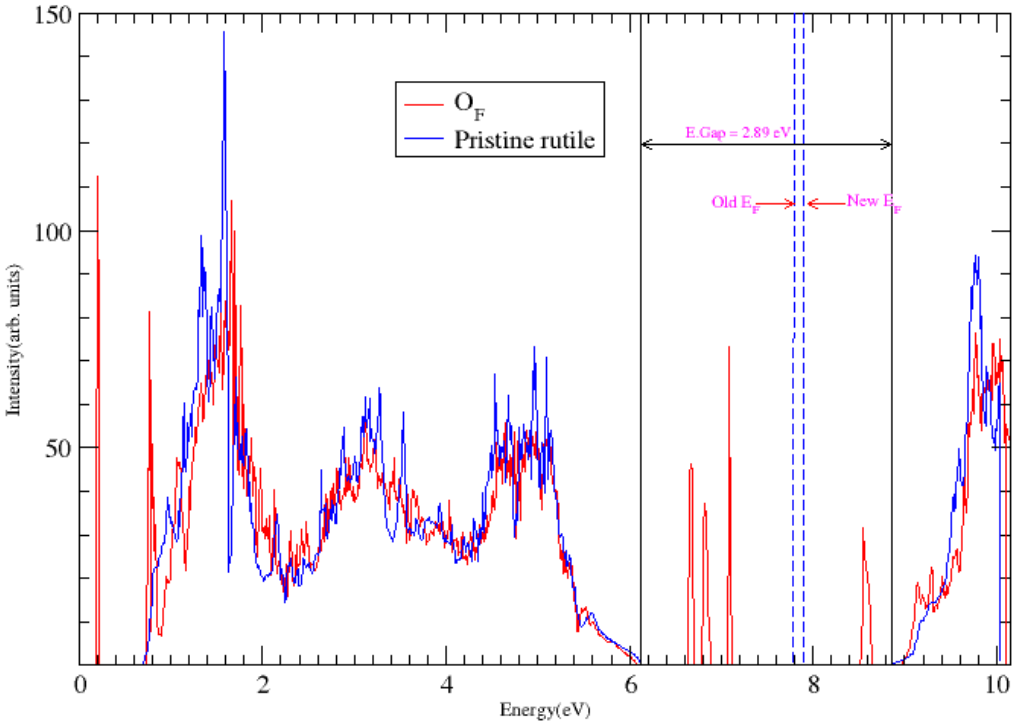

Figure A.7: DOS structure of rutile TiO_2 showing mid-gap states following the introduction of oxygen Frenkel defect.

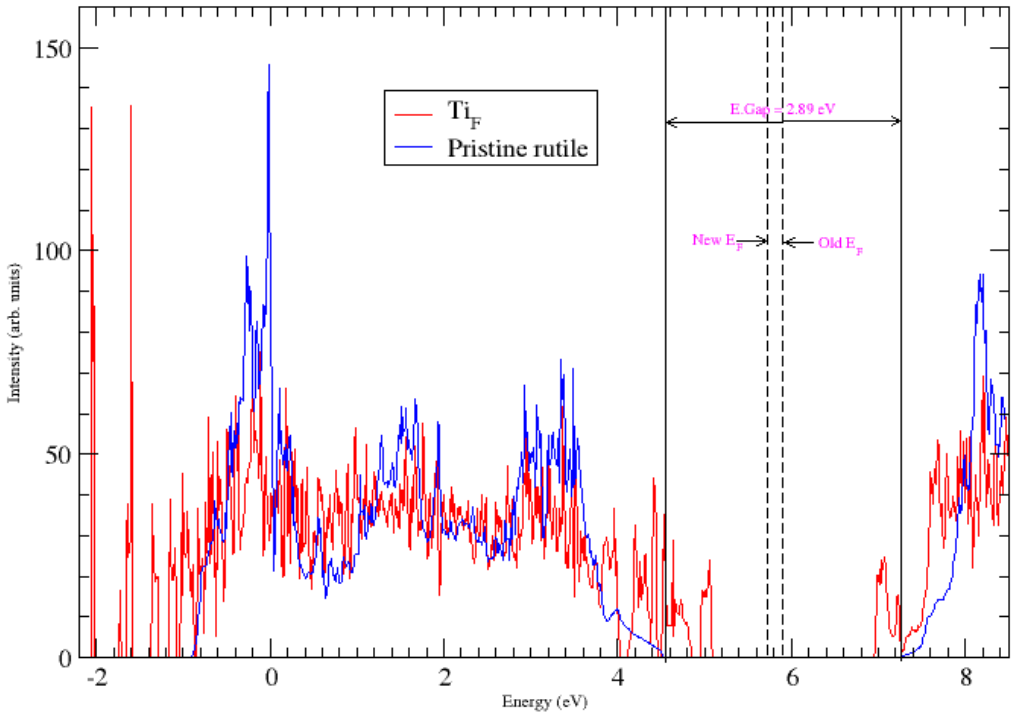

Figure A.8: DOS structure of rutile TiO_2 following the introduction of titanium Frenkel defects.

APPENDIX II

Convergence Tests of Anatase TiO_2

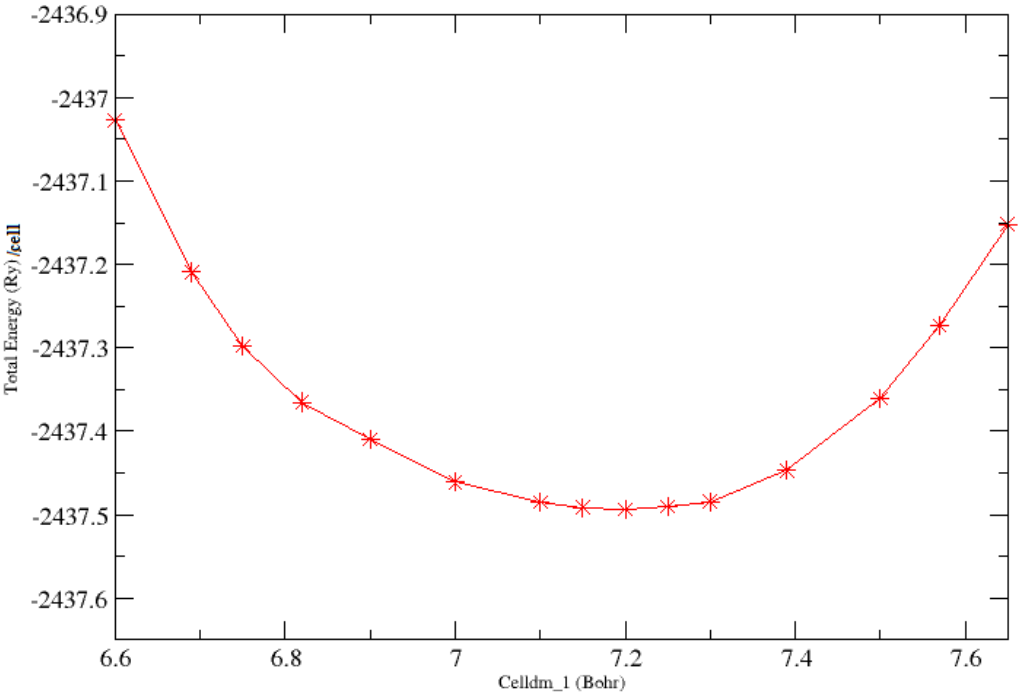

Figure B.1: Energy versus lattice parameter, a_o, for bulk anatase TiO_2.

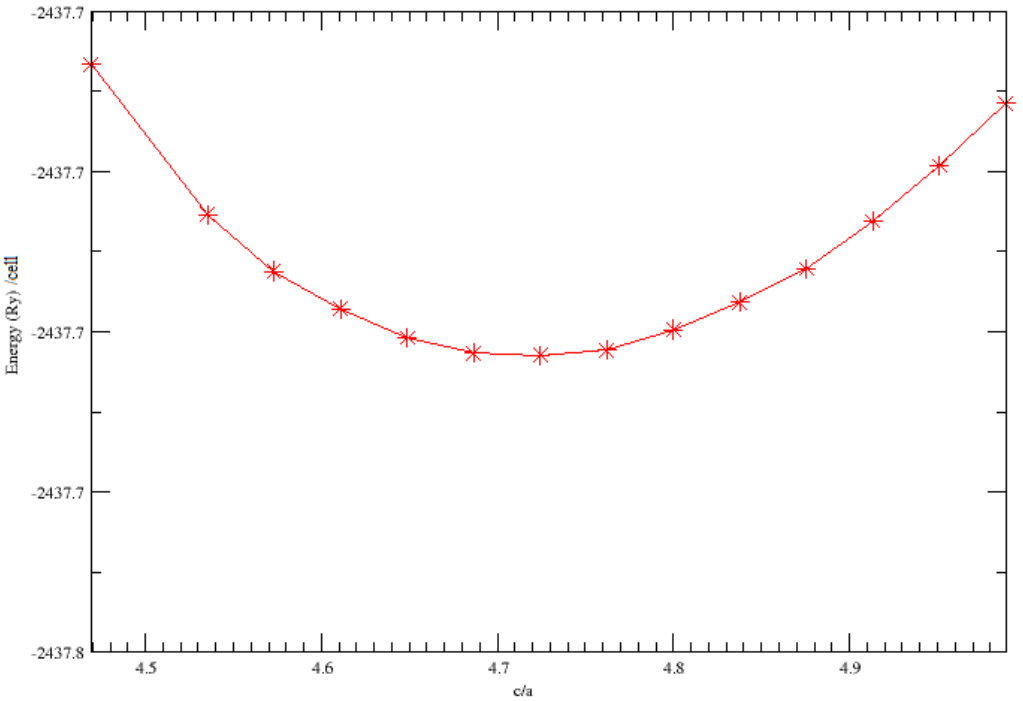

Figure B.2: Energy versus ratio c/a_o for bulk anatase TiO_2.

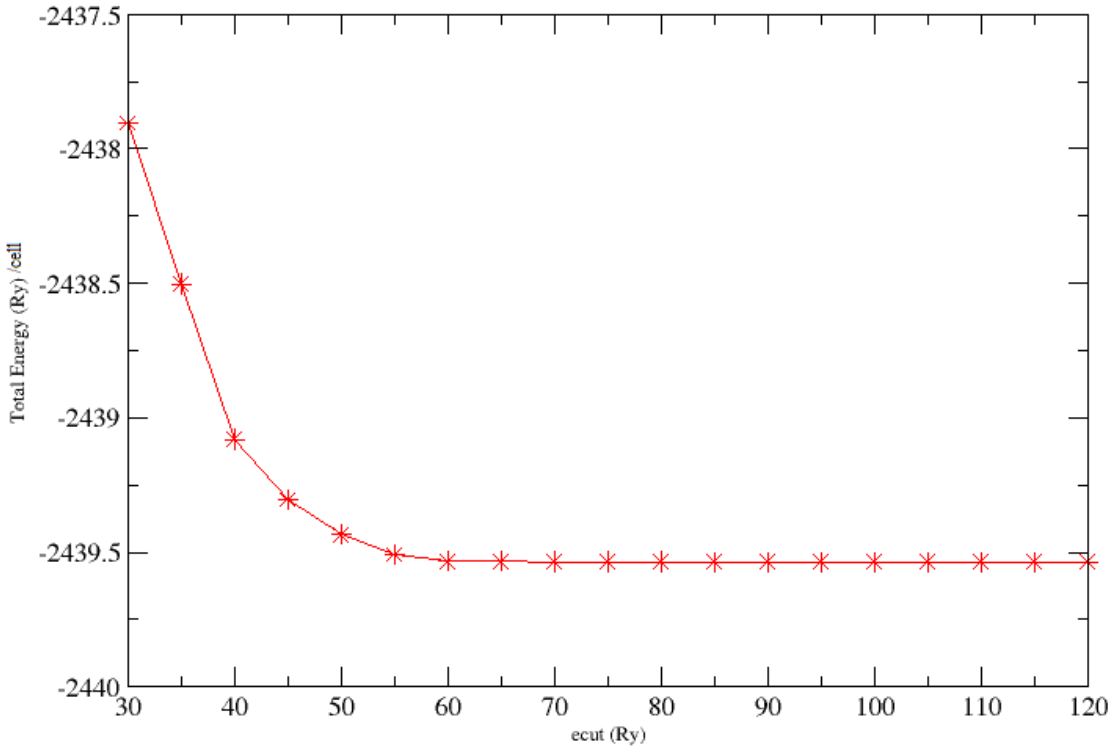

Figure B.3: Energy versus plane wave cutoff energy for bulk anatase TiO_2.

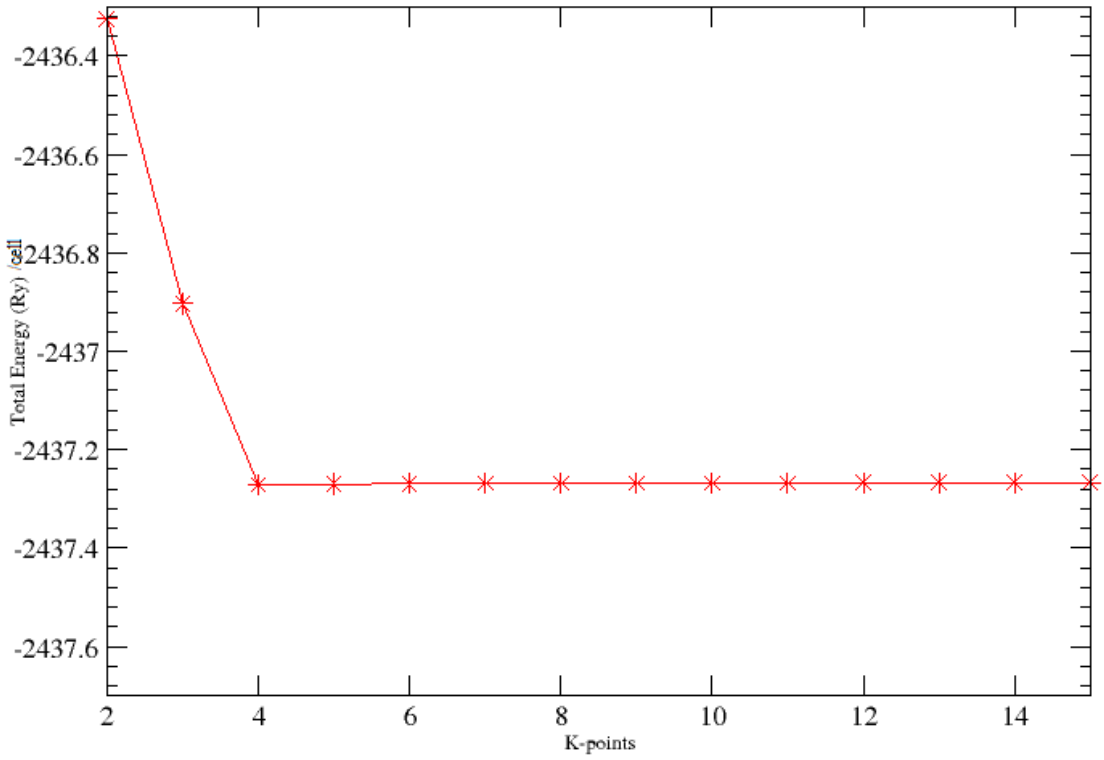

Figure B.4: Energy versus K-point for bulk anatase TiO_2.

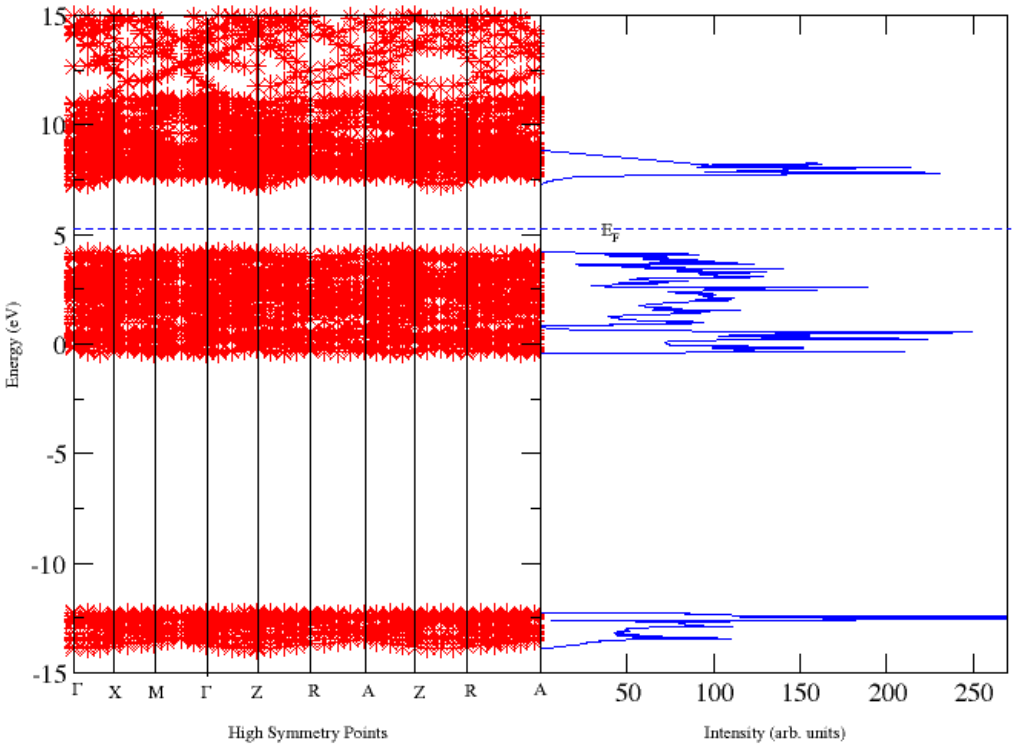

Figure B.5: Bands structure and DOS for pristine anatase TiO_2.

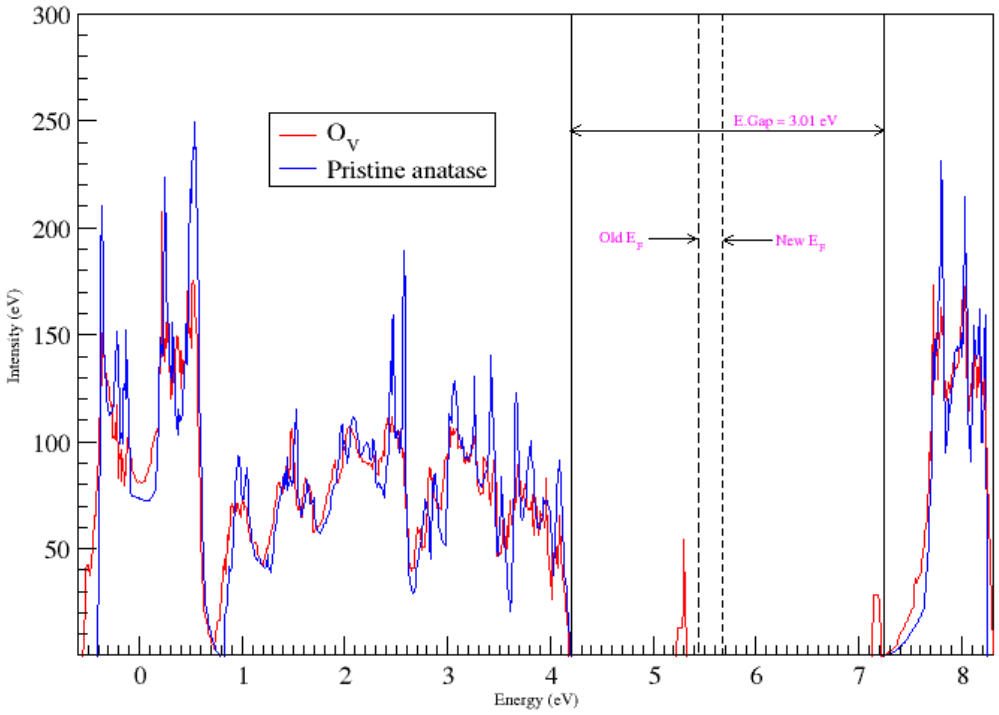

Figure B.6: DOS for pristine anatase TiO_2 (blue) compared with those occurring in anatase TiO_2 with oxygen vacancy (red).

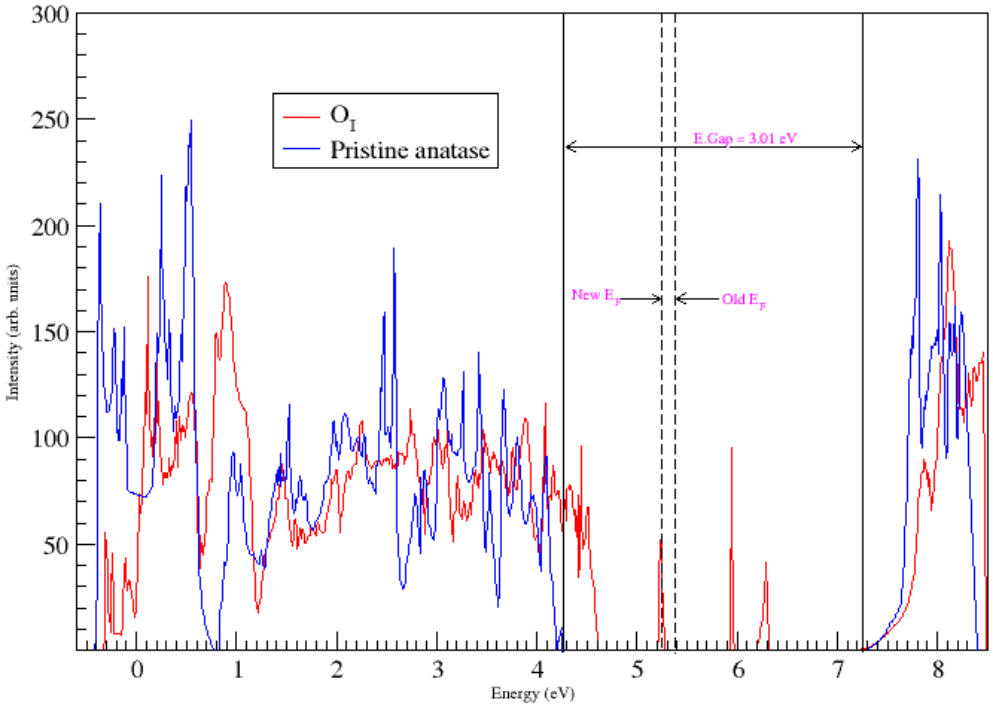

Figure B.7: DOS for pristine anatase TiO_2 (blue) compared with those occurring following the introduction of oxygen interstitial (red).

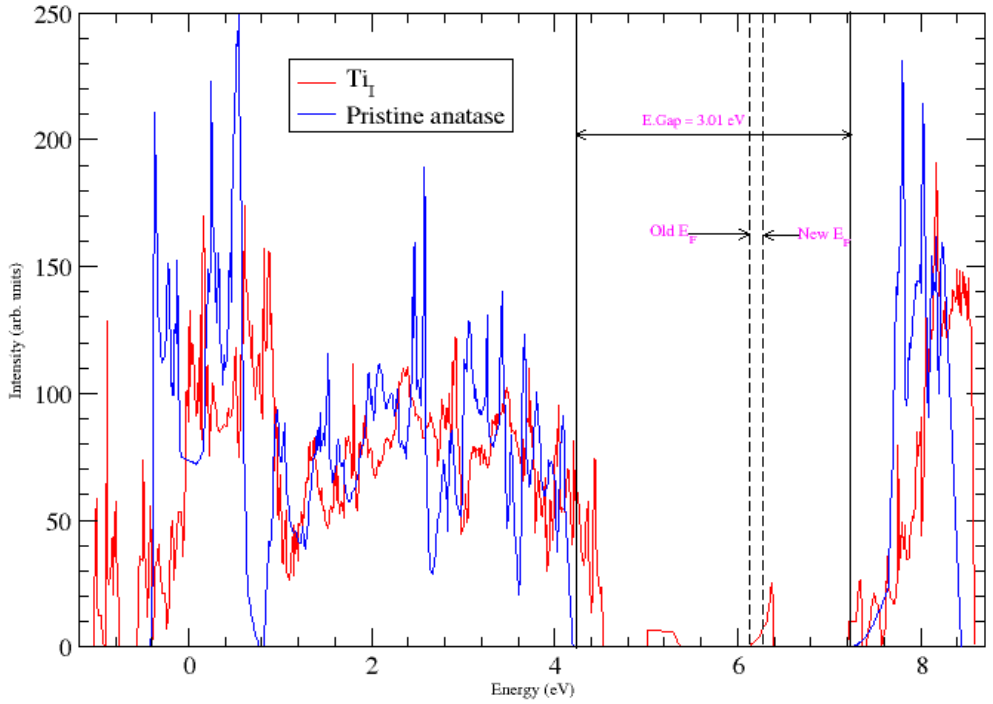

Figure B.8: DOS for pristine anatase TiO_2 (blue) compared with those occurring following the introduction of titanium interstitial (red).

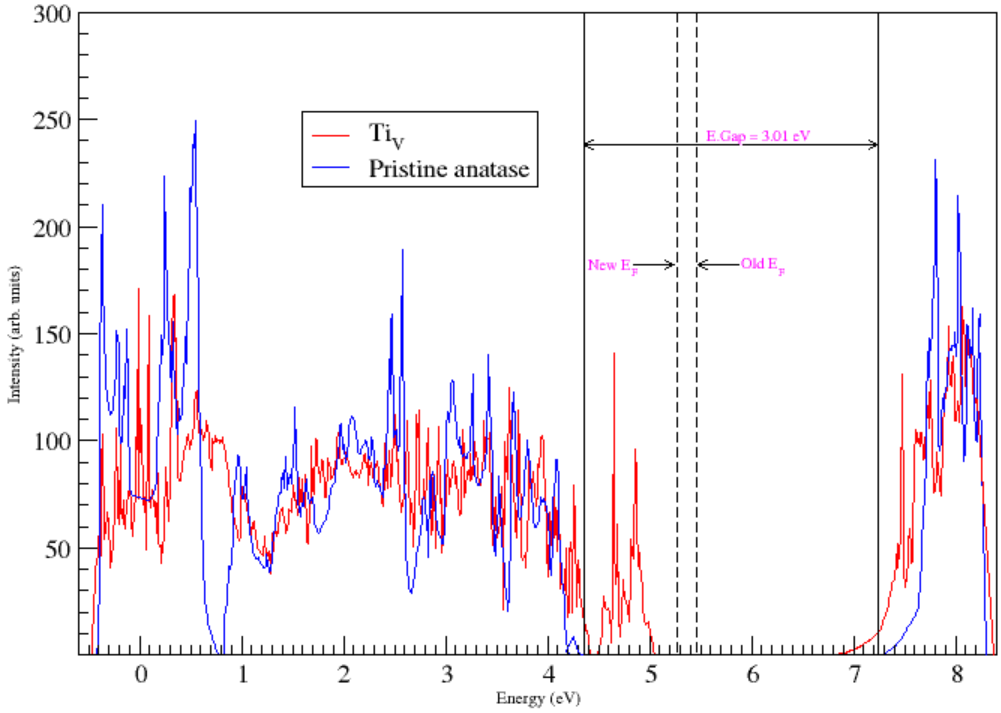

Figure B.9: DOS for pristine anatase TiO_2 (blue) compared with those occurring following the introduction of titanium vacancy (red).

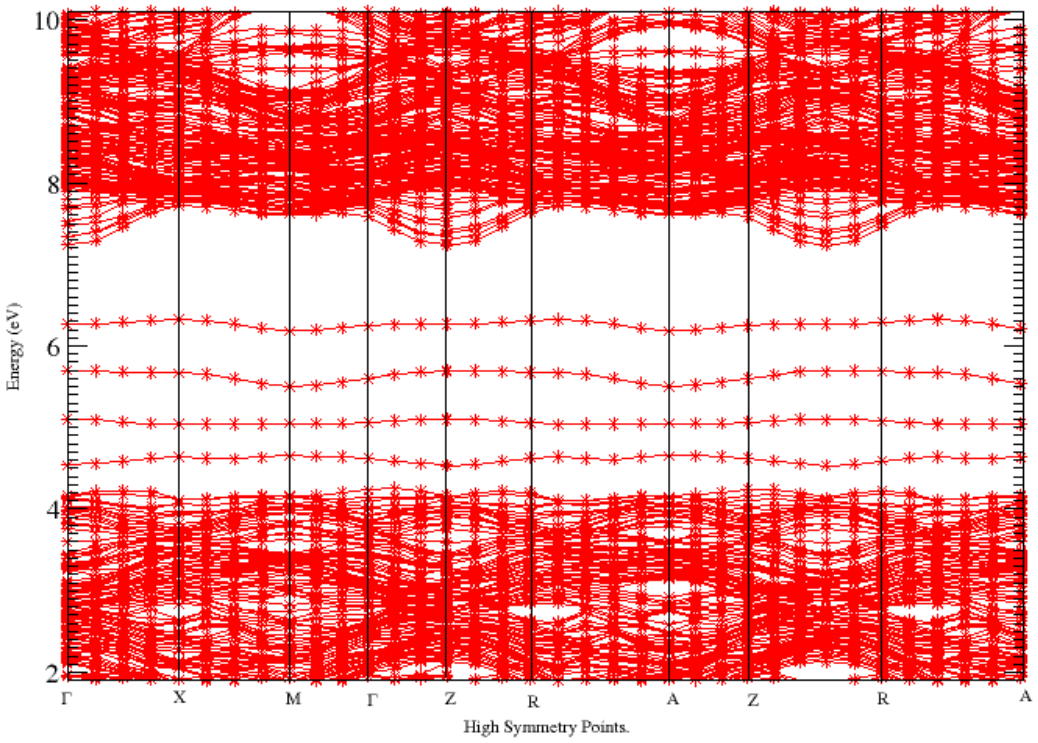

Figure B.10: Bands for anatase TiO_2 showing mid-gap states and downward bending of the CB following introduction of Ti_F.

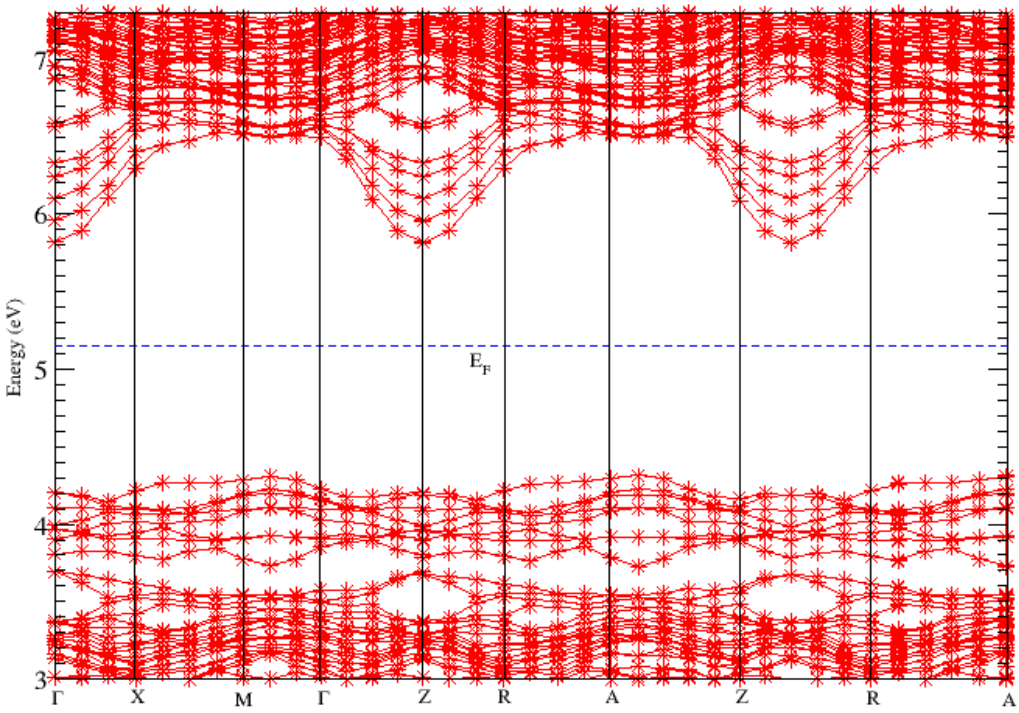

Figure B.11: Band structure of anatase TiO_2 showing mid-gap states and downward bending of the CB following introduction of Ti_V.

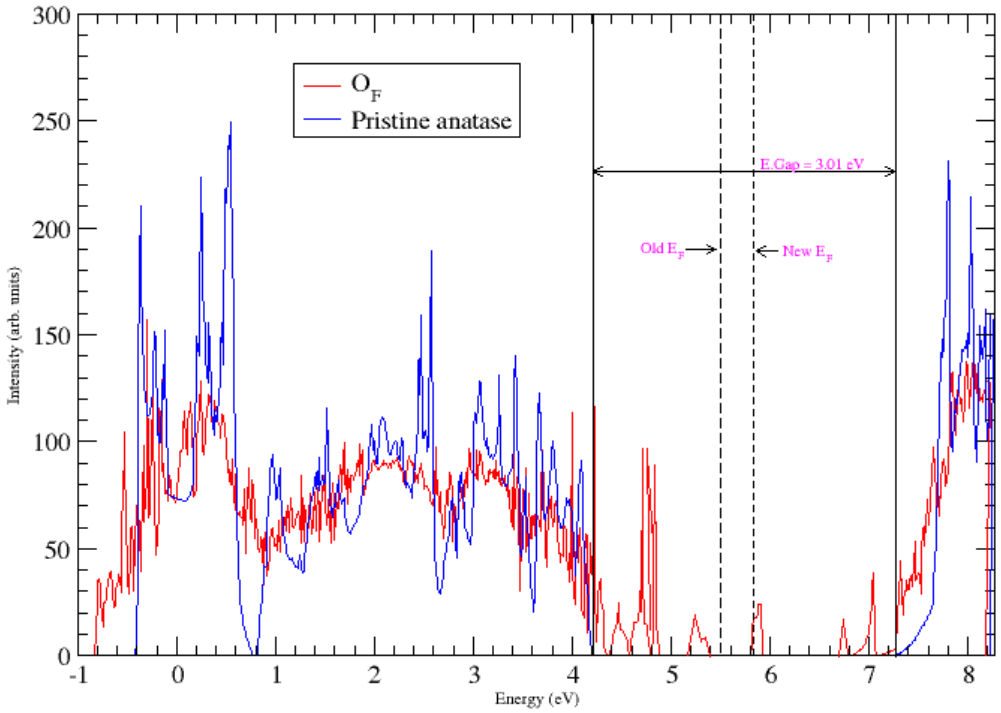

Figure B.12: DOS for pristine anatase TiO_2 (blue) compared with those occurring following the introduction of O_F (red).

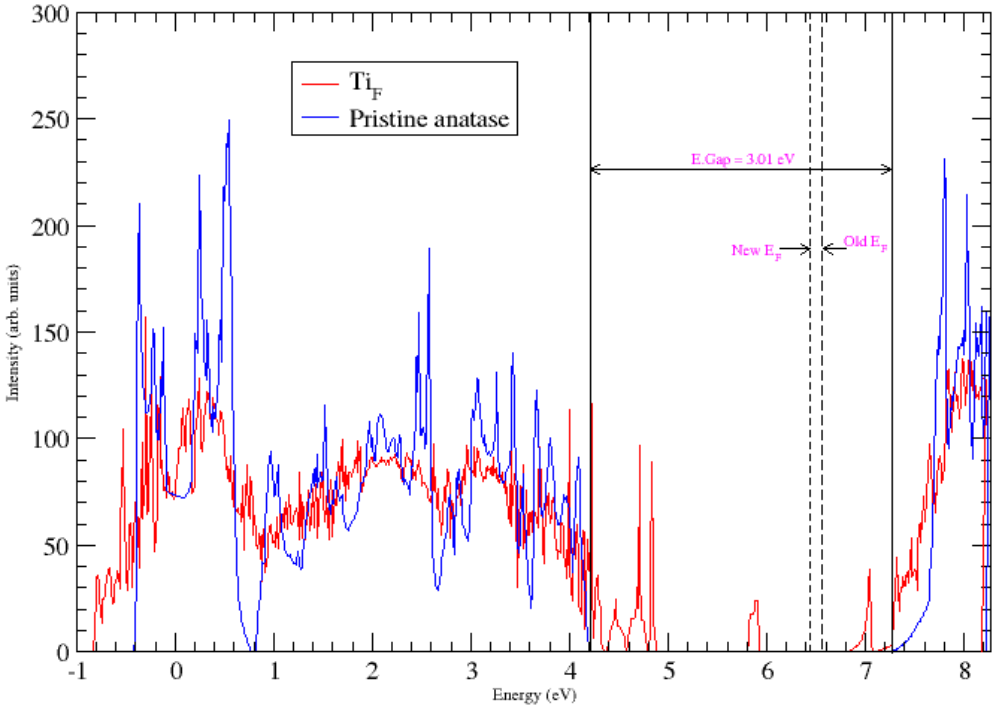

Figure B.13: DOS for pristine anatase TiO_2 (blue) compared with those occurring following the introduction of Ti_F (red).

APPENDIX III

DOS Deviations

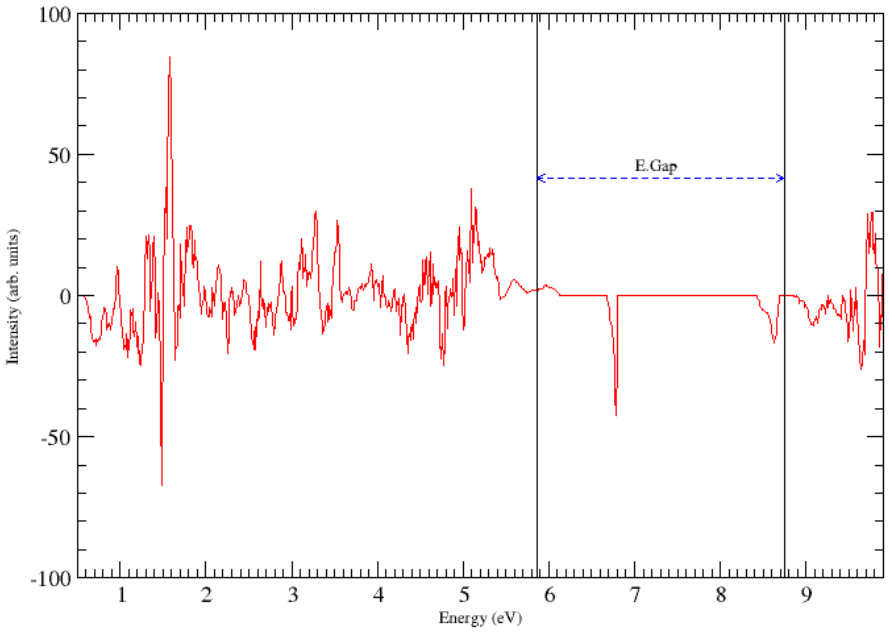

Figure C.1: Diagramatic representation of the DOS difference between those of pristine and those occurring following the introduction of O_F in rutile TiO_2.

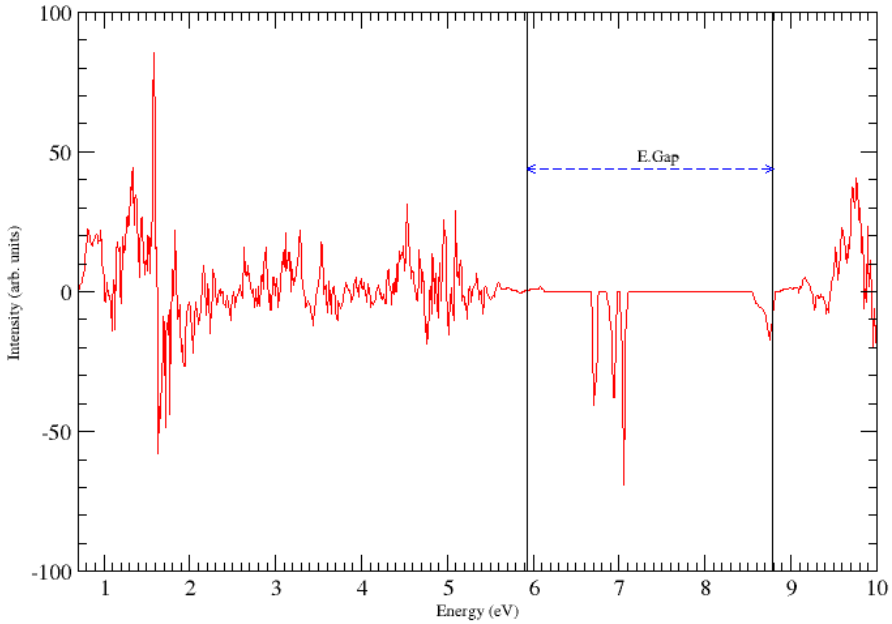

Figure C.2: Diagramatic representation of the DOS difference between those of pristine and those occurring following the introduction of O_I in rutile TiO_2.

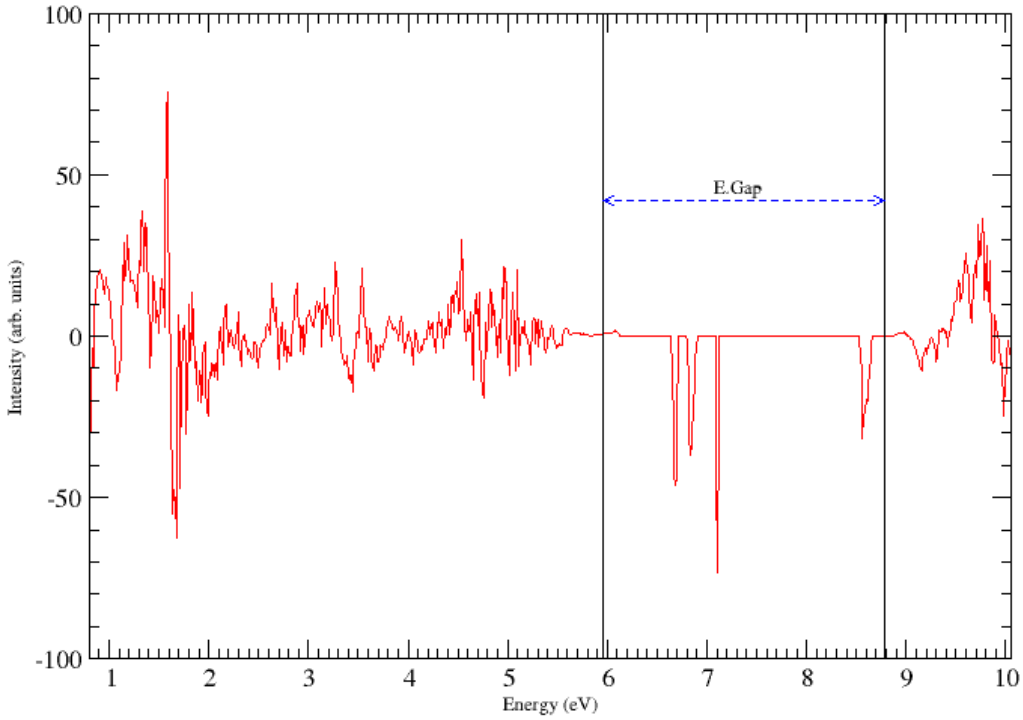

Figure C.3: Diagramatic representation of the DOS difference between those of pristine and those occurring following the introduction of O_F in rutile TiO_2.

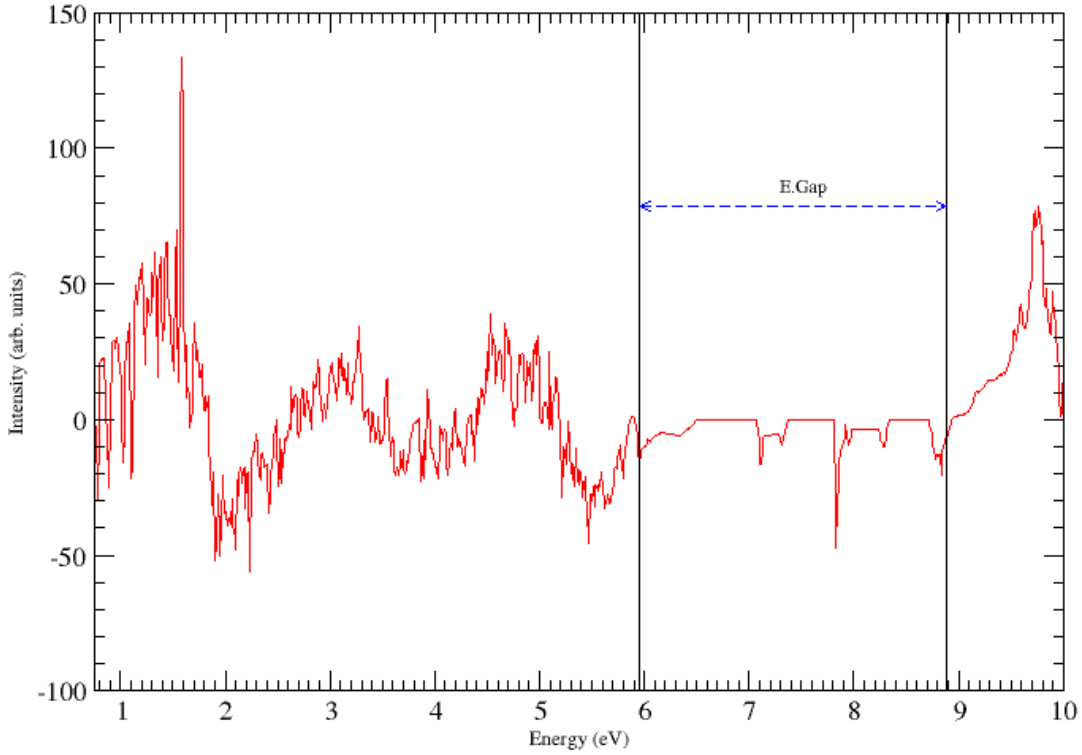

Figure C.4: Diagramatic representation of the DOS difference between those of pristine and those occurring following the introduction of Ti_I in rutile TiO_2.

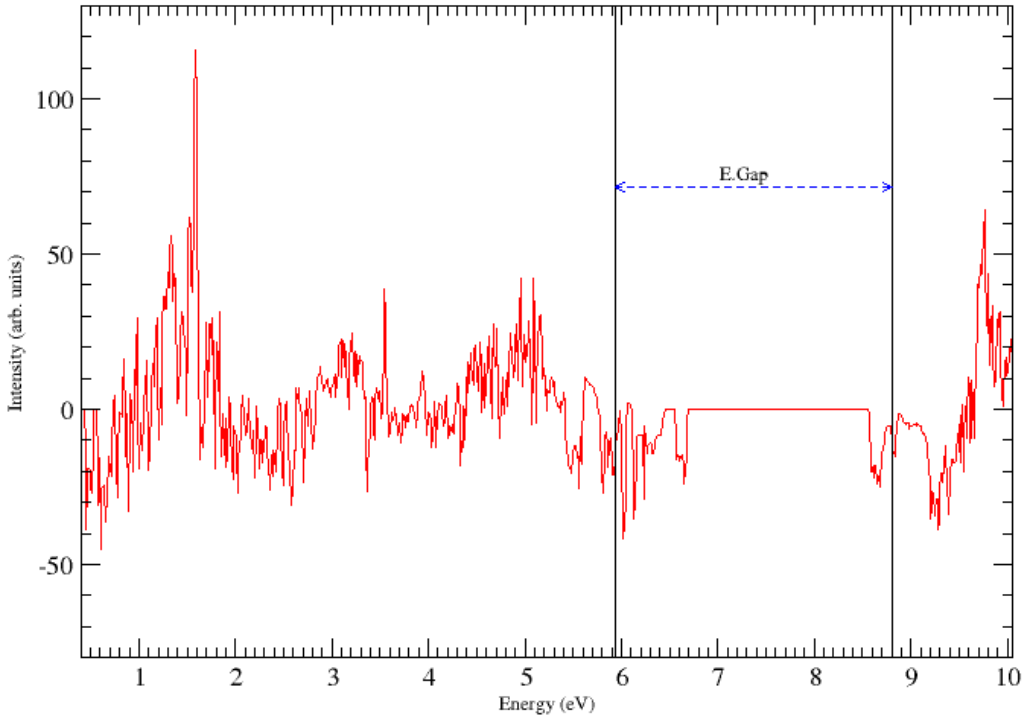

Figure C.5: Diagramatic representation of the DOS difference between those of pristine and those occurring following the introduction of Ti_F in rutile TiO_2.

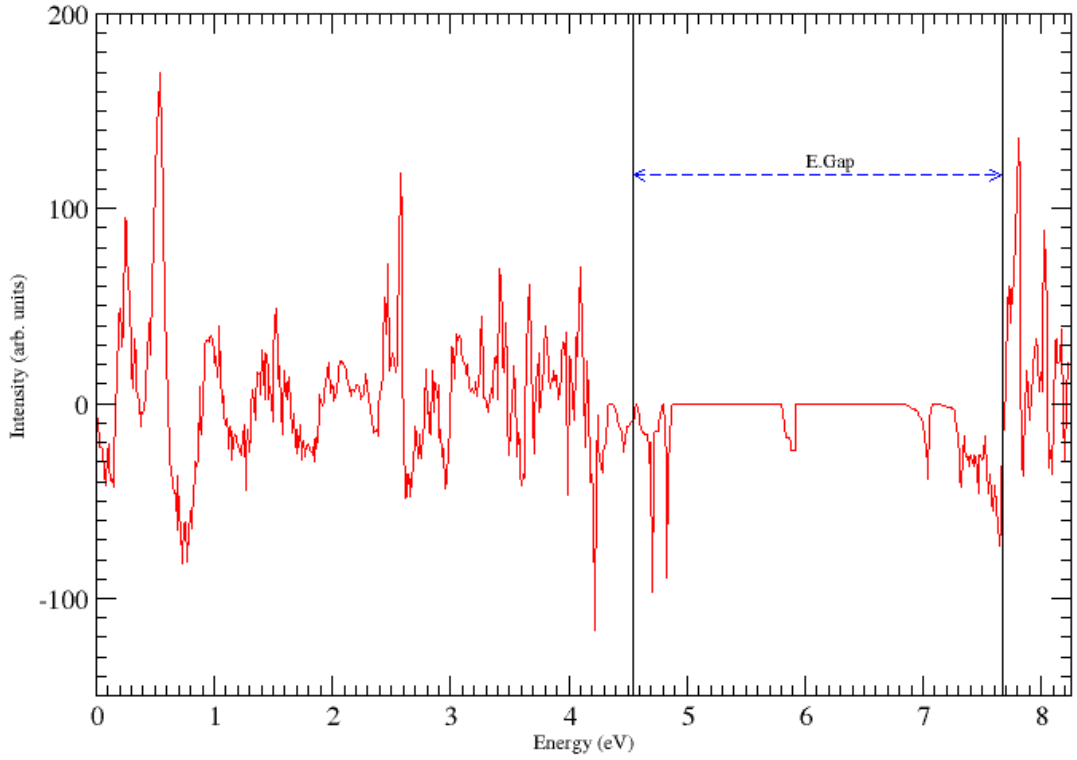

Figure C.6: Diagramatic representation of the DOS difference between those of pristine and those occurring following the introduction of O_I in anatase TiO_2.

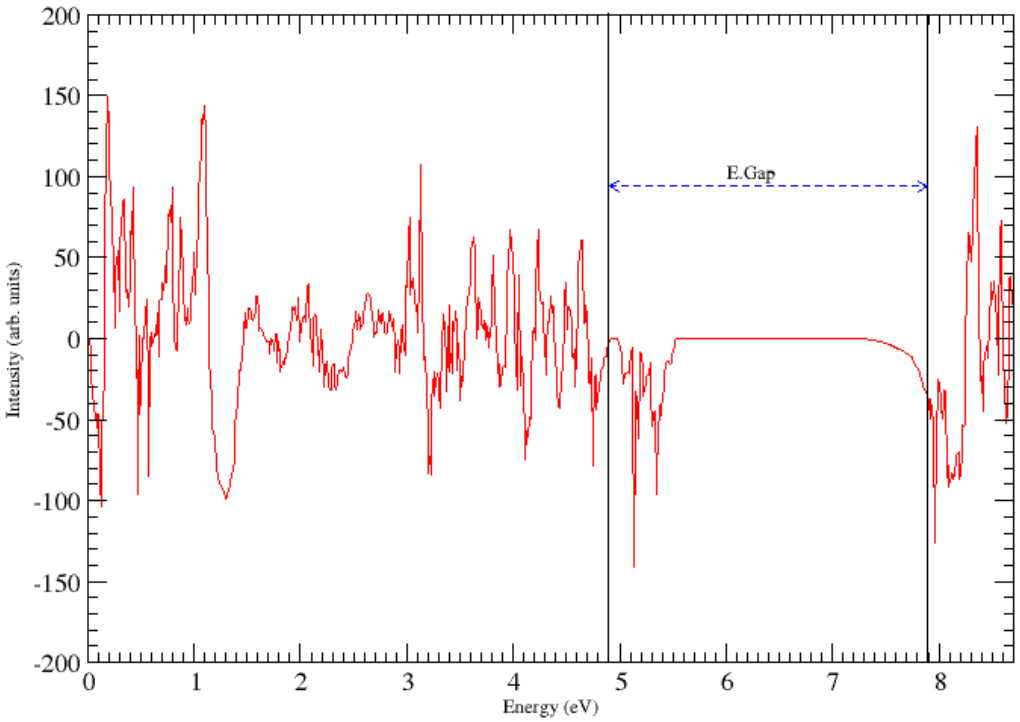

Figure C.7: Diagramatic representation of the DOS difference between those of pristine and those occurring following the introduction of Ti_V in anatase TiO_2.

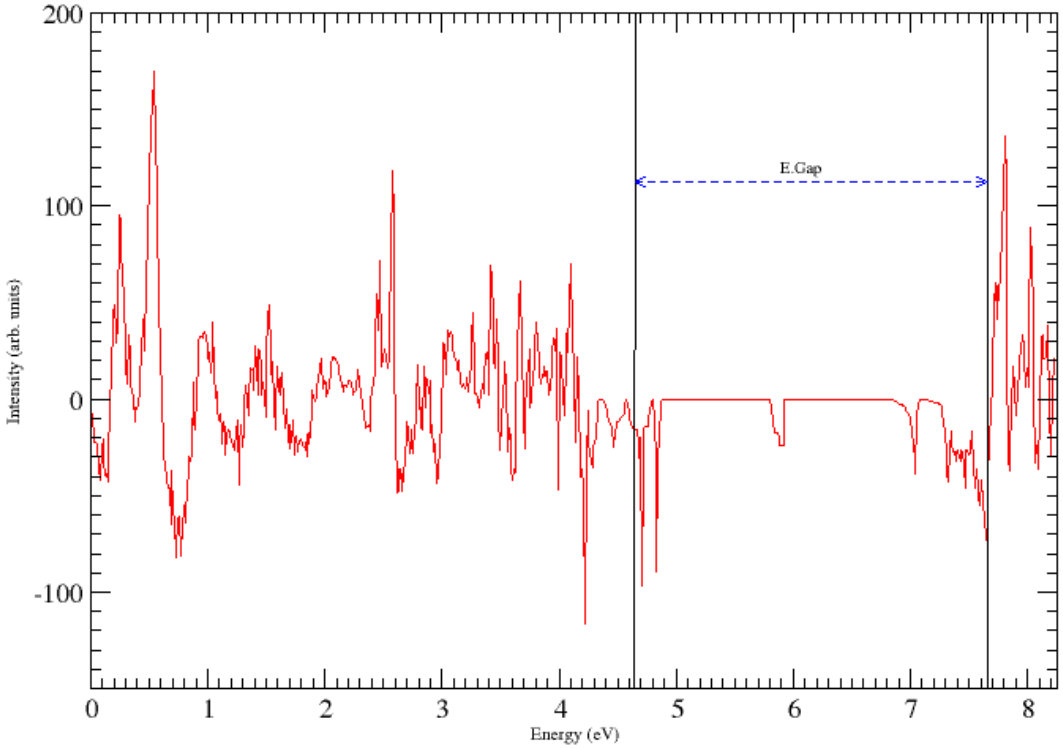

Figure C.8: Diagramatic representation of the DOS difference between those of pristine and those occurring following the introduction of Ti_F in anatase TiO_2.

APPENDIX IV

Defect Formation Energies for NC-PPs & US-PPs.

Table D.1: Comparison of the calculated DFE per formula in Rutile TiO_2 using NC-PPs and US-PPs.

$Defect$	$NC-PPs\,(eV)$	$US-PPs\,(eV)$
$Oxygen\,Vacancy$	8.19	7.167
$Oxygen\,Interstitial$	-7.36	-2.597
$Titanium\,Vacancy$	1.14	1.270
$Titanium\,Interstitial$	-0.17	-0.553
$Oxygen\,Frenkel$	-0.19	-0.117
$Titanium\,Frenkel$	0.26	0.251

Table D.2: Comparison of the calculated DFE per formula in Anatase TiO_2 using NC-PPs and US-PPs.

$Defect$	$NC-PPs\,(eV)$	$US-PPs\,(eV)$
$Oxygen\,Vacancy$	9.33	4.523
$Oxygen\,Interstitial$	-8.76	-3.226
$Titanium\,Vacancy$	1.39	0.620
$Titanium\,Interstitial$	-0.22	-0.489
$Oxygen\,Frenkel$	-0.33	-0.156
$Titanium\,Frenkel$	0.29	0.171

APPENDIX V

Pseudo-Potentials Used in this Study.

Table E.1: Pseudo-potentials used for both rutile and anatase TiO_2.

Type of Atom	Pseudo-Potential Type
Oxygen	O.pbe-mt-fhi.UPF
Titanium	Ti.pbe-mt-fhi.UPF

Oxygen

This pseudo-potential was generated on 10-07-2012 using FH198PP and converted with fhi2upf.x v.5.0.1. It was generated with a Scalar Relativistic Calculation. Its L component and cut-off radius for the Local Potential was 20.0000. The PP type is SL.

Table E.2: Oxygen pseudo-potentials

nl	pn	l	occ	Rcut	Rcut US	E pseu
2s	2	0	2.00	0.000	0.000	0.000000
. 2p	2	1	4.00	0.000	0.000	0.000000
3d	3	2	0.00	0.000	0.000	0.000000
4f	4	3	0.00	0.000	0.000	0.000000

Norm-conserving Pseudopotential	NC
Nonlinear Core Correction	F
PBE Exchange-Correlation Functional	SLA, PW, PBE
Local Potential Cut-off Radius	0.000000000000000E+000
Z Valence	6.0000000000000000
Total Energy	0.00000000000000E+000
Number of Points in Mesh	473
Max Angular Momentum Component	3
Number of Wavefunctions	4
Number of Projectors	3

Titanium

This pseudo-potential was generated on 10-07-2012 using FH198PP and converted with fhi2upf.x v.5.0.1. It was generated with a Non-Relativistic Calculation. Its L component and cut-off radius for the Local Potential was 10.0000. PP SL.

Table E.3: Titanium pseudo-potentials

nl	pn	l	occ	Rcut	Rcut US	E pseu
4s	4	0	2.00	0.000	0.000	0.000000
. 4p	4	1	2.00	0.000	0.000	0.000000
3d	3	2	0.00	0.000	0.000	0.000000
4f	4	3	0.00	0.000	0.000	0.000000

Norm-conserving Pseudopotential	NC
Nonlinear Core Correction	F
PBE Exchange-Correlation Functional	SLA, PW, PBE
Local Potential Cut-off Radius	0.000000000000000E+000
Z Valence	4.0000000000000000
Total Energy	0.000000000000000E+000
Number of Points in Mesh	515
Max Angular Momentum Component	3
Number of Wavefunctions	4
Number of Projectors	3

APPENDIX VI

Conference Presentations & Schools Attended and Articles Under Preparation.

Conference Papers

[1] K. T. Ngeywo., N. W. Makau & G. O. Amolo, *Structural and Electronic Properties of Niobium doped Rutile (110) Surface and Intrinsic Point Defects in Bulk Rutile Titanium Dioxide: a DFT Study*. 1^{st} Multidisciplinary Conference, University of Eldoret, 18^{th} - 19^{th} June, 2015. Submitted for Review.

[2] K. T. Ngeywo., P. V. Mwonga., N. W. Makau & G. O. Amolo, *Intrinsic Point Defects in Bulk Anatase TiO_2 for Green Energy Harnessing.* NACOSTI 5^{th} National Science Week, Kenyatta International Convention (KICC), 16^{th} - 20^{th} May, 2016. Submitted for Review.

Schools and Conferences Attended

[1] Workshop on Computational Science Infrastructure and Applications for Academic Development in the ICTP (smr 2761) – The Abdus Salam, International Centre for Theoretical Physics, Trieste, Italy, 26^{th} September - 9^{th} October, 2015.

[2] The 4^{th} African School on "Electronic Structure Methods and Applications", ASESMA-2016, (smr 2882), Organised in Collaboration with The University of Ghana, Legon, Accra, held on $12^{th} - 25^{th}$ June, 2016.

Articles Under Preparation for submission to peer reviewed Journal(s).

[1] K. T. Ngeywo., P. V. Mwonga., N. W. Makau & G. O. Amolo, *MID-GAP STATES IN DEFECTIVE ANATASE TiO_2 : A GGA+U STUDY*. To be submitted to a peer reviewed Journal.